Exploring The Strong Interaction Through Electroproduction Of Exotic Particles

Matthew Nicol

Doctor of Philosophy

University of York
Physics, Engineering and Technology

October 2022

Abstract

Quarks are the building blocks of hadronic matter. They can combine into systems of three quarks (baryons) and quark-antiquark (mesons). However, evidence for numerous exotics has been found in the last 50 years, from glueballs and hybrid mesons to tetra- and hexaquarks. These greatly advanced our knowledge of the Strong interaction. This thesis presents three new studies for signatures of exotic and non-exotic particles in electroproduction reactions from nuclear targets. The experimental data used in this thesis work was obtained from the CEBAF Large Acceptance Spectrometer for operation at 12 GeV beam energy (CLAS12). CLAS12 is based in Hall B of Jefferson Laboratory, Newport News, Virginia, where an electron is accelerated and impinged off a stationary target.

The first study is of the reaction channel $ep \rightarrow e'pX \rightarrow e'p(K^+K^-)$, which were performed at small electron scattering angles so a quasi-real photon induced the interaction. Angular distribution moments have been produced for the meson resonance X in the hopes of finding possible exotic meson contributions; initial observations are promising, with many structures appearing in the distributions.

A second study is presented with the first-ever extraction of the scaling behaviour of strangeness. An initial estimate for the suppression factor of strange production in electroproduction ($\frac{1}{100}$) suggests one reason for the relative paucity of hyperons discovered. Some strange exotic production is expected to have a weak coupling to individual protons or neutrons, so ratios of strange production cross-sections between a proton and a deuteron target were taken. Enhancements seen via production on deuteron could direct us towards possible new exotics.

The 3rd study focuses on the first constraint on the very strange hexaquark d_{sss}, with the upper limit of the cross-section measured as $\frac{d\sigma_{d_{sss}}}{dMM} = 76 \pm 2$ fb/GeV.

Table of contents

List of figures

List of tables

Acknowledgements

I would like to acknowledge several people who made this project possible.

First, thanks to my supervisors, Dr. Mikhail Bashkanov, Dr. Nicholas Zachariou and Prof. Dan Watts. All three have developed my Hadron Physics knowledge, my understanding of detectors, and my analytical skills. I endlessly challenged Mikhail on the office whiteboard and in the pub. In both cases, he never let me down. Nick could often tell who was at his door just by hearing the knock, probably because it was me 90% of the time. He is always happy to help no matter the time, all it took was some manual labour to soften him up. Dan would often provide incredible ideas after just hearing the problem as if they were simple, before disappearing in a puff of vape mist. Despite being very busy, he always checks in to see how everyone is getting on.

I cannot thank my fiancé, Steph Gardner, enough for dealing with me being stressed and tired 24/7 for three years straight. She picked me up when the PhD beat me down, cheered me through my successes, and never stopped believing in me. She has supported me in working late into the night, travelling abroad several times a year (without getting too jealous), and checking emails every waking minute. Whether it is listening to me ramble on about how I couldn't fix some code or getting our second takeaway of the week because I have had a hard day, she has always been there for me. This process has been so much easier having her by my side.

My parents have supported me throughout my scientific career, from school science clubs to becoming Dr. Nicol. They have always been happy to provide guidance, an ear to listen and even financial support, which enabled me to start my PhD in the first place. Reaching where I am today would not have been possible without them, and for that, I am eternally grateful.

I would like to thank Stuart Fegan, who has single-handedly raised my caffeine consumption by 200%. He has provided so much guidance and wisdom over the last few years "Hrrmm. Only the IOP it is, matter it does not". Stuart is a good friend and has taken it upon himself to make sure all the PhDs in our group make the progress they need (we take up a lot of his time!).

Two other PhD students began at the same time as me and together we have been traversing this immense challenge. Geraint Clash has been my go-to sanity check because if it's crazy he's probably thought of it already. But seriously, he has been a great friend throughout my PhD, whether it is debugging code or moving a sofa up three flights of stairs (and back down again ... and into a new house). Somehow, he even put up with living with me for a year. The other OG PhD student who has helped me climb this mountain is Mihai Mocanu, who would give you both his kidneys without even asking why. He has been incredibly helpful and a true friend.

Declaration

I declare that this thesis is a presentation of original work and I am the sole author. This work has not previously been presented for an award at this, or any other, University. All sources are acknowledged as References.

Chapter 1

Introduction

The work presented in this thesis was obtained from two experiments carried out with the CLAS collaboration, the E12-11-005 MesonEx experiment [1] and the E12-11-005A Very Strange experiment [2].

The MesonEx experiment looks at meson spectroscopy using the CLAS12 detector at Jefferson Laboratory. This work contributes through a search for new and exotic mesons, such as the first tensor glueball with $M \approx 2000$ MeV with the reaction channel: $ep \rightarrow e'pX \rightarrow e'pK^+K^-$. These studies could help further the understanding of possible hadron structures as well as gluon degrees of freedom.

The Very Strange experiment is focused on baryons with strangeness $S = -2$ or -3. Scaling behaviours are ratios between different cross-sections to look for possible enhancements or suppressions of production in given kinematics. Determining the scaling behaviour of strangeness will help further searches of excited baryon states. Finally, this thesis investigates dibaryons (six-quark states with baryon number $B = 2$), by searching for a possible new genuine hexaquark. A genuine hexaquark is a six-quark system bound tightly in a single body, unlike the well-known molecular dibaryon state, where two baryons are bound by meson exchange. This aspect of the research focuses on the search for a very strange hexaquark, d_{sss}, with strangeness $S = -3$. Producing the first-ever upper limit of its cross-section will provide greater insight into six-quark states, as well as narrow the kinematic range for future searches of this dibaryon.

In this chapter, I will briefly detail the main physics elements incorporated into this research as well as the motivation behind it.

1.1 History of Hadron Physics

To best understand and move forward the current models and principles within hadron physics, it is important to know where they have come from and how they have developed. The term 'atom' comes from the Ancient Greek word 'atomos', which means uncuttable, as they believed atoms were fundamental particles. The modern interpretation of the atom begun with the plum pudding model proposed by J. J. Thompson in 1904 [3], shortly after the discovery of the electron [4]. Thompson's theory posited that atoms were a large mass of positive material, similar to the main mass of pudding, with negatively charged electrons spread throughout, represented by the plums.

This theory was later disproved by Ernest Rutherford through his gold foil scattering experiment [5]. In this experiment, α particles were accelerated towards a gold foil while counting rates were measured for different scattering angles. The surprising result was that α particles were being scattered at backward angles, for the plum pudding model this was likened to cannon balls being rebounded off a sheet of tissue paper. Rutherford used the knowledge gained from this experiment to develop the Rutherford model of the atom, which consisted of a dense positive nucleus in the centre, surrounded by light negative electrons [6]. Further developments in the modelling of the atom and its constituents, hadrons and leptons, have been made since, including the Bohr model and quantum model.

Hadron physics has developed a lot since its first postulations, with humans trying to accurately describe the Universe since their existence began, from the most elementary particles to fundamental forces that govern how matter behaves. Our current understanding is that there are four fundamental forces: strong, weak, electromagnetic, and gravitational. The most complete and accurate description to date is the standard model which details three of the four fundamental forces, all except gravitational, and contains 17 fundamental particles as seen in Tab. 1.1. All particles can be described as either a fermion (particles with half-integer spin) or a boson (particles with integer spin). These 17 fundamental particles can be grouped into three categories: leptons, gauge bosons, and quarks.

Leptons are spin $\frac{1}{2}$ subatomic particles that all experience the weak and gravitational forces, some also interact via the electromagnetic but none through the strong force. The known leptons are the electron, muon, and tau, with each of these having a corresponding neutrino.

Gauge bosons are the mediating particles for fundamental forces to interact with matter that come from gauge theories. The mediating particles for the electromagnetic, gravitational, strong, and weak forces are the photon, graviton, gluon and W/Z bosons respectively [8] as shown in Tab. 1.2.

Table 1.1 The fundamental interactions and particles of the standard model [7].

Fermions				**Bosons**	
u	c	t	Quarks	**Fundamental Interactions**	**Mediators**
d	s	b		Strong	8 gluons
ν_e	ν_μ	ν_τ	Leptons	Electromagnetic	γ
e^-	μ^-	τ^-		Weak	W^+, W^-, Z^0
First family	Second family	Third family		Gravitational	Graviton
				Higgs Boson	H^0

Table 1.2 Properties of the four fundamental forces [8].

	Gravity	Electromagnetism	Weak	Strong
Strength	10^{-40}	10^{-2}	10^{-5}	1
Mediator	Graviton	Photon	W^+, W^-, Z^0	8 gluons

Quarks are spin $\frac{1}{2}$ subatomic particles, but unlike leptons, they can interact via all four fundamental forces. There are six quarks: up (u), down (d), charm (c), strange (s), top (t), and bottom (b); Tab. 1.3 highlights the properties of these six quarks.

Table 1.3 Quantum numbers of quarks: B-Baryon number, S-Strangeness, I-Isospin, I_3-3rd projection of isospin, Q-Electric charge, M-Mass.

	B	S	I	I_3	Q	M [MeV]
u	$1/3$	0	$1/2$	$+1/2$	$+2/3$	2.2
d	$1/3$	0	$1/2$	$-1/2$	$-1/3$	4.7
c	$1/3$	0	0	0	$+2/3$	1,275
s	$1/3$	-1	0	0	$-1/3$	95
t	$1/3$	0	0	0	$+2/3$	173,000
b	$1/3$	0	0	0	$-1/3$	4,180

1.2 Constituent Quark Model

The strong interaction affects quarks through its mediating particles, gluons, which are massless charge-neutral bosons that act as an attractive or repulsive force between quarks with the potential to bind them together and form bound systems called hadrons. Despite quarks having colour charge (red, green or blue), when they combine into hadrons this object must be colourless overall (i.e RGB or a colour and anticolour). Hadrons further split into three-quark systems called baryons and quark-antiquark systems called mesons [8]. In the Constituent Quark Model (CQM), the valence

quarks and gluons describe the entire system of a hadron, acting as simple building blocks to combine in different configurations. At CQM's beginning, only three quarks were postulated: up (u), down (d), and strange (s). Hadrons are considered to be part of a unitary symmetry group SU(3), where the '3' represents the three fundamental flavours of the quarks in CQM [9]. They are called symmetry groups because they must remain the same after undergoing certain transformations, SU(3) transformations in this case.

Mesons are one of the simplest systems to study hadron structure, with just a $q\bar{q}$ in CQM. To best understand their properties, quantum numbers are considered [10]:

- l - Orbital angular momentum
- P - Parity, $P = (-1)^{l+1}$
- S - vector sum of spin of quark + spin of antiquark
- J - vector sum of angular momentum and spin $|l - S| \leq J \leq |l + S|$
- C - Charge parity, $C = (-1)^{l+S}$

In this model, mesons are just quark-antiquark pairs with baryon number $B = 0$. They only have two configurations for the quarks' spins, which are aligned or anti-aligned. Quarks have spin $\frac{1}{2}$, therefore, mesons can have a total spin of $S = 0$ or 1 based on these configurations. Integer spin particles such as these are classified as bosons. Particles with the same J^{PC} are grouped into multiplets with the members dictated by SU(3). Nine $q\bar{q}$ combinations comprised of u, d, and s quarks are contained within an octet and a singlet, often considered together as a nonet. Figure 1.1 shows the nonet of pseudoscalar mesons with $J^P = 0^-$ and the nonet of vector mesons with $J^P = 1^-$ on the left and right respectively.

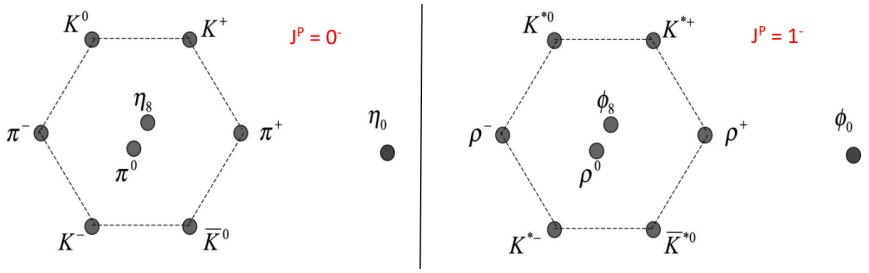

Fig. 1.1 Octets and singlets of pseudoscalar mesons (left) and pseudovector mesons (right) [8].

Baryons are three-quark (qqq) systems with a baryon number $B = 1$. The 'normal' baryons in CQM consist only of u, d, and s quarks suggesting a flavour SU(3); this dictates that baryons made from these quarks must fit into one of four multiplets. One of these multiplets contains only one member (singlet), two contain eight particles (octet), and the last 10 (decuplet). However, the singlet and one of the octets are unphysical and do not appear in nature, leaving us with an octet and decuplet only, as seen in Fig. 1.2

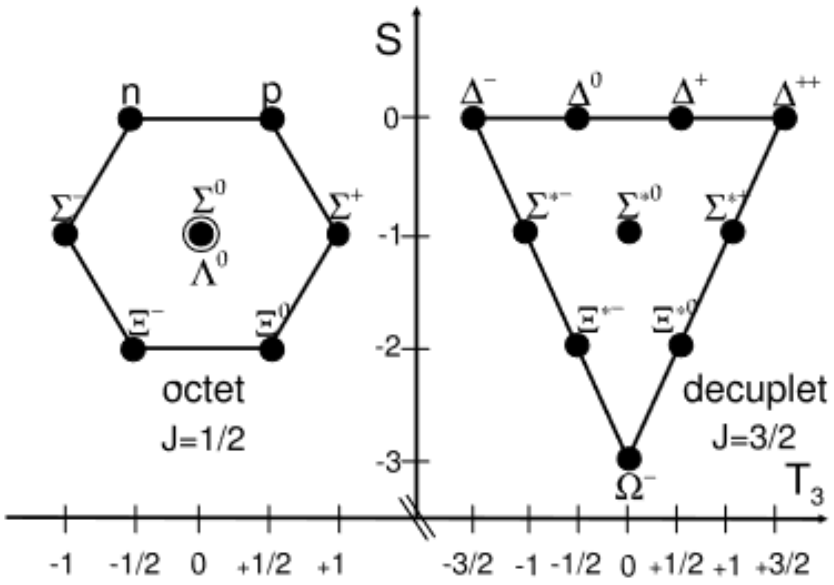

Fig. 1.2 Octet (left) and decuplet (right) of baryons. Here S is strangeness and T_3 is isospin 3rd projection, which corresponds to the electric charge of the state [11].

1.2.1 Strangeness

Many of the known mesons and baryons today consist of primarily the lightest quarks, up and down. Rochester and Butler produced the first evidence for strange particles through the use of cloud-chamber photographs of cosmic ray events. Analysis of these photographs led to the discovery of two new particles later called K and Λ [12]. The K^+ particle discovered by Rochester and Butler is a meson, with quark content $\bar{s}u$. The Λ was the first baryon confirmed to have strangeness, with strangeness $S = -1$, made up of uds. The more general term for a baryon with one or more strange quarks is a hyperon.

In strong and electromagnetic interactions, strangeness is conserved, meaning the total strangeness before an interaction is equal to that afterwards. However, strangeness is not conserved in weak

interactions as a quark's flavour can be changed in these interactions. When a hyperon is produced in a strong interaction, usually a K meson is produced at the same time in order to conserve strangeness. The analysis of this thesis revolves heavily around strangeness and K mesons.

1.3 QCD

The simple model, CQM, described in Sec. 1.2 cannot explain some observed states, such as exotic mesons (hadron with baryon number $B = 0$ and a non $q\bar{q}$ structure) and dibaryons (single object with baryon number $B = 2$). A more developed picture of hadrons and the strong interaction is Quantum ChromoDynamics (QCD). This is an SU(3) gauge field theory that details the strong interactions experienced by quarks as mediated by gluons.

With QCD came the other 2nd generation quark charm (c), and the two 3rd generation quarks top (t) and bottom (b). Top quarks have an incredibly high mass of 173 GeV/c^2, this leads to them being very short-lived, only 5 x 10^{-25} s. Therefore, they are not involved in hadron physics as they decay too quickly to form any sort of bound structure. So in hadron physics, we tend to look for particles that contain a combination of up, down, strange, charm, and bottom quarks.

When theories are developed, they first try to interpret the most basic systems. For hadrons, this would be mesons and baryons. Once these are reasonably well understood and the model has been updated, more complex systems/states are explored to check if the model still holds. Exotics are great candidates for this.

1.3.1 Exotics

There are exotic mesons that would be good candidates for testing QCD , such as glueballs (made entirely of gluons) or hybrid mesons ($q\bar{q}$ and one or more gluons). Both of these systems have gluonic excitations. Gluonic excitations are possible as they carry a colour charge similar to quarks, allowing them to combine with quarks to produce colourless objects such as hybrid mesons. Their colour charge also enables them to self-interact, producing objects such as glueballs.

Dibaryons are systems of six quarks with a baryon number of two - the first to gain significant experimental evidence was deuteron [13]. Dibaryons can exist in many different forms though, this thesis focuses on molecular dibaryons (two baryons bound together in a molecular state) and genuine hexaquarks (six quarks tightly bound in one bag [14]), which are represented in Fig. 1.3.

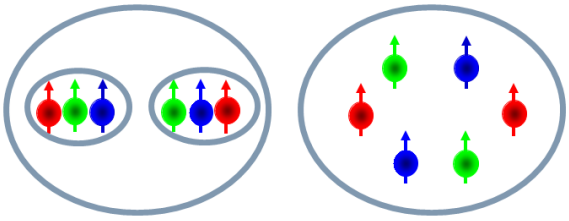

Fig. 1.3 Representative diagram of the internal structure of a molecular dibaryon (left) and a genuine hexaquark (right).

Molecular dibaryons are two separate baryons behaving like a molecule to form one single state of six quarks as seen in Fig. 1.3 (left), the most well-known example of such a state is deuteron. Gluons bind quarks together to form hadrons, but meson exchange is what holds baryons together. This is typically dominated by π exchange, however, this is not always the case. If we consider hyperdeuteron (a dibaryon consisting of a nucleon and a singly strange hyperon), π exchange is forbidden due to isospin conservation.

Genuine hexaquark states are when six quarks are bound tightly together in a single bag as shown in Fig. 1.3 (right), held together by the strong force. Another force that needs to be considered is the colour magnetic force, which acts between quarks. This is repulsive between quarks with their spins aligned and attractive for anti-aligned quarks. The magnitude of this force is inversely proportional to the constituent mass of the valence quarks, as shown by

$$C \propto \frac{1}{m_i m_j}, \tag{1.1}$$

where C is the colour magnetic force between two quarks of mass m_i and m_i. Therefore, its magnitude would be smaller in states with heavier valence quarks. This force is responsible for vector mesons, Fig. 1.1 (right), which are much heavier than the pseudoscalar meson, Fig. 1.1 (left).

By studying exotics and their internal structures we can better our understanding of QCD and hadron physics. This research's focus in searching for exotics will enable us to probe what is and is not possible within QCD.

1.4 Exotic Mesons

The first part of this research explores exotic mesons, such as hybrids and glueballs. In a hybrid meson, the gluonic field can provide a non-zero contribution to the overall meson's spin, allowing

for quantum numbers not possible with a simple $q\bar{q}$ meson. Quantum numbers such as these are called exotic quantum numbers, they include but are not limited to $J^{PC} = 0^{--}$, 0^{+-}, 1^{-+}, and 2^{+-}. Here we use the term exotic hybrid meson for a hybrid meson in which the quantum numbers are not possible in the quark model[1]. Experimental data [15–17] already exists for a few potential exotic hybrid mesons such as the $\pi_1(1400)$ with a $J^{PC} = 1^{-+}$.

We cannot directly detect these exotic mesons as they are unstable and decay too fast, so we must consider their decay modes in order to study them. For normal $q\bar{q}$ mesons, strange production is suppressed, therefore, we do not generally look at strange decay channels. However, in the case of hybrid mesons, the gluon will produce a $q\bar{q}$ pair and it is flavour blind, meaning that its coupling to u, d, or s quarks is equal. Hence, as strange production is suppressed in $q\bar{q}$ mesons but not hybrid ones, it is expected that they would be more prominent here than in pure u and d quark systems. For this reason, this research focuses on the channel $\gamma p \to pX \to p(K^+K^-)$, here X is a mesonic resonance that decays into a K^+ and a K^-. The allowed and forbidden decay modes that can lead to $K\bar{K}$ production are shown in Tab. 1.4. This will help narrow down the meson search, for example, this does not rule out a hybrid meson but an exotic hybrid meson could not decay into $K\bar{K}$ as they have opposite parity and charge parity.

With the detection of the K^+K^- pair, it's possible to reconstruct the undetected resonance that produces them. In meson production, there are often lots of overlapping contributions making it difficult to distinguish between them. These contributions can be considered the sum of many partial waves, separated based on their quantum numbers. A series of Hamiltonians called a meson's moments of angular distribution, indicate the various contributions from these different waves as shown in the equations in Eqs. (A.1) & (A.2). These moments appear as $H^n(LM)$, the Hamiltonian projection is n, the meson's spin is L, and the meson's projection is M. If multiple mesons are being observed, an interference would display as sharp changes in an otherwise smooth distribution. Once the moments have been determined, partial wave analysis (PWA) can be performed to disentangle the overlapping contributions and ascertain the possible mesons and their quantum numbers. At this time, the moments have been determined but no PWA has been done, it is a complicated process and will be performed in collaboration with other experts in the field. For certain moments with limited partial wave contributions, it is possible to make some initial hypotheses, even before PWA, regarding what

[1] For the remainder of this thesis, hybrid mesons with exotic quantum numbers will be referred to as exotic hybrid mesons

mesons we might see interfering based on these sharp changes in the moments' distributions. Chapter 5 details the results from this particular research.

1.5 Scaling Behaviour of Strangeness

Searching for new particles, such as the exotics in this research, is much easier if you can narrow down your search. One of the best ways to do this is through scaling behaviours which give an indication of kinematic regions where enhanced or suppressed production is expected for given reactions. In other words, how do we choose an appropriate scaling behaviour that is likely to lead to the discovery of new exotics?

In some models strange exotic production is expected to be proto- or neutro-phobic, hence comparison between interactions on these two single-nucleons can give an insight into where to expect strange exotic enhancements. Examples of this behaviour are expected for excited states of Λ, such as $\Lambda(1405)$, as they only have one charge state unlike Σ for example, which has three. This is the main motivation of this work, producing the first-ever scaling behaviour of strangeness, as it has a great potential for observing new exotics. These same studies can also make estimates for the suppression factor of strangeness, the reduction in abundance for each additional kaon produced.

An additional benefit of this research is that it could potentially help physicists further explore strangeness, which despite the first strange particles being discovered in 1947 [12], is still an area that requires much more insight. One such area within strangeness is hyperons, baryons with one or more strange quarks. In the last 20 years, no new hyperons have been discovered with three- or four-star classification[1] from the Particle Data Group (PDG) [19], totalling 31 in 2020 compared with 33 N^* excited nucleon states and Δs. As discussed in Sec. 1.2, baryons belong to multiplets, every N^* state belongs to an octet and each Δ state to a decuplet. In baryon octets and decuplets, for each state with strangeness $S = 0$ there are three with $S < 0$. Hence, there should be three times as many hyperons as N^* and Δs, yet approximately equal numbers have been found. The strangeness suppression factor could indicate why this is the case and the scaling behaviour can provide kinematics where there is enhanced strange production, aiding the search for excited baryon states as well as other interesting states of strangeness.

[1] The Particle Data Group classifies a particle's validity with star statuses. One star - "evidence of existence is poor", two star - "evidence of existence is only fair", three-star - "existence ranges from very likely to certain, but further confirmation is desirable and/or quantum numbers, branching fractions, etc. are not well defined", four-star - "existence is certain and properties are at least fairly well explored" [19]

Strong interactions that produce hadrons with negative strangeness such as the Λs, also make positively strange K^+ ($u\bar{s}$) or K^0 ($d\bar{s}$) mesons in order to conserve strangeness. Detecting these K mesons and reconstructing any additional undetected particles, allows us to produce these scaling behaviours and explore what exotics might have been produced. K^+ mesons are easier to detect than K^0 as they are charged, therefore, the work presented in this thesis focuses on the detection of K^+s only.

In electrophotoproduction, a baryon can be produced via baryon resonant production, where the photon couples directly to the target. The photon induces an excitation of the target hadron to a resonance, which generally occurs at lower energies of the order of a few GeV[1]. Non-resonant production is where the photon indirectly interacts with the target via an exchange particle, usually occurring at higher energies than resonant production with photons of several GeV.

Scaling behaviours look at the ratio of cross-sections for different reactions, targets, beams or other experimental conditions. Cross-sections give the probability of a specific reaction channel occurring as a function of one or more kinematic variables. The cross section (σ) is given by

$$\sigma = \frac{\mathbb{Y}}{A\phi l \rho_T}, \tag{1.2}$$

where $\mathbb{Y}$ is the yield, A is the product of acceptance and efficiency, ϕ is the flux, l is the length of the target, and ρ_T is the effective density of the target material given by

$$\rho_T = \frac{\rho N_A}{M}, \tag{1.3}$$

where ρ is the density of the target, N_A is Avogadro's number, and M is the molar mass. Cross-sections can also be calculated theoretically based on current physics models, which can then be checked against experimental data to determine their accuracy or any discrepancies.

1.5.1 Strangeness Suppression Factor

Studying the ratio of cross-sections between one, two, and three kaon production, enables the determination of the suppression factor of strangeness production. Resonant and non-resonant production mechanisms describe different physics elements, therefore, it makes no sense to mix

[1]For the purpose of this scaling research, we focus on baryon production, therefore, we consider baryon resonant production as resonant and anything else to be non-resonant

these. For the suppression factor, we focus on the non-resonant production as it has a more consistent behaviour and distribution than the resonance region.

1.5.2 Isospin dependence of meson coupling

When we instead consider the ratio between the cross-sections of strange production on a deuteron ($\sigma_{d,total}$) and a proton (σ_p) target, we have access to information that can verify the isospin dependence of the exchange meson on the different targets. The cross-section $\sigma_{d,total}$ is given by

$$\sigma_{d,total} = \sigma_p + \sigma_n + \sigma_d, \tag{1.4}$$

where σ_n is the cross-section for interactions on a neutron single-nucleon, and σ_d is the cross-section for coherent interactions on the deuteron two-nucleon system. First, we consider the non-resonant production at higher photon energies where we are focused on the exchange particle.

The main non-resonance strangeness production route is through kaon in-flight production, where a pair of kaons are produced by the incoming photon and a meson is exchanged with the proton or neutron. In this research, only K^+s and the scattered electron are detected, therefore, the possible pairs of kaons are a K^+ and a K^- or a K^+ and a $\bar{K}^0$. For the exchange meson, we can have either an isoscalar or isovector meson with isospin 0 or 1 respectively; examples of these include η for an isoscalar and π for an isovector meson. Electric charge and strangeness are conserved in strong interactions which leads to limited options for these kaon in-flight production channels.

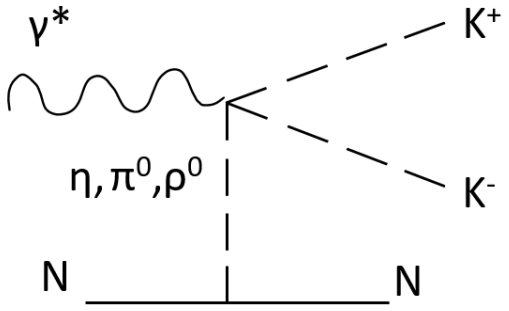

Fig. 1.4 Feynman diagram for kaon in-flight production with neutral exchange meson interacting with nucleon target.

First, we consider the production of a K^+K^- pair, therefore, the exchange meson must be neutral to conserve charge. The neutral meson can be either an isoscalar or isovector meson, with the initial nucleon target ending as the same particle species now with some kinetic energy, shown in Fig. 1.4.

This is possible on a proton and on a neutron and is expected to have equal cross-sections, giving a ratio of 2:1 for deuteron:proton production rates.

The other option is to produce a $K^+\bar{K}^0$ pair with a negatively charged exchange meson, in this case, the meson must be isovector as it is charged. There are no non-resonant options for interacting with a neutron, however, there are for a proton as highlighted in Fig. 1.5. Another 'non-resonant' consideration is Deck contributions, where a resonance is induced by the exchange meson and not directly from the photon. For Deck contributions, the isovector meson can interact with either the proton or neutron equally, a possible option for each is shown in Fig. 1.6 on the left and right respectively. This gives three possible production modes for the deuteron target and two for the proton, giving an expected ratio of approximately $\frac{3}{2}$ for the charged exchange meson production.

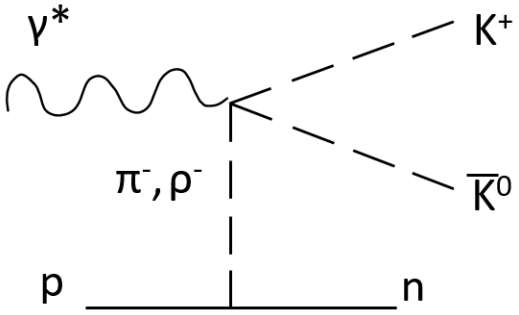

Fig. 1.5 Feynman diagram for kaon-inflight production with charged exchange meson interacting with proton target.

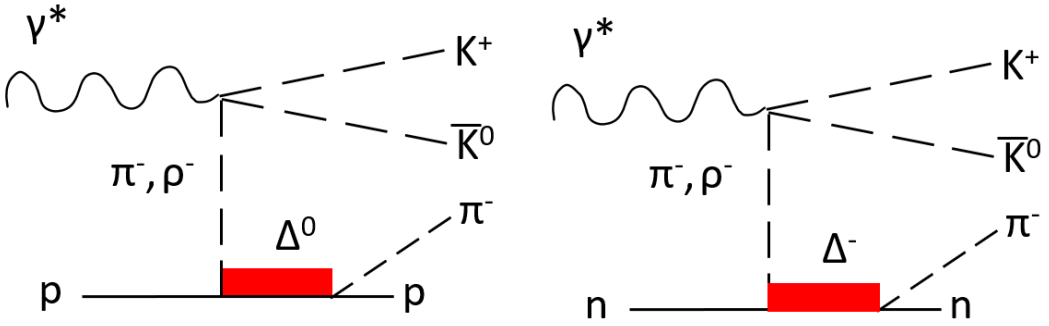

Fig. 1.6 Feynman diagram for kaon-inflight production with charged exchange meson interacting with proton (left) and neutron (right) target showing possible Deck production.

If we consider only neutral exchange mesons in these reaction channels, the scaling of the deuteron to the proton target we would expect is 2. On the other hand, considering only charged exchange mesons, the scaling we would expect is $\frac{3}{2}$. Therefore, looking at both possibilities, the scaling between

deuteron and proton target data should be between $\frac{3}{2}$ and 2 for non-resonant strange production. This scaling can give the proportion of isospin $I = 0$ to $I = 1$ mesons as the exchange particle, showing if either has a stronger coupling to proton or deuteron. Deviations from this expectation or enhancements at given photon energies could indicate new meson species, possibly exotic, being exchanged with the target.

1.5.3 Strange Exotic Baryons

Focusing on resonant production, at these lower energies ($E_\gamma < 2$ GeV), we mainly produce strange baryons (hyperons), which have narrow widths and are often easily identified. As some strange exotic production is expected to have a weak coupling to a proton or neutron, we might observe enhanced production on one nucleon and not the other. As deuteron consists of a proton and neutron, taking the ratio of the cross-sections between deuteron ($\sigma_{d,total}$) and proton (σ_p), allows us to compare the production rates on the two nucleons. Any deviations from a smooth trend could potentially highlight kinematic regions of enhanced production of these exotic or excited states. The results of this research are shown in chapter 6.

1.6 Very Strange Dibaryon

The final exotics search is leading on from recent experimental evidence of the first genuine hexaquark, $d^*(2380)$ [20–22], which has created a whole new area of exploration. The WASA collaboration at COSY, was the first to provide experimental evidence for a genuine hexaquark, the $d^*(2380)$ [22]. The experiment involved a polarized deuteron beam scattering on a hydrogen target. A lot of controversies surrounded the $d^*(2380)$ when it was first discovered, with many believing it was just another molecular dibaryon like deuteron or even a triangular singularity [23]. However, additional studies performed at the Mainz Microtron (MAMI) electron accelerator facility put many of these notions to rest by exploring multiple reaction channels for the $d^*(2380)$ [24]. The experiment was performed in the A2 hall at MAMI. Electrons produce a real photon beam via Bremβtrahlung, which interacts with a deuterium target. This induces the photodisintegration of deuteron atoms inside the target.

All results from the above experiments are in agreement with the basic properties of the $d^*(2380)$, with a mass of M $\approx$ 2380 MeV and a width of $\Gamma \approx$ 70 MeV. This mass is far from the threshold

of two Δs, suggesting this is not a molecular ΔΔ state. Further to this, the very narrow width of 70 MeV is much smaller than two Δs, providing further evidence of a mostly genuine hexaquark state. Additionally, it was shown that the $d^*(2380)$ is likely to be predominantly photoexcited on deuteron in a M3 multipole (magnetic octupole) transition rather than E2 (electric dipole). This behaviour is inconsistent with a molecular state, but is explained under the assumption of a genuine hexaquark $d^*(2380)$ as detailed in Ref. [25].

The $d^*(2380)$ has spin parity $J^P = 3^+$, electric charge $Q = +1$, and a mass of 2.38 GeV. The $d^*(2380)$ forms an antidecuplet of dibaryons with spin parity $J^P = 3^+$, Fig. 1.7. If we consider the dibaryons in this antidecuplet as molecules of two baryons, for the d^* case this would be two Δs, the others are highlighted down the left-hand side of Fig. 1.7.

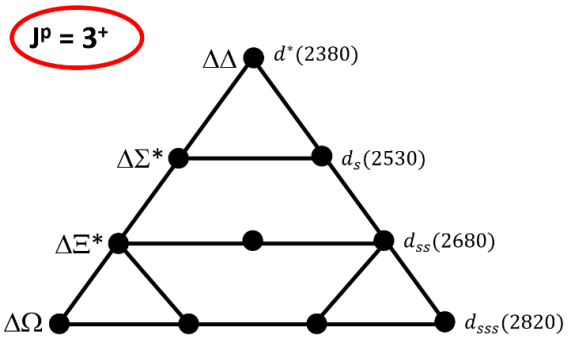

Fig. 1.7 $d^*(2380)$ antidecuplet [26].

Such exotics studies as this can be used to enhance our knowledge of QCD and hadron internal structures. More studies are required to further understand these new states, this research, as well as others within the Hadron Group at the University of York, aim to search for different genuine hexaquarks and explore the d^*'s properties further. The $d^*(2380)$ has been shown to be a hexaquark dominant state [27, 28], it is likely that other members of its antidecuplet are too. For this reason, the work detailed in this thesis shows the initial search for the very strange dibaryon d_{sss}, aimed at producing the first-ever upper limit of its cross-section. To understand the reasoning why the d_{sss} was chosen for this study, we must consider both cases where the d^* and the other members of its antidecuplet are either molecular dibaryons or genuine hexaquarks.

As discussed previously, molecular dibaryons are held together by π exchange, but πs do not couple to strange quarks. Therefore, as we move down the d^* antidecuplet, looking at members that have higher strangeness, we should expect to see a decrease in binding energy if they are molecular.

This relationship between the binding energy of a molecular dibaryon (BE_{Mol}) and the quark content is given by

$$BE_{Mol} \propto \frac{q_{ud}}{q_{tot}}, \tag{1.5}$$

where q_{ud} is the number of light quarks (up or down), and q_{tot} is the total number of quarks in the baryon. If all the antidecuplet members are molecular dibaryons, then d_{sss} would be made from $\Omega\Delta$ and π exchange would be impossible as Ω consists of 3 strange quarks only. Other meson exchanges are possible but π exchange dominates meaning a molecular d_{sss} dibaryon would be very weakly bound. Other baryons, such as $\Xi^*\Sigma^*$, could make up the d_{sss}, allowing for π exchange. This would still lead to a decrease in the binding energy.

On the other hand, if they are in fact genuine hexaquarks, then they will be held together by the strong force with gluon exchange. The magnitude of the strong force will not change with different valence quarks. However, the colour magnetic force decreases with the mass of the valence quarks. In this case, with $J = 3$ dibaryon, all quark spins are aligned, so the colour magnetic force is repulsive as detailed in Sec. 1.3.1. If we again move down the d^* antidecuplet, we start to have fewer up and down quarks and more strange quarks, which are heavier, this means the colour magnetic force will decrease and binding energy will increase.

This divergent trend of strangeness vs binding energy for molecular dibaryons and genuine hexaquarks is shown in Fig. 1.8. This is why binding energy is of key importance, as it will tell us more about the internal structure, and knowledge of this will give us insight into the many body effect in QCD.

The d_{sss} has isospin $I = \frac{3}{2}$ and so has four charge members. This thesis work focuses on the d_{sss}^{--}, in the bottom left of the multiplet in Fig. 1.7. There are no conventional resonant background channels with strangeness $S = -3$ and electric charge $Q = -2$ that could overlap or interfere with a potential d_{sss}^{--} signal. Therefore, if we observe a resonant structure with these properties, it is a good indication of the d_{sss}. As discussed in Sec. 1.2.1, kaons are produced via the strong interaction, which conserves strangeness. Detecting three of these kaons in resonant production means that a system with strangeness $S = -3$ has been produced. If these kaons are all K^+s, then by conservation of charge, this system has charge $Q = -2$. This means that by detecting the scattered electron and three K^+s only, we can select events that potentially originate from a d_{sss}^{--}, without detecting any other final state particles. Chapter 7 highlights the results of the search for the very strange dibaryon d_{sss}^{--} using these criteria.

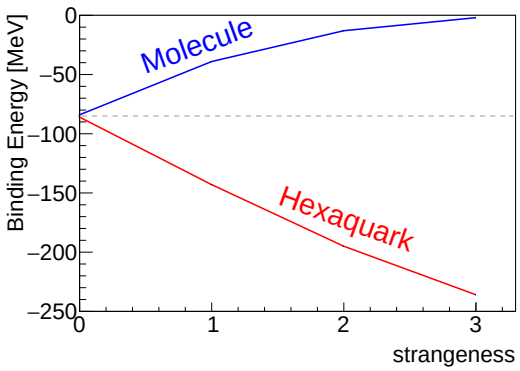

Fig. 1.8 Binding energy of d^* antidecuplet members with the assumption of a genuine hexaquark (red) and a molecular dibaryon (blue)[26].

$J^{P(C)}$	I^G	$K\bar{K}$ (990)
$0^{+(+)}$	0^+	
	1^-	
	2^+	I
$0^{+(-)}$	0^-	C
	1^+	(C) I*
	2^-	(C) I
$0^{-(+)}$	0^+	P
	1^-	P
	2^+	P
$0^{-(-)}$	0^-	P
	1^+	P
	2^-	P
even$^{+(+)}$	0^+	
	1^-	
	2^+	I
even$^{+(-)}$	0^-	C
	1^+	(C) I*
	2^-	(C) I
even$^{-(+)}$	0^+	P
	1^-	P
	2^+	P
even$^{-(-)}$	0^-	P
	1^+	P
	2^-	P
odd$^{+(+)}$	0^+	P
	1^-	P
	2^+	P
odd$^{+(-)}$	0^-	P
	1^+	P
	2^-	P
odd$^{-(+)}$	0^+	C
	1^-	(C) I*
	2^+	(C) I
odd$^{-(-)}$	0^-	
	1^+	
	2^-	I

Table 1.4 Two body decay modes that are allowed and forbidden. The first column shows possible spin (J), parity (P), and charge (C) parity. Column two presents the possible isospin (I) and G parity (G). Following this is the third column with the two-body decay mode and energy threshold in MeV, the matrix below indicates that the decay is allowed if blank and forbidden by the quantum number shown if not[18].

Chapter 2

Historical Review

This chapter will describe some of the historic searches and evidence for exotic particles, up to the most recent studies performed around the world.

2.1 Exotic Meson Searches

In 2000, there were only two experimental candidates for exotic mesons, the $\pi_1(1400)$ [15, 29] and the $\pi_1(1600)$ [30]. It is expected that these are either exotic hybrid mesons, which have been described in Sec. 1.4, or multiquark states such as tetraquarks, with composition $q\bar{q}q\bar{q}$.

Evidence for the $\pi_1(1400)$ has been found by the E852 collaboration at Brookhaven National Laboratory (BNL) [15]. This experiment impinged a π beam off a liquid hydrogen target to induce the reaction $\pi^- p \to \eta\pi^- p$ at 18 GeV. Another study was performed by the Crystal Barrel (CB) collaboration based at LEAR [29]. They performed a protonium annihilation experiment to produce $\pi^0\pi^0\eta$ both in liquid and gaseous hydrogen. To determine the different contributions to this reaction channel, PWA was used. When the CB collaboration included a $\pi\eta$ P-wave in their fits, it reproduced the distributions well, providing further evidence of the potential $\pi_1(1400)$. With quantum numbers, $J^{PC} = 1^{-+}$, this resonance has to be exotic. It has isospin $I = 1$, so it is not possible for this state to be a glueball but it could be a hybrid or tetraquark.

Observations of a resonance with exotic quantum numbers $J^{PC} = 1^{-+}$ and $M \approx 1.6$ GeV have been observed in multiple channels, suggestive of the possible $\pi_1(1600)$ state. PWA was used once more to ascertain the quantum numbers of the mesons involved, this time using the data from the E852 experiment at BNL [31]. The same initial reaction was used for these studies, with πs being

fired at a hydrogen target. However, this time they were studying the channel $\pi^- p \to \pi^+\pi^-\pi^- p$. A complementary study was undertaken by the VES collaboration at IHEP, they also used a π beam to induce the reaction [32]. The VES experiment differed by using a beryllium target, also their π beam had a far greater energy of 37 GeV/c. They also observed a resonance with $J^{PC} = 1^{-+}$ and $M \approx 1.6$ GeV, this time looking in the $b_1(1235)\pi$ and $\eta'\pi$ channels.

In more recent years, further evidence for exotic mesons has been produced. One example is from the COMPASS collaboration with their observation of the axial-vector meson $a_1(1420)$ [33]. Additionally, searches for the lowest mass glueball, the scalar glueball with quantum numbers $I^G = 0^+$ and $J^{PC} = 0^{++}$, are being performed by the BESIII experiment at IHEP[34]. It is heavily mixed with ordinary scalar mesons, making it unlikely to be seen as a pure state. Additional work with BESIII is searching for the tensor glueball $f_2(2200)$, which is the 2nd lightest glueball. This meson has spin $J = 2$ and there is expected to be less mixing with ordinary $q\bar{q}$ mesons than the scalar glueball, this is likely why enhancements can be seen in this study.

2.2 Baryon Excited States

The work in this thesis on the scaling behaviour of strangeness looks at excited states of baryons, both strangeness $S = 0$ and $S \neq 0$. Figure 2.1 highlights the excited baryon states that have been discovered and predicted so far for the light baryons of the SU(6)$\otimes$O(3) singlets and octets. Although a large number of N^* states have been discovered, there are a lot of gaps in the hyperon excited states we expect to find. Each of the N^* states belongs to an octet, which should have a corresponding Λ, Σ, and Ξ state. Many Λ^* and Σ^* states are predicted by lattice QCD and quark models [35].

For many of the excited states we have discovered, we lack understanding of their basic properties, especially the baryons with strangeness. Accurate measurements of what is considered to be one of the best-known baryon resonances, $\Lambda(1520)$, were published in 2011 [36], some 30 years after its initial discovery. This analysis was performed using data from the Jefferson Lab Hall A experiment, where a 5.09 GeV electron beam was impinged off a hydrogen target.

Looking at the double strange baryons, there are currently six Ξ states with a three-star rating from PDG, and only two of them have weak experimental evidence for their spin parity (J^P) [37]: $\Xi(1530)$ with $J^P = \frac{3}{2}^+$ [38] and $\Xi(1820)$ with $J^P = \frac{3}{2}^-$ [39]. The $\Xi(1530)$ study was performed using the BABAR detector at SLAC PEP-II, which is an electron-positron collider. The collisions produce

centre-of-mass energies of 10.58 and 10.54 GeV. A charged hyperon beam was used to determine the spin parity of the $\Xi(1820)$ state at the CERN-SPS. Ξ^-s were accelerated to a mean momentum of 116 GeV/c, at which point they interact with a target, a beryllium rod in this case.

N	(D, L_N^P)	S	J^P	Octet Members					Singlets
0	$(56, 0_0^+)$	1/2	$1/2^+$	$N(939)$	****	$\Lambda(1116)$	$\Sigma(1193)$	$\Xi(1318)$	–
1	$(70, 1_1^-)$	1/2	$1/2^-$	$N(1535)$	****	$\Lambda(1670)$	$\Sigma(1620)$	$\Xi(1690)$	$\Lambda(1405)$
			$3/2^-$	$N(1520)$	****	$\Lambda(1690)$	$\Sigma(1670)$	$\Xi(1820)$	$\Lambda(1520)$
		3/2	$1/2^-$	$N(1650)$	****	$\Lambda(1800)$	$\Sigma(1750)$		–
			$3/2^-$	$N(1700)$	***				–
			$5/2^-$	$N(1675)$	****	$\Lambda(1830)$	$\Sigma(1775)$		–
2	$(56, 0_2^+)$	1/2	$1/2^+$	$N(1440)$	****	$\Lambda(1600)$	$\Sigma(1660)$		–
	$(70, 0_2^+)$	1/2	$1/2^+$	$N(1710)$	****	$\Lambda(1810)^\dagger$	$\Sigma(1770)^\dagger$		
		3/2	$3/2^+$						–
	$(56, 2_2^+)$	1/2	$3/2^+$	$N(1720)^\dagger$	****	$\Lambda(1890)^\dagger$	$\Sigma(1840)^\dagger$		–
			$5/2^+$	$N(1680)$	****	$\Lambda(1820)^\dagger$	$\Sigma(1915)^\dagger$		–
	$(70, 2_2^+)$	1/2	$3/2^+$						
			$5/2^+$	$N(1860)$	**				
		3/2	$1/2^+$	$N(1880)$	***			–	
			$3/2^+$	$N(1900)^\dagger$	****		$\Sigma(2080)^\dagger$		–
			$5/2^+$	$N(2000)$	**	$\Lambda(2110)^\dagger$	$\Sigma(2070)^\dagger$		–
			$7/2^+$	$N(1990)$	**	$\Lambda(2020)$	$\Sigma(2030)^\dagger$		–
	$(20, 1_2^+)$	1/2	$1/2^+$	$N(2100)^\dagger$	***				
			$3/2^+$	$N(2040)^\dagger$	*				
			$5/2^+$	–		–	–	–	
3	$(56, 1_3^-)$	1/2	$1/2^-$	$N(1895)^\dagger$	****				–
			$3/2^-$	$N(1875)^\dagger$	***		$\Sigma(1940)^\dagger$		–
	$(70, 1_3^-)$			5 x					
	$(70, 1_3^-)$			5 x					
	$(20, 1_3^-)$	1/2		2 x					
	$(70, 2_3^-)$			6 x					
	$(56, 3_3^-)$	1/2		2 x					–
	$(70, 3_3^-)$	1/2	$7/2^-$	$N(2190)^\dagger$	****	$\Lambda(2100)^\dagger$			
		3/2	$9/2^-$	$N(2250)$	****				
	$(20, 3_3^-)$	1/2		2 x					
4			$9/2^+$	$N(2220)$	****	$\Lambda(2350)$			
5			$11/2^-$	$N(2600)$	***				

Fig. 2.1 Light baryon excited state spectrum with PDG star ratings, for more details, refer to [40].

Chapter 3

Experimental Setup

This chapter will give an overview of the experimental setup that obtained the data used in this research. It will explain the key detector components involved in this work as well as detail how the different detector types function and are designed to best achieve their physics objectives.

3.1 Jefferson Laboratory

The experiment was performed at the Thomas Jefferson Laboratory (JLAB), an electron beam facility and a U.S. Department of Energy Office of Science national laboratory. Better understanding the nucleus of an atom is one of the primary goals of its research. The electron beam is split between four experimental halls: A, B, C, and D, which all perform various physics experiments.

3.1.1 CEBAF

The Continuous Electron Beam Accelerator Facility (CEBAF) [41] produces and accelerates an electron beam up to 12 GeV. A laser light is shone onto a small piece of gallium-arsenide, transferring enough energy to its atoms that they are ionised, releasing electrons. Next, the electrons enter the accelerator via the injector to start their first circulation of the CEBAF in Fig. 3.1 at close to the speed of light. These electrons are constrained into an incredibly narrow beam similar to the width of a human hair through the use of electromagnets. Directed into the first linear accelerator, the electrons pass through 25 cavities, in which, superconducting radiofrequency (SRF) technology is applied in order to accelerate the electrons further, shown in Fig. 3.1. In order for the SRF cavities to function

effectively, they must be maintained at a temperature of between 2–4 K [41], this is achieved via two refrigeration plants in the centre of the accelerator ring.

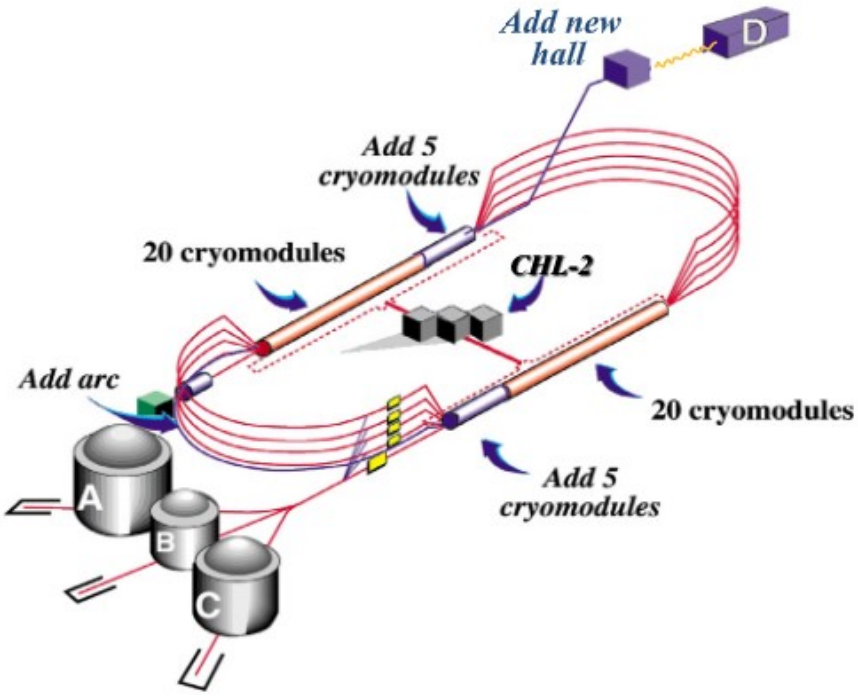

Fig. 3.1 Overview of CEBAF continous electron beam accelerator after 12 GeV upgrade and addition of new experimental Hall D [42].

Once they have travelled through the first linear accelerator, magnets in the arcs at the end of the accelerator ring are used to recirculate the electrons down the other linear accelerator which runs antiparallel. This process is repeated around the entire loop up to 5 times for halls A, B, and C or 5.5 times for Hall D, producing an electron beam of up to 12 GeV. The beam is delivered in small bunches every few ns so it can be split into all four halls, allowing experiments to work simultaneously.

3.2 CLAS12

CLAS12 is the CEBAF Large Acceptance Spectrometer (LAS) which impinges an electron of up to 12 GeV off of a stationary target [42] . For the research project in this thesis, a liquid hydrogen (proton) or liquid deuterium (deuteron) target was used. The detector set-up is split into three sections: Forward Tagger (FT), Forward Detector (FD), and Central Detector (CD). The CLAS12 set-up with key detectors labelled is shown in Fig 3.2.

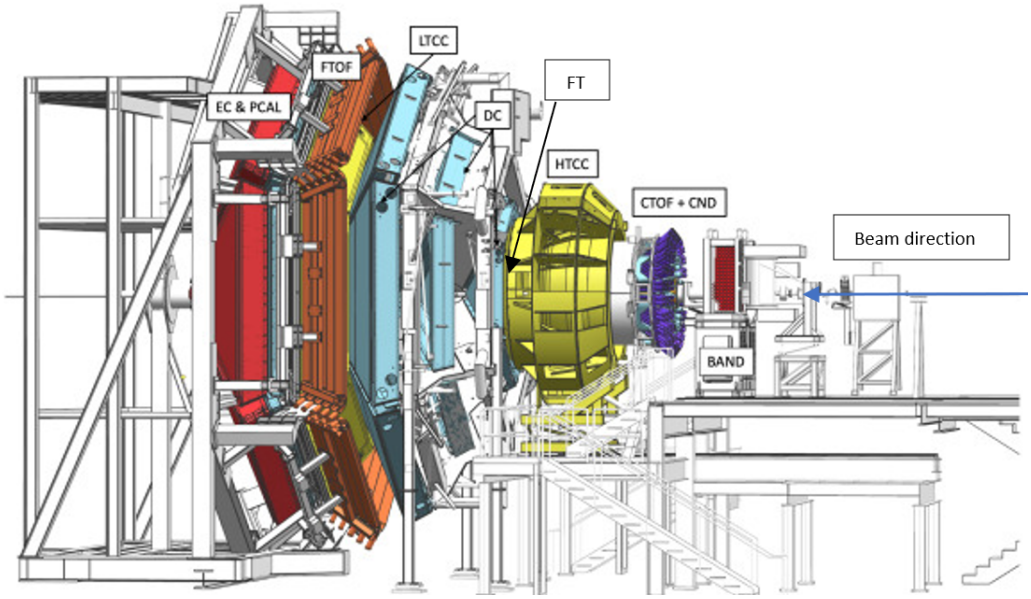

Fig. 3.2 CLAS12 apparatus in Hall B beamline with key detector components labelled and the direction of the beam [42].

3.2.1 Forward Tagger

The FT [43] covers the polar angular range $\theta = 2.5$–4.5°, looking at electrons close to the beamline. Detecting scattered electrons at small angles with low squared four-momentum transfer, Q^2, allows for experiments with quasi-real photoproduction. A simple Feynman diagram showing an electron scattering off a proton target, producing a virtual photon that exchanges squared four-momentum Q^2 is shown in Fig. 3.3. Reconstruction of the quasi-real photon requires information on the scattered electron, specifically, its three-momentum. First, the scattered electron's energy $E_{e'}$ is used to determine the photon's energy (E_γ), given by

$$E_\gamma = \nu = E_{beam} - E_{e'}, \tag{3.1}$$

where ν is the energy exchanged via the electron scattering, E_{beam} is the energy of the e^- beam. The linear polarization (P_γ) is then given by

$$P_\gamma = \varepsilon \approx (1 + \frac{\nu^2}{2E_{beam}E_{e'}})^{-1}, \tag{3.2}$$

where ε is the virtual photon polarization. Next, to determine the polarization plane, the azimuthal angle (ϕ) of the scattered electron is needed. Lastly, the polar angle ($\theta_{e'}$) is used to calculate the four-momentum transfer (Q^2), which is given by

$$Q^2 = 4E_{beam}E_{e'}sin^2(\frac{\theta_{e'}}{2}). \tag{3.3}$$

To achieve these measurements, the FT has three subsystems, these are the calorimeter (FT-Cal)

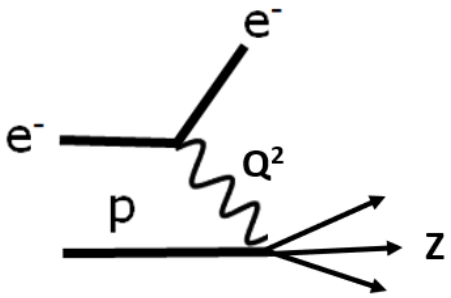

Fig. 3.3 Electron scattering Feynman diagram with a proton target. A photon with squared four-momentum Q^2 inducing a reaction producing the resultant particles Z.

which identifies electrons; the Micromegas tracker (FT-Track) which measures their scattering angles; and the hodoscope (FT-Hodo) which separates electrons and photons. These detectors are positioned between the Drift Chambers (DC) and the High Threshold Cherenkov Counters (HTCC) as shown in Fig. 3.4.

FT-Cal

The role of the FT-Cal is to determine the energy of electrons and photons, as well as their interaction time and position. The main interactions of photons with matter are Compton scattering, photoelectric effect, and pair production. For high-energy photons (above a few MeV), such as in this experiment, pair production dominates; this is where the photon converts into an electron-positron pair. Electrons of these energies predominantly emit photons when they interact with matter, this process is called Bremβtrahlung. These processes continue as the particles travel through the material, producing an electromagnetic shower, which leaves the remaining particles with lower energy. If there is enough matter, the electrons and photons will then undergo scattering to lose their remaining energy until atoms in the material absorb them. The resulting photons of these processes are absorbed by

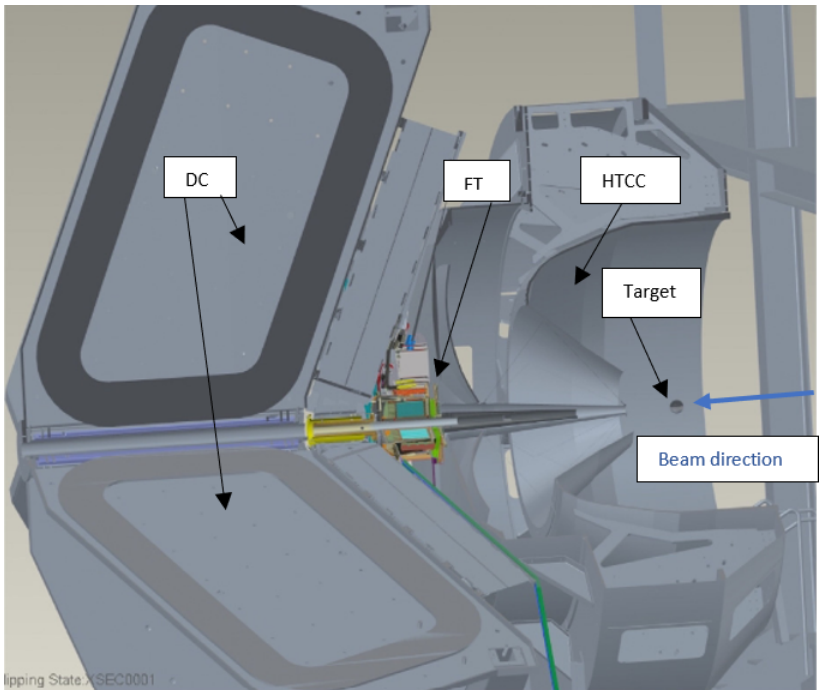

Fig. 3.4 Cross-section of the FT and the surrounding detectors [43].

photodetectors, which use cluster algorithms to reconstruct the original interaction particle. This provides the particle's energy and interaction time.

To cope with the high rates and achieve a precise measurement for the scattered electron interaction time, a fast scintillation decay time is required. For this reason, lead tungstate ($PbWO_4$) crystals are used, which have a decay time of just 6.5 ns. The individual crystals are $15 \times 15 \times 200$ mm^3, with the entire array containing 332 of these. Full azimuthal angular coverage ($\phi = 0$–$360°$) is provided by these crystals as well as a small forward angle acceptance ($\theta = 2$–$5°$). The FT is located in a strong magnetic field and is restricted to a small volume, making the use of photomultipliers (PMTs) not feasible, however, semiconductor-based photodetectors work well under these requirements. For this reason, Large Area Avalanche Photodiodes (LAAPDs) are used in the FT-Cal.

FT-Hodo

Electrons and photons will produce electromagnetic showers in the FT-Cal, the FT-Hodo's job is to separate these [43]. The probability of a particle interacting with matter is proportional to Z (atomic number), so photons have a low likelihood of interaction in the plastic scintillators in the FT-Hodo. However, as electrons are charged, they still have a reasonable probability of interacting with the

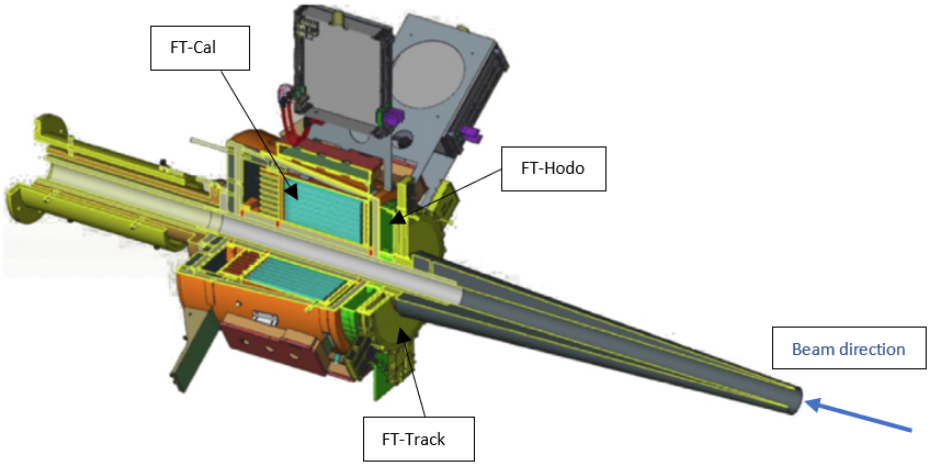

Fig. 3.5 Overview of the FT with the FT-Cal (blue), FT-Hodo (green) and the FT-Track (yellow)[43].

oppositely charged atomic nuclei in the scintillation material. This enables the FT-Hodo to primarily detect electrons. Additionally, the scintillators are in two layers that are only 7 mm and 15 mm thick in the upstream and downstream layers respectively. This small amount of material further decreases the chance that a photon will interact in the scintillators. The position and timing of these interactions are then matched with the electromagnetic showers in the calorimeter, thereby separating the photons and electrons detected in the calorimeter.

The FT-Hodo is located upstream of the FT-Cal. There are 232 plastic scintillators split across two layers, with 44 15×15 mm^2 and 72 30×30 mm^2 scintillators on each layer, shown in Fig. 3.6. For the light readout, 3×3 mm^2 Hamamatsu S13360-3075PE SiPMs are used, these are coupled to 5 m long clear optical fibres, which are in turn embedded into the scintillator tiles. The two layers of the FT-Hodo also enable identification of the signals of interest from electromagnetic splash-back produced in the FT-Cal.

FT-Track

At the time of this research, the FT-Track detector had misalignments in the mapping; this meant the tracking information provided by this detector was not suitable. For the studies in this thesis, the gravity point of the electromagnetic showers in the FT-Cal was used for the tracking instead. A brief description is included of the various components and workings of this detector, for more details refer to Ref. [43].

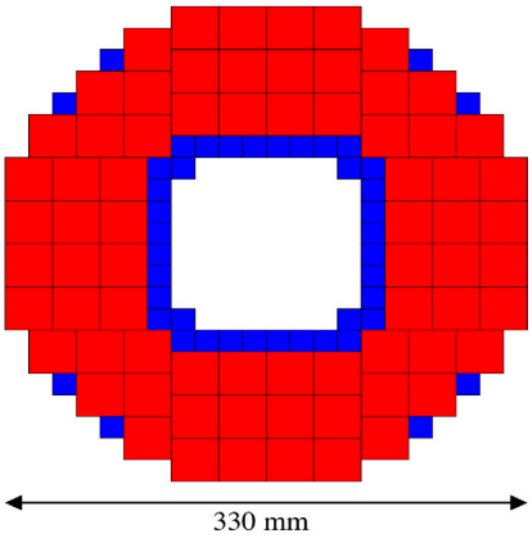

Fig. 3.6 Scintillator tile arrangement in the FT-Hodo, made up of 15×15 mm^2 tiles (blue) and 30×30 mm^2 tiles (red)[43].

Micromegas are gaseous detectors consisting of very thin cathode and anode strips producing an electric field region strong enough for electron multiplication, inside a container filled with gas [44]. As charged particles pass through, they ionise the gas atoms. The electrons released are accelerated towards the anode strips. Before reaching them, they enter a region with an incredibly high potential difference (amplification gap), which is shown in Fig. 3.7. The potential difference is strong enough to produce electromagnetic avalanches.

When the electron shower reaches the anode strips, it deposits its energy and the strip that is fired gives positional information of the charged particle. In the FT-Track, this is used to get accurate positioning of the scattered electron and in turn, gives its angle relative to the beam. Micromegas use thin strips surrounded by an insulating material instead of the traditional wires of a multi-wire chamber, this allows for a more precise position information of the order of 100 μm compared with 200–300 μm.

The FT-Track is positioned upstream of the FT-Hodo, with two layers of double-faced Micromegas disks between the FT-Hodo and the high threshold Cherenkov counter (HTCC), shown in Figs. 3.4 and 3.5. The FT-Track is filled with a gas mixture composed of 90% argon and 10% isobutane. This generates a high number of electrons in the conversion gap whilst minimising the Lorentz force effects due to the low drift velocity.

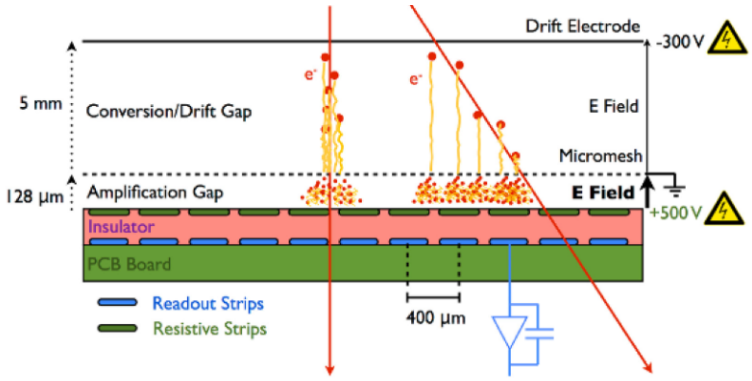

Fig. 3.7 Simple overview of a micromegas detector with key elements labelled [45].

3.2.2 Forward Detector

The FD covers the angular range $\theta = 5$–45°. The FD's subsystems are the Drift Chambers (DC) which measure particles' trajectories and momenta; the Cherenkov detectors which separate electrons, pions, and kaons; scintillators which are used for time of flight measurements in the Forward Time Of Flight (FTOF) detector; and the electromagnetic calorimeters (ECAL) used to detect e^-, γs, and neutrons [46–49].

Drift Chambers

The DC is a wire chamber, a large container with fine electrical wires going from one side to the other and filled with gas. CLAS12 uses a mixture of argon and carbon dioxide (90%:10% respectively) [46]. Charged particles ionise the atoms in the gas as they travel through the DC, and the ionisation electrons are attracted to the positive anode wires, allowing the trajectory of the particle to be tracked [50].

As the charged particles' trajectory is bent through the magnetic field, their trajectories correspond to arcs. The lower momentum particles will have a smaller radius curvature compared with higher momentum particles, therefore, the radius of these arcs refers to the momentum of the particle.

As with the rest of the FD, the DC was constructed around the six coils that make up the superconducting toroidal magnet, splitting the detector into six sectors in the azimuthal angle [46]. There are 3 regions, shown in Fig. 3.8 (blue), in the DC that are comprised of two 'superlayers', each of six layers. Every one of these layers has 112 hexagonal cells which cover the angular range $\theta = 5$–40°. With six layers, even if there are some individual wire inefficiencies, the DC still obtains

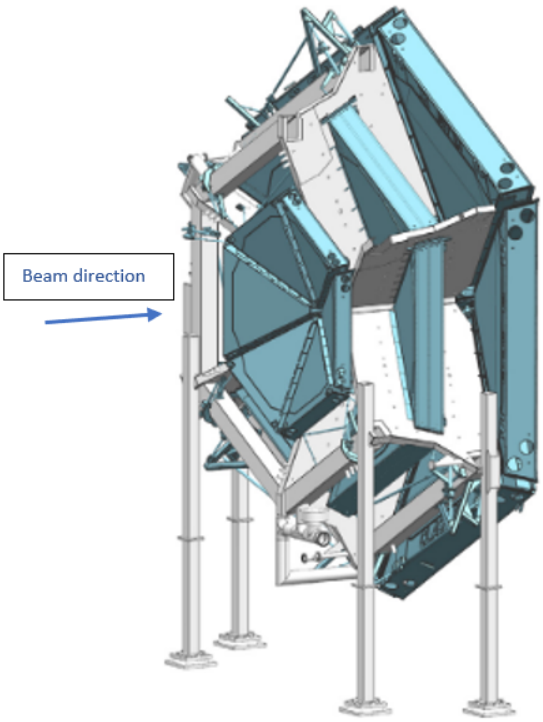

Fig. 3.8 Design model for the Drift Chamber system with the three regions highlighted in blue and the support structure in white. The beam direction is left to right in this figure [42].

good tracking efficiency. The hexagonal cell layout, a large number of layers, and the choice of gas substance and ratio all contribute to giving the DC its relative momentum resolution of $\sigma = 1\%$.

Forward Time Of Flight

There are several approaches to determine a particle's species, one approach uses the particle's relativistic speed (β) and momentum to calculate its mass. The relativistic speed is given by

$$\beta = \frac{v}{c}, \tag{3.4}$$

where v is the particle's speed and c is the speed of light in a vacuum. A particle's speed can be obtained by getting timing information at two known points along its trajectory, a distance d apart. The speed is given by

$$v = \frac{d}{t}, \tag{3.5}$$

where t is the time difference between the two points

The Forward Time Of Flight (FTOF) detector system is the main component in CLAS12 to provide timing information for particle identification. FTOF uses plastic scintillators to get timing information of particles. With the particle's hit time and position in the scintillator and the initial vertex time given by the beam bunch time, the particle's speed can be calculated. Therefore, Eq. (3.5) can be rewritten as

$$v = \frac{\overrightarrow{AB}}{t_{TOF} - t_{vertex}}, \tag{3.6}$$

where $\overrightarrow{AB}$ is the distance between A (vertex position) and B (TOF hit position), t_{TOF} is the hit time in the TOF, and t_{vertex} is the vertex time.

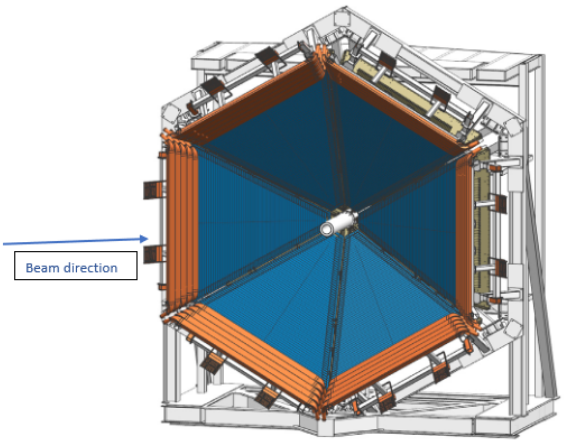

Fig. 3.9 Overview of the FTOF detector. Panel 1B counters are shown in blue, panel 2 surround the perimeter in orange. Panel 1A counters are downstream behind panel 1B and not visible in this figure[48].

FTOF separates into three layers (1A, 1B and 2), each comprising rows of plastic scintillator bars with a PMT readout on each end. Figure. 3.9 highlights the location of the different layers and their respective counters. FTOF layers 1A and 1B cover the angular range: $\theta = 5 - 35\ ^\circ$, with 1A directly behind 1B further downstream to ensure accurate timing measurements are performed for most forward-going particles. Layer 2 surrounds the target to detect lower momentum particles bent far away from the beamline at the angular range: $\theta = 35$–$120\ ^\circ$. Timing resolution is critical to get a reliable PID, FTOF1B's timing resolution is $\sigma = 80$ ps. This allows separation to a four σ level of πs and Ks up to 2.6 GeV, ps and Ks up to 4.8 GeV, and ps and πs up to 5.4 GeV, seen in Fig. 3.10. This highlights how difficult it can be to accurately identify kaons at higher momenta, for this, we can use the Low Threshold Cherenkov Counter (LTCC).

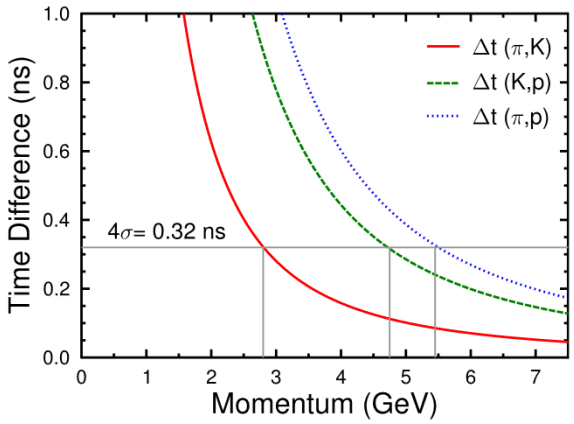

Fig. 3.10 Difference in flight time (ns) for a 7 m path length from the target to the FTOF against particle momentum (GeV) between different particle species as indicated [48].

Cherenkov Counters

Scintillator-based PID detectors, such as FTOF, work well for lower momentum particles. However, they are not reliable at separating particle species at higher momentum due to timing resolution, as detailed in the FTOF subsection. A phenomenon called Cherenkov radiation allows for better separation of particles at these higher momenta. Cherenkov radiation is produced when a charged particle passes through a material moving faster than the phase velocity of light in that material, emitting prompt photons (Cherenkov light). Cherenkov detectors take advantage of this phenomenon by filling the detector system with gas and aligning mirrors to direct the Cherenkov light produced onto photodetectors.

CO_2 is the medium used in the High Threshold Cherenkov Counters (HTCC). At room temperature and atmospheric pressure, CO_2 has a refractive index of 1.00045. The Cherenkov radiation produced in this medium is directed by 48 elliptical mirrors onto 48 photomultiplier tubes (PMTs), the layout of which can be seen in Fig. 3.11. The electronic signal created in these PMTs is used to identify high momenta πs and e^-s. The energy range of scattered electrons in the CLAS12 detectors is 1-10.5 GeV, due to the electron's low mass (0.511 MeV/c^2), its minimum speed is 99.999987% of that of light in vacuum. Therefore, all the scattered electrons produce Cherenkov radiation. πs, with a much larger mass of 139 MeV/c^2, require energies of approximately 4.6 GeV to produce Cherenkov light, so any particles of energy lower than this with light in the HTCC are electrons. The two particle types can still be separated at higher energies as they have different characteristic signals. The HTCC is great for distinguishing between electrons and πs at these energy ranges, however, due to the low

refractive index of the CO_2 medium, it is not suitable for detecting heavier particles such as Ks. For such particles, one must look to the Low Threshold Cherenkov Counters (LTCC).

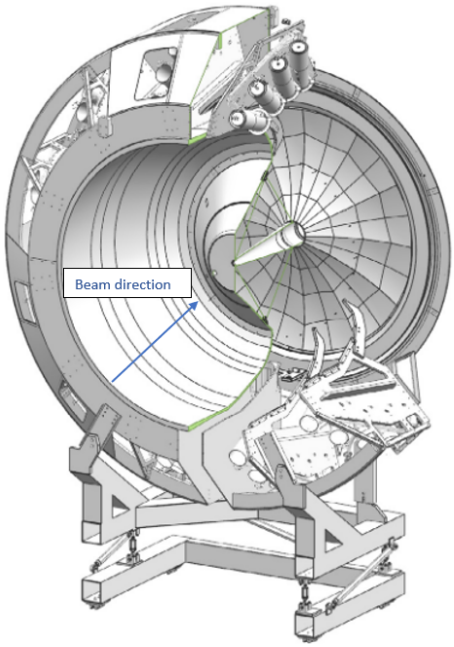

Fig. 3.11 Cut view of the HTCC detector. The elliptical mirrors are shown to the right downstream, whilst the PMTs are arranged in 12 groups of four towards the outer edge of the detector[42].

To correctly distinguish between high momenta πs and Ks, the LTCC has been installed in the CLAS12 setup, using a very similar setup to the HTCC but with C_4F_{10} as the medium because of its higher refractive index of 1.00134. The LTCC enables charged π/K separation for energies between 3.5–9 GeV/c, this gives greater possibilities for identification of Ks and πs at higher momenta than the FTOF system which has 4 σ separation only up to 2.6 GeV.

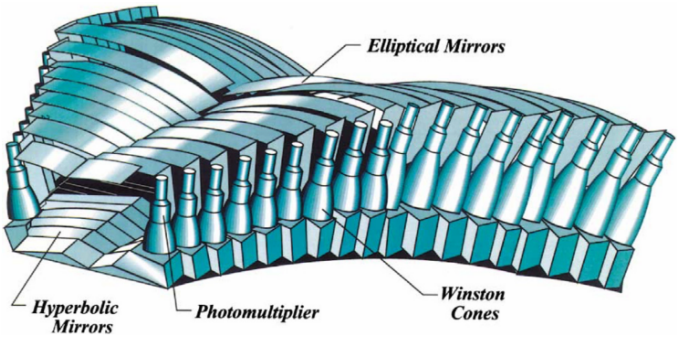

Fig. 3.12 The design model for each of the LTCC boxes, highlighting the key components and their layout [42].

As is shown in Fig. 3.12, the LTCC system is made up of truncated pyramids that are referred to as boxes. There are LTCC boxes in four of the six sectors of CLAS12. The LTCC has a total of 108 lightweight mirrors per box spread across a layer of elliptical mirrors and a layer of hyperbolic mirrors [51]. The Cherenkov light produced by charged particles in the radiator gas volume is reflected off the elliptical mirrors towards the hyperbolic mirror array. To aid with the light collection, the LTCC has 36 Winston light-collecting cones, which the hyperbolic mirrors direct the light towards. Lastly, this light is detected by 36 125 mm diameter PMTs. For the semi-inclusive deep inelastic scattering (SIDIS) physics program, improved particle identification was required between 3–8 GeV, this led to the installation of a ring imaging Cherenkov (RICH) detector, replacing one of the four LTCC modules. Details on the RICH detector can be found in Ref. [47].

The HTCC is not used in this research because this work focuses primarily on the detection of kaons, which the HTCC does not specialise in. Additionally, as the LTCC and RICH only cover four of the six detectors, they do not provide the full 360° coverage in the azimuthal angle desired for these research projects and are also not considered.

Electromagnetic Calorimeters

The main purpose of the calorimeters in the CLAS12 detector system is to identify electrons, photons, $\pi^0 \to \gamma\gamma$ decays, and neutrons [42]. The two main components of the electromagnetic calorimeters are the Electromagnetic Calorimeter (EC) and the Pre-shower Calorimeter (PCAL). Both the EC and PCAL are made up of six modules and combined they are called the ECAL. The PCAL was added for the 12 GeV beam energy upgrade to extend the radiation length of the detector, the EC alone would not completely absorb the electromagnetic showers caused by this higher energy beam.

Six lead scintillator electromagnetic sampling calorimeters work independently to make up the ECAL. These consist of 15 layers of plastic scintillators that are separated by 14 lead sheets. A novel triangular hodoscope design was used for the ECAL to accommodate CLAS12's hexagonal layout, as shown in Fig. 3.13. For detailed descriptions of the PCAL's and EC's construction, refer to Ref. [49].

3.2.3 Central Detector

The Central Detector covers the angular range $\theta = 35$–$125°$. The CD's subsystems are the Silicon Vertex Tracker (SVT) for momentum and vertex reconstruction ; the Central Time Of Flight (CTOF)

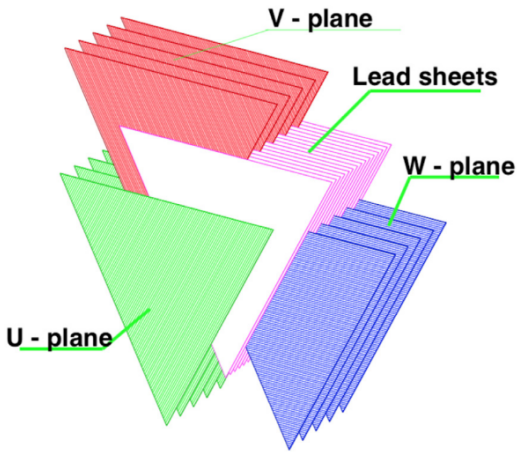

Fig. 3.13 Visualisation of the scintillator layers separated by lead sheets. The U, V, and W planes each have five layers of scintillator strips [49].

which measures TOF at complimentary angles to the FTOF; and the Central Neutron Detector (CND) which detects neutrons [52–54].

Silicon Vertex Tracker

The SVT is a solid-state detector based on silicon semiconductors. Semiconductors in nuclear physics are generally made from germanium or silicon; silicon is relatively cheap and its well established manufacturing makes it a great choice for many experiments, with the ability to make large complex arrays.

Semiconductor materials can be made with the atoms having an excess of electrons or holes in their outer shells; these are classified as n-type (negative) and p-type (positive) respectively [55]. When these two materials come in close contact, the electrons from the n-type material can bridge the junction between them and combine with the holes in the p-type material. Charge carriers in the junction are neutralized, which is called the depletion region. Radiation entering the depletion region produces electron-hole pairs, similar to what is observed in an ionization chamber. The electrons flow towards the p-type semiconductor and the holes towards the n-type. The total electrons gathered form an electrical pulse with its amplitude being proportional to the radiation's energy.

The barrel structure of the SVT is formed of three concentric polygonal regions, covering the angular range $\theta = 35 - -125^{\circ}$ [52]. Region 1 is the innermost layer positioned at a radius of 65 mm from the beamline and contains 10 double-sided SVT modules, Region 2 is placed at 93 mm with 14 modules, and Region 3 is at 120 mm with 18 modules. The dimensions of the SVT modules are

41.9 cm×4.2 cm×0.39 cm and they are all identical. On both sides of the modules are single-sided, 320 μm microstrip sensors that are manufactured by Hamamatsu Photonics. Three 112 mm×42 mm sensors, corresponding to 256 strips, make up each of the two layers, these strips are placed at varying angles between 0–3° to reduce the dead sensor area. Momentum resolution of the SVT is of the order of σ =6% compared with the DC's 1% for the forward-going particles.

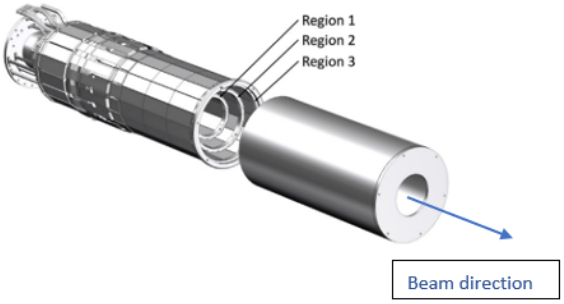

Fig. 3.14 Overview of the SVT barrel and Faraday cage. The beamline follows the SVT axis, entering from the left [52].

Central Time Of Flight

The CTOF's purpose is to identify charged particles coming from the target at large angles, it covers the range $\theta = 35$–$125°$. Similar to FTOF, the scintillation material used is plastic scintillators. 1 m long upstream and 1.6 m long downstream focusing light guides are used to connect the scintillators to PMTs on each end of the scintillators to achieve a double-sided photomultiplier (PMT) readout. There are 48 scintillators in the array which forms a hermetic barrel around the target to ensure most of the charged particles emitted from the target are detected. The tracks from the SVT are then matched with hits in the CTOF to determine β vs. P measurements for particle identification.

Central Neutron Detector

The purpose of the Central Neutron Detector (CND) is to detect neutrons between angles $\theta = 40°$–$120°$ with momentum of 0.2–1 GeV. Three layers of plastic scintillators surround the beamline in a barrel shape, as shown in Fig. 3.16. The scintillators bars are trapezoidal in shape, with 48 in each layer spanning the full azimuthal angular range. 72 U-turn light guides are used to direct the scintillation photons towards all 144 Hamamatsu PMTs, which are used for the readout of these

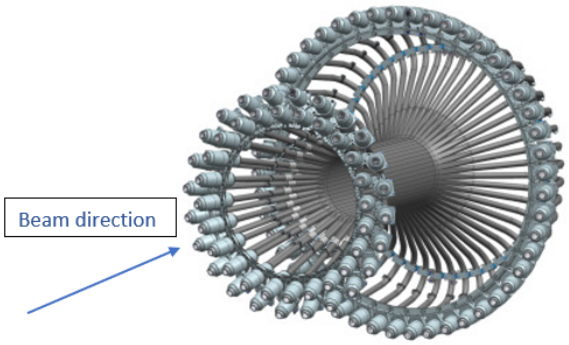

Fig. 3.15 CTOF layout, showing the plastic scintillator barrel, PMTs, and light guides[53].

scintillator bars. Neutrals are not considered in this thesis work, therefore, this subsystem of CLAS12 is not used.

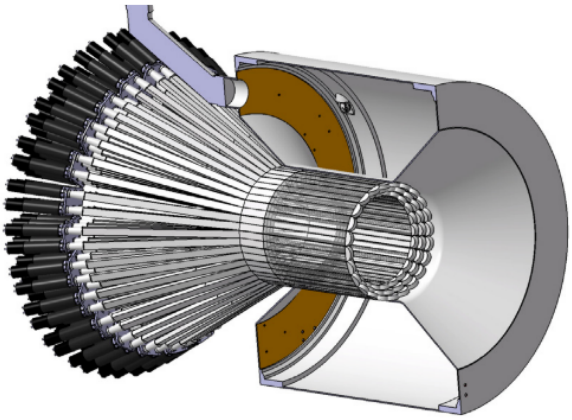

Fig. 3.16 Cut view of the Central Neutron Detector (CND) [54].

3.2.4 Superconducting Magnets

Tracking charged particles in a magnetic field is an effective way to study their trajectories, momentum, and separate particle species. This is why the solenoid and torus magnets have been installed, to bend low-energy (300 MeV–1.5 GeV) and higher energy (0.5 GeV–10 GeV) charged particles' trajectories respectively [56]. The solenoid magnet is located upstream of the torus magnet and consists of five NbTi coils, producing a magnetic field of up to 5 T. The torus magnet applies an approximate toroidal field distribution around the beam axis. Employing the use of six superconducting coils arranged symmetrically around the beamline so the field generated is focused mainly in the azimuthal direction (ϕ). The peak magnetic field produced by the torus magnet is 3.6 T. Both magnets were designed

to not impede the trajectories of particles, allowing for long path lengths to the TOF detectors for accurate particle identification.

3.3 Targets

CLAS12 can host many different stationary targets from hydrogen to lead. The data used to produce all the results in this thesis is from either a liquid hydrogen or liquid deuterium target, allowing for interactions on protons (single-nucleon) and deuteron (two-nucleon system).

3.4 Faraday Cup

At the end of the beamline in Hall B, 29 m further downstream than the CLAS12 detector, there is a Faraday Cup (FC) composed of 4000 kg of lead, shown in Fig. 3.17 [42]. This equates to 75 radiation lengths so the FC can entirely absorb the beam. The charge deposited on the FC needs to be extracted, this is done through the use of an electrical feed-through, which determines the accumulated charge. Once the total charge has been determined, this can be used to calculate the number of electrons (N_e) that were impinged off the target is given by

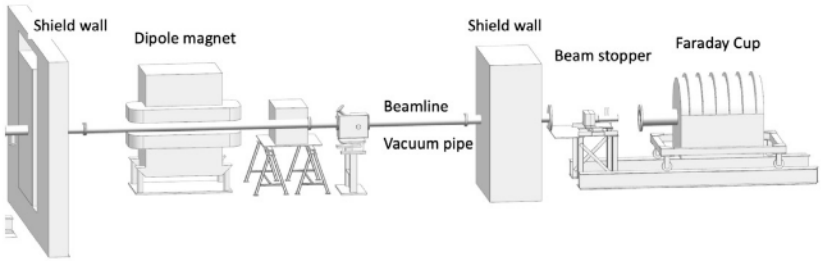

Fig. 3.17 Layout of the beamline downstream of the CLAS12 detector system to the Faraday Cup (FC)[42].

$$N_e = \frac{Q_{Acc}}{q}, \tag{3.7}$$

where N_e is the number of electrons (flux), Q_{Acc} is the accumulated charge on the FC in Coulombs, and q is the charge of an electron with 1.6x10^{-19} C.

3.5 Data Acquisition(DAQ) and Trigger

The detectors in physics experiments experience enormous volumes of signals per second and only a small portion of these can be written to a data storage system. Therefore, it is important that these signals are filtered rapidly (of the order of 10s kHz) to determine which events should be recorded. The CLAS12 DAQ was operating at trigger rates of approximately 15 kHz in 2018, recording data at speeds up to 500 MB/s, this equated to a livetime that was greater than 95%. Conditions are set to ascertain whether an event is processed and stored, these can be very broad but the two main types are based on hardware responses and physics requirements. Cluster mapping is an example of checking hardware responses, it is performed in the ECAL to determine whether the scattered electron has been detected [42]. A physics-based trigger could be a constraint on multiplicities, requiring a certain number of charged particles for example. Figure 3.18 shows the structure of the DAQ and trigger systems in place at CLAS12. This also highlights how the different detector systems' readouts are processed.

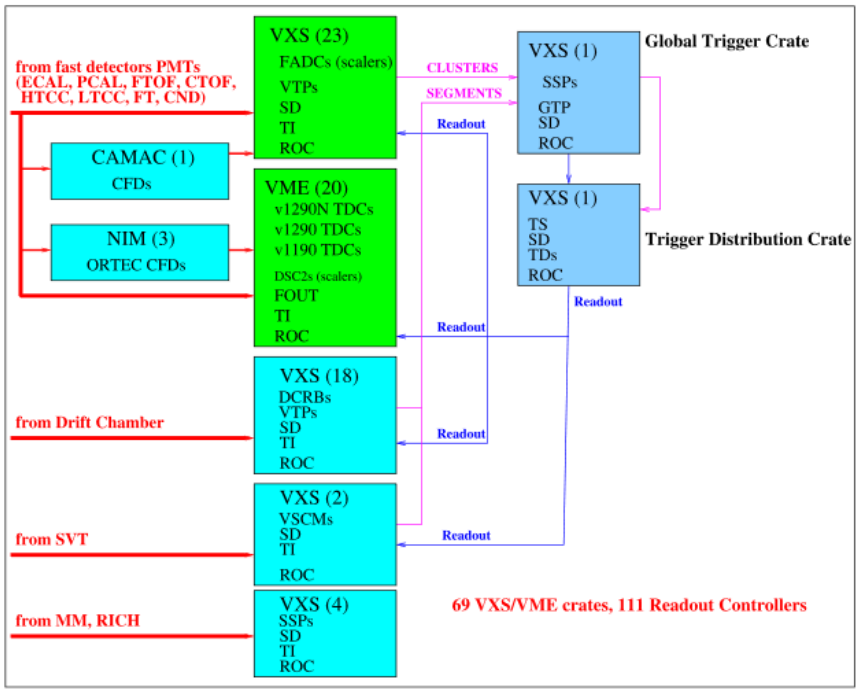

Fig. 3.18 Schematic diagram showing the DAQ and trigger systems in place at CLAS12 [42].

The trigger conditions used in the exotic meson study of this thesis, with the reaction channel $ep \to e'pX \to e'p(K^+K^-)$, were defined by the MesonEx trigger set out by the MesonEx working

group. The basic condition for all channels was the detection of the scattered electron in the FT ($\theta = 2.5$–5°). To verify this, a cluster in the FT-Cal with energy greater than 0.5 GeV, a width larger than the minimum required for an EM shower, and a matching cluster in the FT-Hodo was required [57].

For the scaling behaviour studies and d_{sss} upper limit of cross-section work, an electron was required in the FD ($\theta = 5$–35°). To confirm this, a track in the FTOF system was used to determine the position and energy deposited in the ECAL to confirm the particle specie.

Each detector involved in the CLAS12 trigger has different programmable features to adapt the trigger to different subsystems and maintain a high livetime. Other quality control measures are taken, one example is the CLAS12 event display (ced). The ced observes a limited number of single events to give the shift workers access to information on any problematic detector components and act immediately. Additionally, occupancies for a large number of the detector subsystems are checked via monitoring histograms, these also have some basic analysis plots that can be compared with historic results.

3.6 Data

There are many run groups in CLAS12, each linked to a particular experimental proposal. The two groups whose data we use in this research are Run Group A (RGA) and Run Group B (RGB). The main difference between RGA and RGB was the target, liquid hydrogen and liquid deuterium were used respectively. These run groups also had multiple stages of beam time where different configurations or setups were used, these are called run periods. This research contains results from the run periods in Tabs. 3.1 and 3.2. Inbending refers to when the magnet polarity bends negative particles towards the beamline and outbending away.

Table 3.1 Configurations for RGA run periods.

Run Period	Target	Beam Energy [GeV]	Torus polarity
Fall 2018 Inbending	Liquid Hydrogen	10.6	Inbending
Fall 2018 Outbending	Liquid Hydrogen	10.6	Outbending
Spring 2019	Liquid Hydrogen	10.2	Inbending

Table 3.2 Configurations for RGB run periods.

Run Period	Target	Beam Energy [GeV]	Torus polarity
Spring 2019	Liquid Deuterium	10.6 or 10.2	Inbending

Chapter 4

Data Analysis Techniques

In this chapter, details will be given about the different analysis techniques that have been explored during these research projects. This begins with exploring different techniques for particle identification and how misidentified particles can be removed from a data sample. Following this is a description of how constraints can be applied to event selection. Finally, there is a discussion about the simulation of data and how it can be processed with realistic detector responses.

4.1 Particle Identification

Confidence in particle identification is incredibly important in scattering experiments such as these, otherwise, results lose validity. Although hardware performs particle identification, such as the FTOF or HTCC, choosing how to use the information from all the various detector systems can drastically increase the accuracy of particle identification. This can be done to reduce the effects that misidentification, ghost tracks (single tracks being counted more than once) and accidentals (noise in the detectors leading to an unphysical particle track being constructed) cause on the overall result. First, we consider the base-level particle identification performed by CLAS12 which is the event builder PID.

4.1.1 Event Builder PID

In CLAS12's Event Builder Particle Identification (EB PID), the FTOF and DC are crucial for forward-going particles, and the CTOF and SVT are for large angle particles. As discussed in Sec. 3.2.2, we obtain β from time of flight detectors and momentum from tracking detectors. This information is

used to calculate a particle's measured mass, which is given by

$$m^2 = \frac{P^2}{\beta^2} - P^2, \tag{4.1}$$

where P is the momentum of the particle and m is its rest mass. This mass can then be compared with that of known particle species for identification. With the tracking and timing information, we can also determine the particle's four-momentum ($\tilde{P}$), which is given by

$$\tilde{P} = (P_x, P_y, P_z, E), \tag{4.2}$$

where P_x, P_y, and P_z are the x, y, and z components of the particle's momentum respectively and E is its total energy.

As shown in Fig. 4.1, as one goes to higher momenta, the β values of different particle species converge close together. This effect makes it harder for the EB PID to separate particle species at higher momenta, most notable for particles with similar masses such as Ks and πs (495 MeV and 140 MeV/c respectively). The main limiting factors for separating particle species using β are the timing resolution of the TOF detector, and the momentum resolution of the tracking detectors, as discussed in Sec. 3.2.2 and 3.2.3. The uncertainty in the EB PID comes from the difference between the measured β of detected particles and the theoretical β for the given particle species. This is given as the number of standard deviations (σ) they are apart, called χ^2_{PID}.

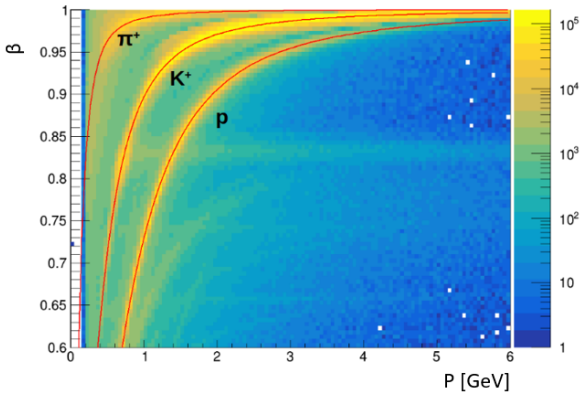

Fig. 4.1 β vs P for positive particles, theoretical values shown with red lines for π^+, K^+, and p.

4.1.2 χ^2_{PID}

Applying constraints on the χ^2_{PID} reduces the error associated with the particle identification. Figure. 4.2 shows how the various χ^2_{PID} levels look on a β vs P distribution for particle tracks identified by the EB PID as protons. While these cuts remove a large area of the 2D distribution, the reduction in statistics is low as the events are mostly concentrated in a very narrow band close to the theoretical values for a proton.

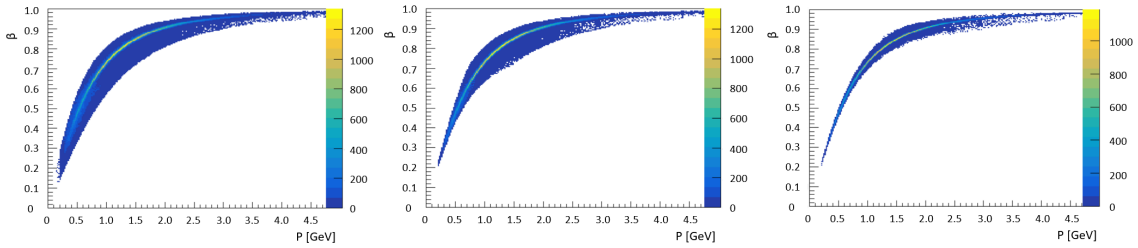

Fig. 4.2 Effect of $\chi^2{}_{PID}$ constraints. Original EB PID (left), $|\chi^2{}_{PID}| < 3$ (middle), and $|\chi^2{}_{PID}| < 1$ (right). (RGA Spring 2019 inbending data).

4.1.3 Out of time π Problem

Section. 4.1.1 highlighted how the vertex time for an event is used to determine a particle's β, this comes from the trigger particle in an event. Particles are grouped into events and associated with these trigger particles, usually the scattered electron. The electron beam comes in bunches every 4 ns, these detected particles can be associated with a scattered electron from the wrong beam bunch, making their vertex time incorrect. When this occurs, the time of flight is incorrect, leading to a miscalculation of the particle's velocity and therefore β. Often this produces a bad EB PID determination. This is a common problem for πs from the wrong beam bunch being misidentified as Ks, an issue dealt with a lot in this research.

These misidentified πs cross over the mass of a K on a calculated mass vs P distribution, as appears in Fig. 4.4 as horizontal bands at $P \approx 0.9$ GeV/c, making it difficult to separate these two species. This out of time π problem mostly occurs at lower momentum and so one method to remove these is to perform a cut on the momentum of the particles; this removes most of the bands of misidentified πs but it can also remove a lot of true kaons in the process. For the research on the very strange dibaryon and scaling behaviour of strangeness, statistics are very low at $S = -3$, a lot of the detected kaons are also low momentum. Therefore, this simple low momentum cut is not appropriate

for this research and an alternative must be used instead such as the novel approach described in Sec. 4.3.

4.2 Event Selection

Event selection is crucial to ensure that the channel observed is the one of interest, and is done with a few different techniques including topology, missing mass, and invariant mass.

4.2.1 Topology

Topology is the most basic form of event selection, choosing events that have given multiplicities of each particle type detected in the final state. Different topologies of the same decay channel might be explored for several reasons: low statistics, kinematics, and detector efficiencies are just some of these. There are two main types of topologies: exclusive, where all the final state particles are detected and inclusive, where only some of them are detected.

4.2.2 Missing Mass

Missing mass uses conservation of four-momentum to reconstruct undetected particles, it can also confirm the exclusivity of the reaction channel selected. This is done by subtracting the four-momenta of the detected final state particles from that of the initial reactants (beam and target), we can then deduce the remaining momentum of our undetected particles. For example, in the decay shown in Fig 4.3, by subtracting the outgoing particles (e', K^+) from the original beam and target, the Λ can be reconstructed without detecting any of its decay products. The mass of the Λ (m_Λ) is given by

$$\begin{aligned} \tilde{P_\Lambda} &= \tilde{P_{beam}} + \tilde{P_T} - \tilde{P_{e'}} - \tilde{P_{K^+}} \\ m_\Lambda &= \sqrt{(E_{beam} + m_T - E_{e'} - E_{K^+})^2 - |\overrightarrow{P_{beam}} - \overrightarrow{P_{e'}} - \overrightarrow{P_{K^+}}|^2}, \end{aligned} \tag{4.3}$$

where $\tilde{P_\Lambda}$, $\tilde{P_{beam}}$, $\tilde{P_T}$, $\tilde{P_{e'}}$, and $\tilde{P_{K^+}}$ are the four-momenta of the Λ, beam, target, scattered electron, and K^+ respectively. The total energy of the particles is represented by E_{beam}, $E_{e'}$, and E_{K^+} for the beam, scattered electron, and K^+. The target is stationary, so its total energy is from its mass (m_T). The magnitude of the three-momentum of the beam, scattered electron, and K^+ is represented by $\overrightarrow{P_{beam}}$, $\overrightarrow{P_{e'}}$, and $\overrightarrow{P_{K^+}}$ respectively. As mentioned above, there are a lot of reasons why particles in a given

event might not be detected, and so missing mass is a very useful tool to find out information about those undetected particles.

4.2.3 Invariant Mass

Another technique that uses conservation of momentum is invariant mass, but in this case, we use the summation of decay products' four-momentum instead of looking at the excess momenta. Unstable particles have a finite lifetime and can decay prior to reaching experimental detectors, such as Λ. However, if we can detect their decay products then we can reconstruct them. Similarly to the missing mass discussion, the undetected Λ in Fig. 4.3 can again be reconstructed but this time by combining the four-momentum of the proton ($\tilde{P_p}$) and π^- ($\tilde{P_{\pi^-}}$). The mass of the Λ is also given by

$$\begin{aligned} \tilde{P_\Lambda} &= \tilde{P_{\pi^-}} + \tilde{P_p} \\ m_\Lambda &= \sqrt{(E_p + E_{\pi^-})^2 - |\overrightarrow{P_p} + \overrightarrow{P_{\pi^-}}|^2}, \end{aligned} \tag{4.4}$$

where E_p and E_{π^-} are the energies of the proton and π^- respectively. The magnitude of the three-momentum of the proton and π^- is represented by $\overrightarrow{P_p}$ and $\overrightarrow{P_{\pi^-}}$ respectively.

Invariant mass is well suited for reconstructing decayed particles but it requires the detection of all of its decay products, which is not always possible due to the reaction kinematics or the angular acceptance of the detector systems involved. Using missing mass can be more successful as detection of all the decay products is not required, however, the reconstruction is usually not as reliable as invariant mass. A combination of these techniques can be used to ensure a relatively pure event sample.

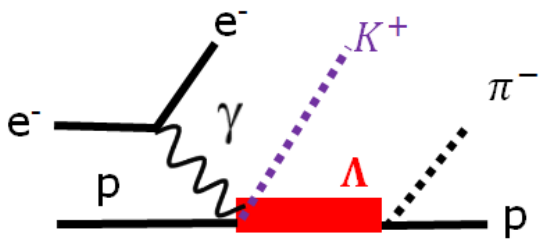

Fig. 4.3 Decay channel for strangeness -1, electron on proton target produces K^+ Λ, with Λ decaying into a proton and π^-.

4.3 Kaon Identification Method

As this research revolves around strangeness and kaons, it is very important that a clean sample of kaons are selected. A novel technique has been developed in order to improve the identification of kaons beyond the EB PID. This is done to reduce the effects of the out of time πs, other misidentified particles, ghost tracks and accidentals.

We only consider K^+s in the FD with a $|\chi^2| < 3$, this is done to remove any obvious background contributions or very poorly reconstructed K^+s. To reduce the impact of higher momentum πs leaking into our K sample, we look at a similar 2D distribution for π^+s in the FD with $|\chi^2| < 3$. A basic fit was performed on this and any of the particles identified as Ks that fit this pion condition were also removed from the sample. Generally, we require $\chi^2_K < 3$ and $\chi^2_\pi > 3$.

With these K^+s, first, we calculate their TOF mass using the measured β from FTOF and measured momentum from the DC as detailed in Sec. 3.2.2 & 4.1.1. Comparing this to the momentum of these particles as in Fig. 4.4, the effect of these misidentified tracks is clear. Most notable are the horizontal bands at approximately 1.2 GeV and below 0.9 GeV, which are caused by out of time π^+s. However, using just these variables it is not possible to actually separate the misidentified from the true K^+s on an event by event basis[1]. Nevertheless, we can weight the events based on the proportion of true to misidentified K^+s, enabling a significant reduction in the effects these cause.

In order to determine this ratio, a 2D momentum-dependent fit is produced for the EB K^+s which can then be used to ascertain the abundance of each for a given momentum and calculated mass. It would be near impossible to accurately predict the distribution and abundance of the background where there are large contributions. However, we know for true kaons that we expect a smooth distribution of abundance as a function of the kaon's momentum, and also that the resolution will worsen consistently as momentum increases. Using this knowledge, we can fit the distributions for true kaons in areas with low background contributions, then extrapolate this to the areas with significant background to extract the abundance of correctly identified kaons. For this reason, the previously described horizontal bands at 1.1–1.3 GeV and below 0.9 GeV are not included when producing the initial 2D fit. This produces a momentum-dependent distribution for the true kaons which can be extended across those regions, assuming anything else is misidentified.

[1] As mentioned in Sec. 3.2.2, there is a Cherenkov detector (RICH) capable of performing reliable kaon-pion separation, however, only one of the six sectors in CLAS12 was equipped with this incredibly useful device at the time of data collection.

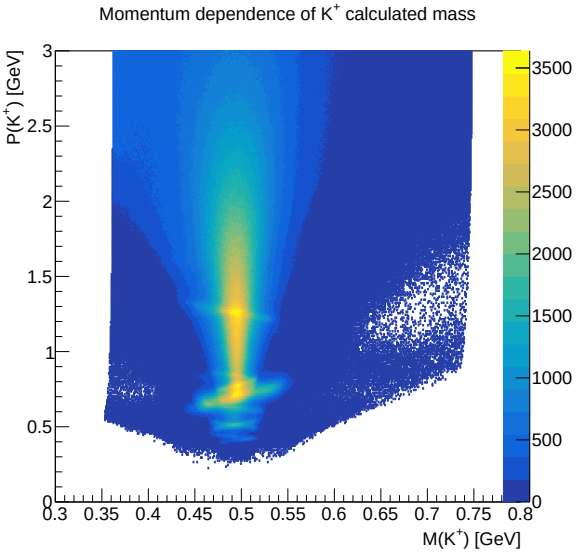

Fig. 4.4 Momentum dependence of EB K^+ calculated mass (RGB Spring 2019 Inbending data).

To produce the 2D fit, we must look at the 1D distributions of the calculated mass for varying K^+ momentum bins. The function that is used to fit the 1D distributions consists of a double Gaussian for the true kaons, a Gaussian for π^+s, and a decreasing 1st-order polynomial for random background contributions from ghosts and accidentals. Due to the resolution effects of the DC and FTOF, both of which are used for identification, a single Gaussian is not sufficient to describe the overall resolution of true kaons. Both these Gaussians have a fixed mean at the mass of the kaon, due to them originating from the same particle.

As π^+s and K^+s have a similar mass, 0.140 and 0.494 GeV/c respectively, their calculated masses can overlap for the given resolution. This is why a Gaussian has been included in the fit for the π^+ contributions that are incorrectly identified as K^+. The magnitude of the Gaussian scales with momentum due to increases in contributions from misidentified π^+s.

The overall fit function is given by

$$\begin{aligned}\text{Kaon fit function} = & A_1 \ \exp[-0.5(\frac{\mu_K - 1}{\sigma_K})^2] + A_1 A_2 \ \exp[-0.5(\frac{\mu_K - 1}{2\sigma_K})^2] + \\ & A_3 \ \exp[-0.5(\frac{\mu_\pi - 1}{\sigma_\pi})^2] + \\ & Bx + C,\end{aligned} \tag{4.5}$$

where for the true kaon fit (red), A_1 is the amplitude of the first Gaussian, μ_K is the mean for both, σ_K is the standard deviation for the first Gaussian, and A_2 is the ratio between the amplitude of the

second Gaussian and the first. The standard deviation of the second Gaussian is assumed to be twice the width of the first Gaussian. For the misidentified pions (blue), A_3 is the amplitude of the Gaussian, μ_π is the mean, and σ_π is the standard deviation. For the random background contributions (black), B is the slope and C is the y-intercept of the linear function. This describes the overall distribution of the particles identified as K^+s by the event builder PID well. An example of this overall fit is shown for the momentum bin 2.45-2.46 GeV in Fig. 4.6.

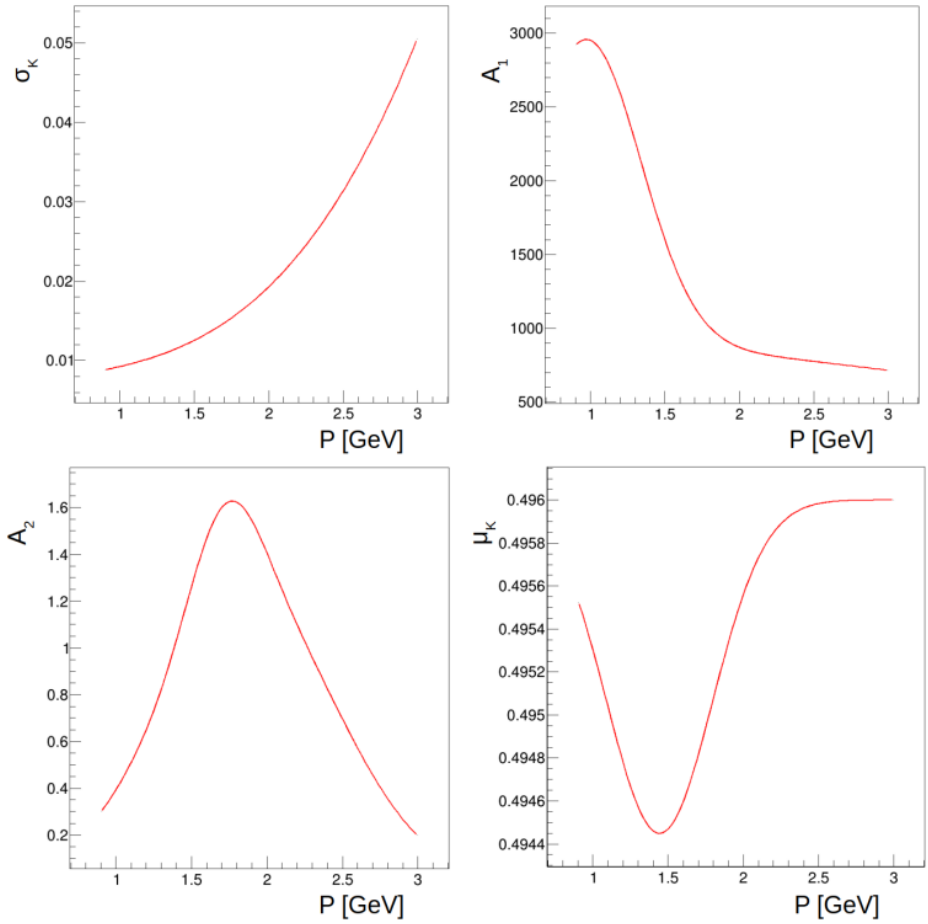

Fig. 4.5 A 2D fit was produced for the particles determined by the event builder PID as K^+s to ascertain the abundance that were correctly identified. The momentum dependence of the parameters used for the true kaon component of the fit function in Eq. (4.5) are shown here.

Similar fits to the one in Fig. 4.6 are produced across a large number of kaon momentum bins to build up a momentum-dependency for the true kaons. The momentum dependence of the parameters of the true kaon component are presented in Fig. 4.5. These are used to build up the 2D distribution for true kaons, as mentioned previously, anything else from the data is assumed to be misidentified. The ratio between the true kaons and misidentified is calculated for this 2D distribution, this is shown

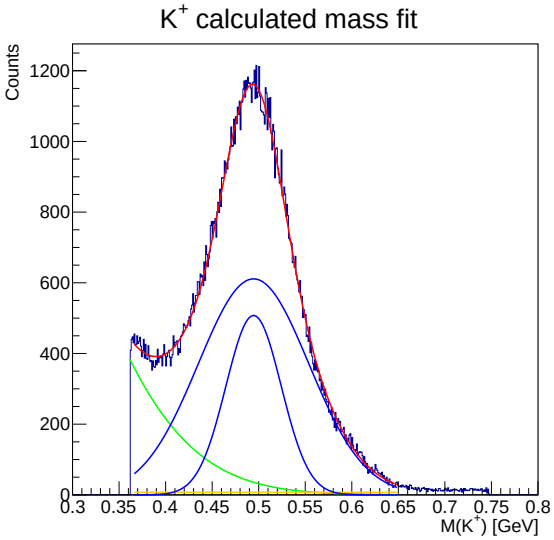

Fig. 4.6 Fit of K^+ calculated mass for P(K^+)=2.45-2.46 GeV. Red: Total fit, Blue: Two true kaon Gaussians, Green:π^+ background Gaussian, Orange: Random background 1st order polynomial. (RGB Spring 2019 Inbending data).

in Fig. 4.7. Next, each event is weighted by the ratio in this plot based on that event's kaon momentum and calculated mass.

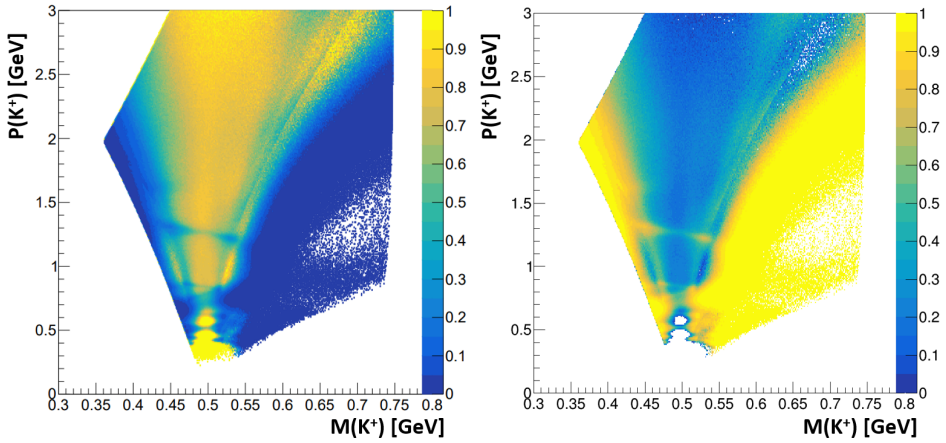

Fig. 4.7 Ratios of true (left) and misidentified (right) K^+s to total EB K^+s (RGB Spring 2019 Inbending data).

The result of this momentum-dependent background subtraction is shown in Fig. 4.8 for the reaction $ep \rightarrow e'pK^+X$. As detailed previously, Ks and πs are easily misidentified and thus there are large contributions in this figure from π contamination. The first peak in the original data (blue) of Fig. 4.8 at approximately 0.9 GeV, comes from the reaction $ep \rightarrow e'\Delta^+ \rightarrow e'(n\pi^+)$, where the

π^+ is incorrectly identified as a K^+ by the EB PID. This results in a peak for the remaining neutron shifted by the difference in the π and K masses. After the background subtraction is applied, the resulting distribution (red) has far fewer events in the region of this shifted neutron, highlighting the effectiveness of this technique. Approximately 40–50% of this neutron peak is removed, while only losing $\approx$ 15% of the hyperon signals. Additionally, this approach has removed almost all events that were below the threshold for this channel which are either misidentifications or unphysical reconstruction.

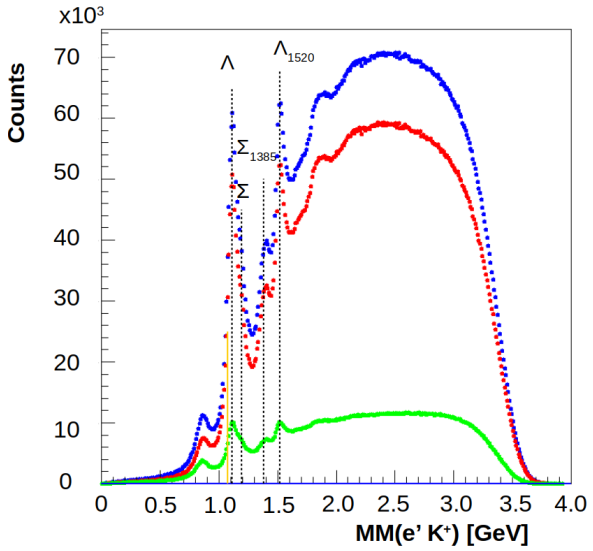

Fig. 4.8 Missing Mass of $e'K^+$ X. Blue: original data, Green: Background, Red: Signal (RGA Fall 2018 Inbending data).

In this background distribution, there are some hyperon peaks visible, however, these are not necessarily good events leaking into our background. Charged kaons can decay in-flight before reaching the detectors, due to their finite lifetime, this leads to the incorrect reconstruction of the kaons' four-momentum and then the resulting hyperon. This results in broader peaks, which can be seen in the background distribution (green) in Fig. 4.8. The kaon's decay products take longer to reach the detectors than a kaon that has not decayed would, which leads to a longer time-of-flight being measured. With a larger time-of-flight, the calculated mass would be lower. This leads to an asymmetric distribution as can be seen in the top left corner of Fig. 4.4. The fit used in this technique for the true kaons is a Gaussian (symmetric), therefore, the majority of the kaons that decay before the TOF detectors are assumed as background.

4.4 Simulations and Acceptance Corrections

Simulations are an incredibly useful tool in physics analysis, allowing researchers to study background contributions, expected kinematics, and detector acceptances and efficiencies. The simulations presented in this thesis are produced using CLAS12elSpectro [58], which is an interface for the elSpectro event generator that aligns well with the CLAS-mcgen. The elSpectro event generator allows for sampling the phasespace distributions of any final state in electron scattering interactions.

Simulations are crucial for cross-section measurements as they are independent of detector setup or particle detection. As discussed in Sec. 1.5, acceptance and efficiency corrections must be made to correct the yield (abundance detected) to what was actually produced. To do this, accurate information is needed regarding the dimensions and placement of detectors as well as their responses. If we can simulate reactions with known kinematics and determine what happens if those particles were passed through the detector setup, then it is possible to use this information to make acceptance and efficiency corrections to our experimental data.

Geant4 Monte-Carlo (GEMC) makes this possible, it simulates particles and how they interact with matter, for detailed explanations of the workings of GEMC, see Ref. [59]. A user can define the different detector volumes and their locations relative to one another and provide GEMC with a basic Monte-Carlo simulation of the reaction channel of interest, these events will be passed through the detector volumes. Realistic detector responses can also be implemented, and GEMC will provide the user's desired output, this way it can match the usual experimental data format for easy analysis and comparison. Finding the ratio between the simulation data passed through GEMC and the original, pure Monte-Carlo simulation gives the acceptance correction that should be applied to experimental data. The acceptance correction is given by

$$A = \frac{\text{Processed through GEMC}}{\text{Pure MC}}, \tag{4.6}$$

where A is the product of the detector acceptances and efficiencies.

Chapter 5

Analysis and Results I: Exotic Mesons

This chapter explains the analysis process and results for the exotic meson search, looking at conditions applied to experimental and simulation data, the techniques and software used to produce the angular distribution moments, and the first look at potential meson contributions for this work.

5.1 Particle Selection Criteria

This research involves a virtual photon interacting with a nucleon in the target. The probability of a photon interacting with a nucleon is dependent on the nuclear form factor, which is the Fourier transform of the charge/magnetisation distribution[60]. The form factor (F(Q^2)) is inversely proportional to Q^2, in its simplest form it is given by

$$F(Q) = \frac{1}{(1+\frac{Q^2}{\Lambda^2})^2}, \tag{5.1}$$

where Λ is 0.71 GeV, which corresponds to the radius of the nucleon ($\sim$ 0.81 fm) . Hence, the coupling is at a maximum when $Q^2 = 0$, corresponding to a real photon. Therefore, scattered electron tracks are only taken if they are within the FT acceptance, meaning we have a low Q^2 virtual photon or quasi-real photon. Choosing events with low virtuality photons instead of high ones provides greater cross-sections. From a theoretical perspective, real photons are simpler to deal with than virtual. This is because real photons are on-shell and their form factors are far more understood than the off-shell of a virtual photon.

As discussed in Sec. 1.4, the reaction channel $\gamma^* p \to pX \to p(K^+K^-)$ is used in this work. Both the K^+ and K^- are required to be detected in the FD, which has an angular coverage of $\theta = 5 - 45°$. Kaons going into the CD are not considered due to the momentum resolution of the SVT of 6% compared with the DC of 1% for particles in the FD. Protons have better separation than kaons do from other particle species, this is highlighted in Fig. 3.10, so the momentum resolution does not need to be as high to accurately identify them. For this reason, protons are allowed in the FD or CD, preventing further reductions in statistics due to kinematic constraints put on the data.

5.2 Event Selection Criteria

An exclusive topology was chosen for this research, requiring the detection of at least 1 e^-, 1 p, 1 K^+, and 1 K^-. This reaction channel favours small momentum exchange, therefore, the proton momentum is close to zero and often will not reach an active detector system or even leave the target. Additional cuts were applied beyond basic PID and topology selections, they are detailed in Tab. 5.1, here *MM* is the missing mass.

- Constraint one was implemented to ensure that the exclusive channel was selected.
- Constraint two was applied to make sure that the proton detected was not misidentified and to further confirm that no additional particles were detected.
- Cuts were placed on the photon energy in the region where simulation and data agree well, shown in Fig. 5.3.

Table 5.1 Constraints on events for exotic meson search.

Constraint	Condition
1	$\lvert MM^2(e'pK^+K^-)\rvert < 0.01$ [GeV^2/c^2]
2	$0.7 < MM(e'K^+K^-) < 1.1$ [GeV/c]
3	$5.9 < E_{\gamma^*} < 9$ [GeV]

5.3 Determination of Moments

The extended maximum likelihood (EML) approach was used for the determination of the meson's angular distribution moments, details on this technique are explained in Ref. [61]. Maximum

likelihood fits require probability density functions (PDF), to achieve this the functions need to be normalised into PDFs. For angular distribution moments, the functions we are fitting are a product of the detector acceptance and the spherical harmonic moments, we consider $S(\theta,\phi)\times\mathbb{A}(\theta,\phi)$, where S and $\mathbb{A}$ represent the spherical harmonic and acceptance components respectively. To produce our PDFs, we must integrate $S\times\mathbb{A}$ across θ and ϕ, this is done through Monte Carlo integration [62]. More specifically, this involves taking the Monte Carlo simulations that were measured after passing through the Geant4 Monte Carlo (GEMC), giving the $\mathbb{A}$ part, then summing up $S(\theta,\phi)$ for the accepted events, providing us with the integral of $S\times\mathbb{A}$.

As discussed in Sec. 4.4, CLAS12elSpectro [58] was used to produce the Monte Carlo (MC) simulations for these meson studies. The configuration was set to match the run period of the experimental data, RGA fall 2018 outbending, so the polarity and various trigger conditions were the same. A total of 100 million events were simulated for this study with the reaction channel $ep\rightarrow e'pK^+K^-$.

Next, the simulated events were put through CLAS's GEMC, which applies acceptance and realistic detector responses to produce output files similar to that of the experimental data, details of this can be found in Sec. 4.4. By doing this, we can see what we should expect from these two kaons at a wide variety of kinematics and compare them with what we see in experimental data.

Verification of our MC studies needs to be performed prior to the moment studies. This is done to ensure the resolution and responses of the detectors are well reproduced and we undertook several studies to this end. Various distributions were compared between the experimental data and MC simulation to ensure that they agreed well. The first variable was $MM^2(e'pK^+K^-)$ to see if in the experimental data, the correct reaction channel was being selected. As in Fig. 5.1, the simulation has a very narrow peak at zero, since only events with the exact reaction were simulated. On the other hand, the experimental data distribution is much broader, and while it still has a peak at zero, many other background contributions lead to this wider distribution. Firstly, there can be events with more particles in the final state than the requested four (e,p,K^+K^-), leading to values above zero. Additionally, particles can be misidentified by the event builder (EB) PID, e.g. the much more abundant pions, which are often incorrectly identified as kaons.

Next, we look at the $MM(e'K^+K^-)$, which is the mass of the reconstructed proton. This is checking that the EB PID correctly identified the proton, also verifying the event did not have high

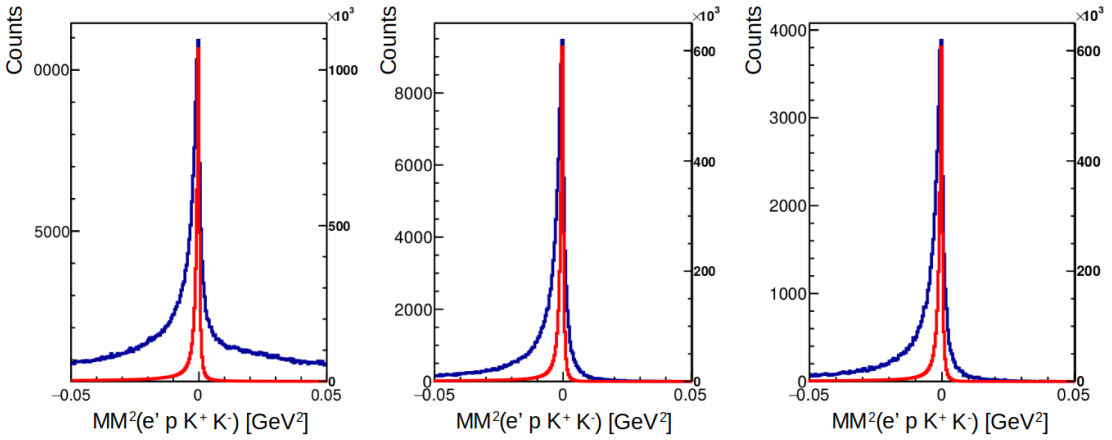

Fig. 5.1 Comparison between experimental data (blue) and simulation (red) for the reconstruction of the exclusive reaction before cuts (left), after a cut on the reconstructed proton (mid), and after a cut on the reconstructed proton and the photon energy (right). Experimental data from RGA Fall18 Outbending.

multiplicity. The mass of the reconstructed proton is given by

$$m_p = \sqrt{(E_{\gamma^*} + m_T - E_{K^+} - E_{K^-})^2 - |P_{\gamma^*} - P_{K^+} - P_{K^-}|^2}, \tag{5.2}$$

where E_{K^-} and P_{K^-} are the energy and momentum of the K^-. Once again, the simulation peak is somewhat narrower as expected in Fig. 5.2. The experimental data has other contributions at higher masses than the proton, some of which come from other reaction channels such as the shoulder at 1.2 GeV. This likely comes from K^+K^- in-flight production with simultaneous excitation of the proton target into a $\Delta(1232)$ resonance.

One of the outcomes of this experiment is to observe the proper t-dependence of the reaction by extracting the exact photon distribution. Therefore, it is not necessary that the MC simulation photon energy distribution reproduces that of the experimental data exactly. However, it is important that our acceptance and efficiency corrections are not largely model dependent, so these distributions should have some similar resemblance.

A notable feature of Fig. 5.3, is the apparent threshold of $E_\gamma \approx$4.5 GeV, which comes from the trigger conditions of CLAS12. The decreasing slope after this threshold comes from a combination of the $\frac{1}{E_\gamma}$ relationship and the t-dependence of the reaction channel. After the same cuts on the exclusive reaction and reconstructed proton are applied to the simulation, Fig. 5.3 (right), the experimental data and MC simulation do not have a perfect agreement, but it is sufficient for this initial study..

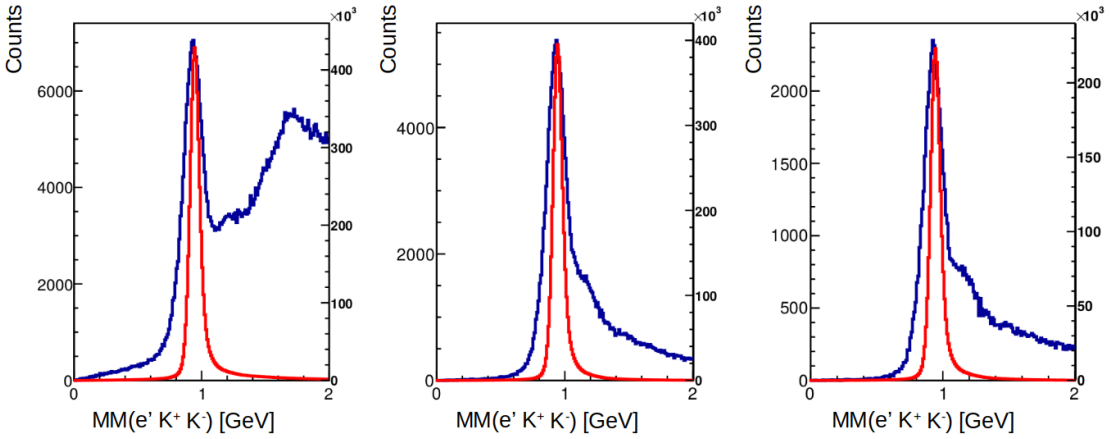

Fig. 5.2 Comparison between experimental data (blue) and simulation (red) for the reconstruction of the proton before cuts (left), after a cut on the exclusive reaction (mid), and after a cut on the exclusive reaction and the photon energy (right). Experimental data from RGA Fall18 Outbending.

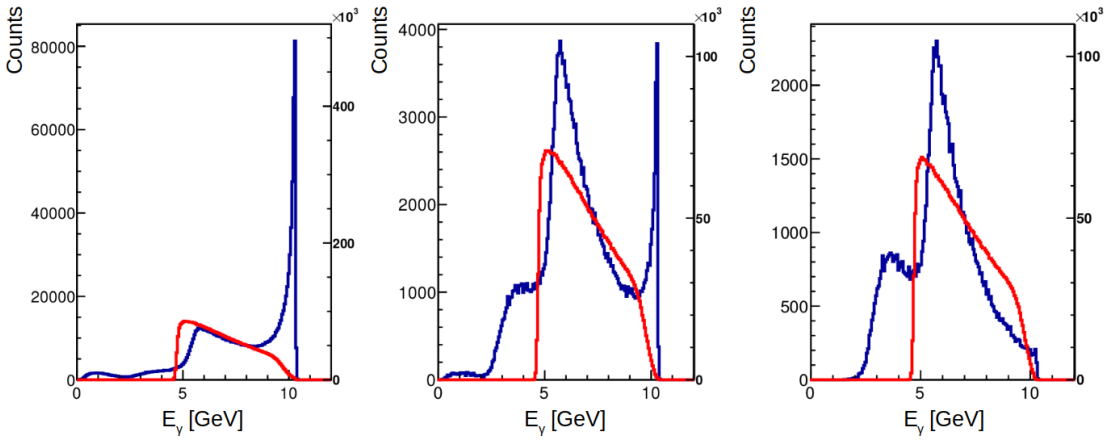

Fig. 5.3 Comparison between experimental data (blue) and simulation (red) for reconstruction of photon energy E_γ before cuts (left), after cut on exclusive reaction (mid), and after cut on exclusive reaction and reconstructed proton (right). Experimental data from RGA Fall18 Outbending.

Determination of the angular distribution moments requires information on the decay angles of the reaction, here we solely assume the origin of the K^+K^- pair is from one mesonic resonance produced in-flight. This analysis considers two different rest frames of the resonance X, the Helicity frame and the Gottfried-Jackson (GJ) frame. For the Helicity frame, shown in Fig. 5.4, the normal to the production plane gives the y-axis ($\overrightarrow{y} = P_p$ x P_γ), and the x-axis is given by ($\overrightarrow{x} = \overrightarrow{y}$ x $\overrightarrow{z}$), here the z-axis is anti-parallel to the recoiling proton. The GJ frame, presented in Fig. 5.5, has the same definitions for the x- and y-axis, however, here the z-axis is along the direction of the photon [63]. This thesis research determines the decay angles using the four-momentum of the K^+.

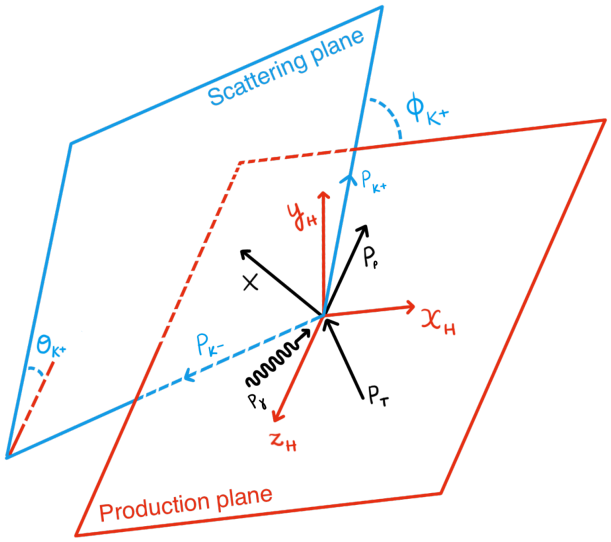

Fig. 5.4 Decay angles of the K^+ in the Helicity reference frame: θ_{K^+} is the angle between the kaon's four-momentum and the z-axis, ϕ_{K^+} is the angle between the scattering plane (blue) and the production plane (red) [64].

Brufit [65] is an event-based maximum likelihood fitting package that is based around RooFit, it was designed to enable the analysis of hadron physics surrounding scattering reactions. It uses the decay angles of the K^+ (defined in Figs. 5.4 and 5.5) to determine the angular distribution moments of the meson X that decayed into the kaon pair. This involves many complex theoretical calculations, details of which can be found in Ref. [66]. Examples of these decay angle distributions and brufit's fitting of the simulation to the experimental data are shown in Fig. 5.6.

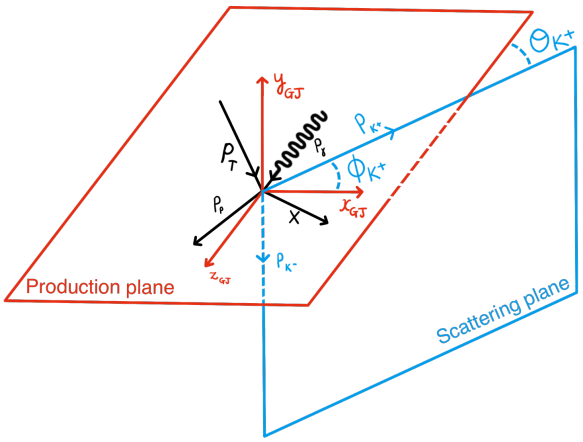

Fig. 5.5 Decay angles of the K^+ in the Gottfried-Jackson (GJ) reference frame: θ_{K^+} is the angle between the kaon's four-momentum and the z-axis, ϕ_{K^+} is the angle between the scattering plane (blue) and the production plane (red) [64].

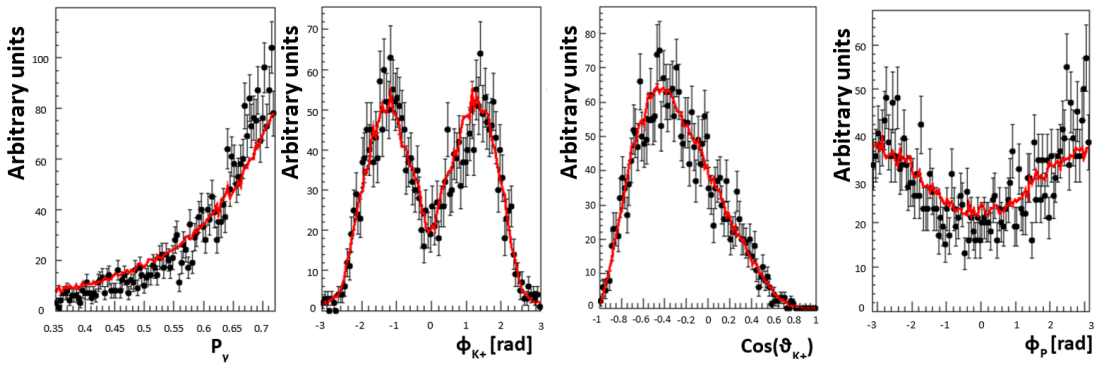

Fig. 5.6 Decay angles for K^+K^-: $\cos(\theta_{K^+})$ is the cosine of the angle between the z-axis and the K^+ momentum vector in the GJ frame, Φ_{K^+} is the angle between the production and scattering planes, Φ_P is the azimuthal angle of the production plane relative to the scattering plane, and P_γ is the photon polarisation.

5.4 Results

The results of the fit for the energy dependence of the first 29 moments of the K^+K^- system are shown in Fig. 5.7 and 5.8. The statistical errors in these distributions arise from a combination of the statistical fluctuations in the experimental data and the simulation. Before publication, systematic studies will be performed but they are not included at this stage. This will involve varying the cuts applied to the data as well as various selection criteria, and then observing the effect on the moments. As detailed in Sec. 1.4, we expect to see sharp changes and possibly sign flips in these distributions where we have large contributions from parent mesons, then smooth distributions elsewhere. Kaons are spin-zero particles, thus, the angular momentum between the kaons entirely originates from the spin of the mesonic resonance, e.g. a p-wave is $L = 1$, therefore, the parent meson has a vector sum of angular momentum and spin, $J = 1$. As discussed in Sec. 1.4, without partial wave analysis it is not possible to say with complete confidence what meson contributions there are, but from the moments alone, hypotheses can be made.

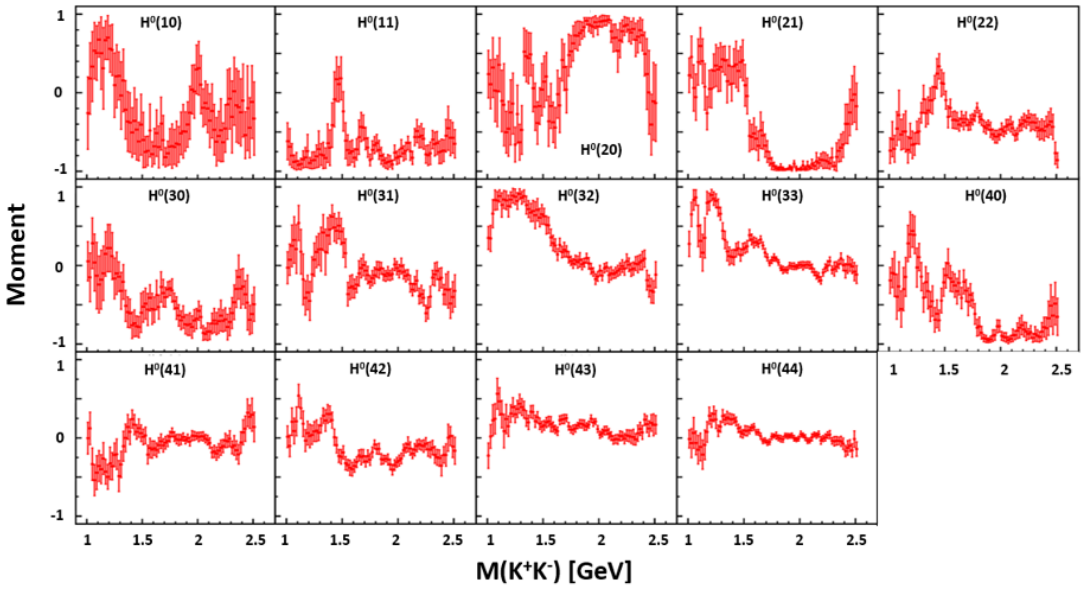

Fig. 5.7 Moments for K^+K^- of the 0th Hamiltonian projections (H^0) as a function of the invariant mass of the two detected kaons.

In the moment $H^0(42)$ distribution, we only have contributions from D-waves (spin 2 mesons), as highlighted in the equations in Eqs. (A.1) & (A.2), these can have quantum numbers $J^{PC} = 2^{++}$ and $I^G = 0^+$ or 1^- from Tab. 1.4. There is a clear change in the magnitude of the moment at approximately

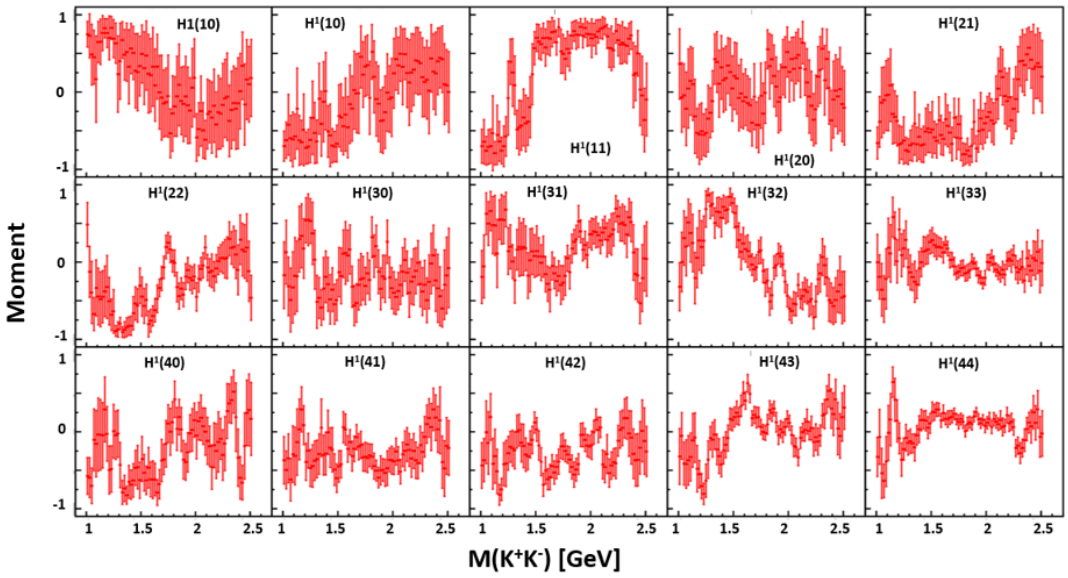

Fig. 5.8 Moments for K^+K^- of the 1st Hamiltonian projections (H^1) as a function of the invariant mass of the two detected kaons.

1.3 GeV, based on the quantum numbers allowed this is likely to come from the $f_2(1270)$ (isospin zero) and/or $a_2(1320)$ (isospin one) states. In the same moment, there is a narrow structure at $M(K^+K^-)$ = 1.1 GeV, and there are no unflavoured mesons with three- or four-star ratings in the PDG at this mass; the nearest to this would be the $f_2(1270)$ at a mass of 1275.5 MeV, this is over 150 MeV away from this clear structure. This suggests that this work has potentially observed a new meson, however, partial wave analysis is needed to confirm this, since other physical background contributions, such as Deck diagrams, cannot be excluded at this stage.

Moment $H^1(10)$ is the sum of interferences between P- and D- waves, and interferences between S- and P- waves, meaning sharp changes in this distribution come from mesons with $J = 1$ and 2 or $J = 0$ and 1 with similar masses. There is a sharp change at $M(K^+K^-) \approx 1.7$ GeV, this could suggest an interference between $\rho(1700)$ and $f_0(1710)$.

Moment $H^1(40)$ is comprised of just D-waves and so for this case is made up of solely spin $S = 2$ mesons. There are a lot of structures appearing in Fig. 5.9 between $M(K^+K^-) = 1.8$–2 GeV with multiple flips in the sign of the gradient, this could be attributed to the $f_2(1950)$ and $f_2(2010)$ mesons. Additionally, there is a sharp change at $M(K^+K^-) = 1.3$ GeV suggesting possible contributions from $f_2(1270)$ or $a_2(1320)$, similar to that of the $H^0(42)$ moment.

$H^1(44)$ is another moment that is composed of only D-waves, so again looking for mesons with spin $S = 2$. Here there is a large fluctuation in the distribution shown in Fig. 5.10 at $M(K^+K^-) \approx 2.3$ GeV,

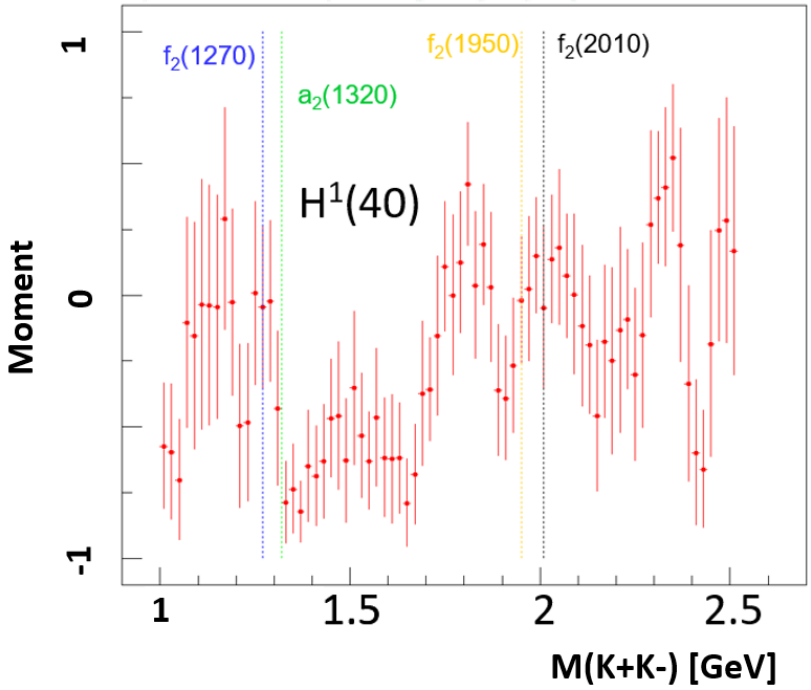

Fig. 5.9 Moment $H^1(40)$ for K^+K^- as a function of the invariant mass of the two detected kaons.

this might be attributed to the mesons $f_2(2300)$ or $f_2(2340)$. Another consideration is the possible glueball state $f_2(2200)$, detailed in Sec. 2.1. Because gluons are flavour blind, we expect a high branching of glueballs into kaons, similar to the hybrid mesons mentioned in Sec. 1.4.

Even before partial wave analysis has been performed, there is a great deal of promise in these moments with lots of clear structures visible at well-known meson masses as well as some unknown or not yet validated. This suggests the possibility of new mesons being observed by this research, however, verification studies through partial wave analysis are required to distinguish the different contributions to these moments.

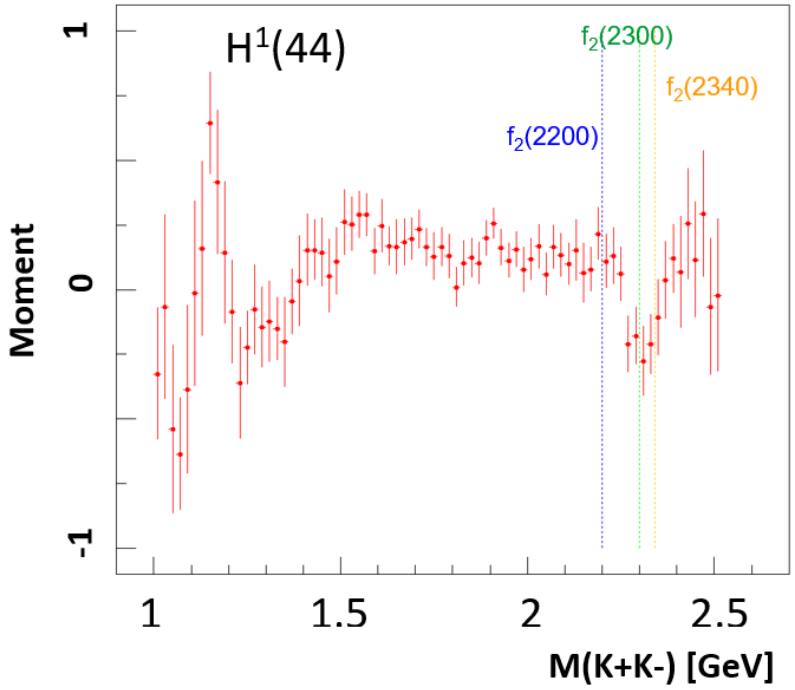

Fig. 5.10 Moment $H^1(44)$ for K^+K^- as a function of the invariant mass of the two detected kaons.

Chapter 6

Analysis and Results II: Scaling Behaviour Of Strangeness

This chapter will detail the analysis processes and results for the scaling behaviour of strangeness, starting with the event selection and reconstruction criteria; followed by the methods to determine scaling behaviour; and finally an overview of the results that came out of this research.

6.1 Particle Selection Criteria

The kinematics of these strangeness production channels, dictate that the majority of the kaons travel in a forward direction; this is especially the case in two and three kaon production, where the energy thresholds are higher. An MC simulation of the reaction $ed \rightarrow e'3K^+\Omega^-\Delta^- \rightarrow 3K^+(K^-\Lambda)(n\pi^-) \rightarrow 3K^+npK^-2\pi^-$ was produced to observe the angular acceptance of the final state particles. Figure. 6.1 shows the angular dependence of the three positive kaons for this reaction, with red lines highlighting the acceptance of the FD. There are few kaons in the region of the CD, at angles of θ >45°, therefore, including the CD in this analysis would add a very small phasespace coverage. Additionally, this would add large contributions from unphysical background due to the poorer resolution of the CD compared to FD, detailed in Sec. 3.2.3. Therefore, events with tracks in the CD were omitted from this analysis.

A further constraint was applied to eliminate trivial background in the event builder level through the use of a cut on the K^+s' $|\chi^2_{PID}| < 3$. To reduce these background contributions from misidentified kaons further, the kaon identification method described in Sec. 4.3 is applied.

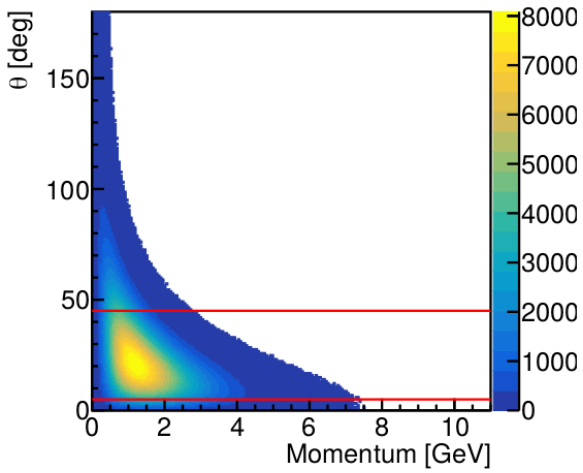

Fig. 6.1 Angular dependence of the three positive kaons in the reaction $ed \rightarrow e'3K^+\Omega^-\Delta^- \rightarrow 3K^+(K^-\Lambda)(n\pi^-) \rightarrow 3K^+npK^-2\pi^-$. Red lines at $\theta = 5$ and 45 ° indicate angular acceptance of the forward detector.

6.2 Event Selection Criteria

The only particles that are required to be detected in this research are the scattered electron and 1, 2, or 3 K^+s. The scattered electron, as well as any kaons, must go in the FD for the event to be selected. The FT was not used in the trigger during the RGB data collection period for more forward-going particles, otherwise the electron would also be allowed there.

6.3 Determination of Scaling Behaviour

The idea behind this study, as discussed in Sec.1.5, is to determine the suppression factor for strangeness production and elucidate kinematic regions with potentially enhanced strange exotic yields. Determination of suppression factors for strangeness production requires looking at the ratio between cross-sections of different strangeness multiplicities. As described in Sec. 1.5.1, we consider only kaon in-flight production reactions for convenience, where all baryon excitations are removed and any strange quarks are produced from vacuum by e-m process. Such reactions are incredibly appealing for theoretical predictions based on quark counting rules. The suppression for strangeness production in the regions where hyperon resonances are abundantly produced are also evaluated for completeness. Theoretical predictions of such reactions are difficult; however, observing the general cross-section behaviour can potentially direct us to possible exotics in the hyperon sector. Previously

discussed in sections 1.5.2 and 1.5.3, exotic channel couplings to protons and neutrons could be very different; strange dibaryons can also be excited on deuteron, but not on protons. Exploration of these exotic objects is performed by investigating strangeness production cross-sections in the ratios between proton and deuteron for all single-, double-, and triple-kaon production cases.

Prior to the determination of ratios, any unphysical background must be eradicated from the event samples. Utilisation of the kaon background subtraction technique, discussed below, was done for this. Contamination of other species in the CLAS12 event builder PID for kaons has been discussed in Sec. 4.1.1, and these misidentified particles have to be removed as much as possible to ensure accurate yields are obtained for given strangeness and kinematics. This was done using the method detailed in Sec. 4.3, however, there are still some traces of unphysical background left in our data sample. These are most notably seen as sub-threshold events, shown in Fig. 4.8, and these are not possible for the channel of interest. Although small background contributions remain after the subraction, this method is expected to provide a reasonable picture of the background events in the different kinematics. To investigate this effect further, the background contributions have been scaled up to match the sub-threshold events in the missing mass picture, as shown in Fig. 6.2, before being subtracted to emulate the removal of almost all background. Comparisons between the scaling produced with the original method and this 'enhanced background' technique can be attributed to the systematical uncertainty of our study. Section 6.4.2 will highlight that the difference between these two methods is not significant, showing the reliability of the ratio techniques used and their insensitivity to small background contributions. Therefore, the original background technique, without scaling, was used for the results shown in this chapter. Further to this, the peaks seen in the background distribution at known hyperon masses are observed because of kaons that decay in-flight before they reach the detectors. This is why the peaks appear broader than in the signal distribution and they should not be considered for these studies.

Next, depending on the ratios being taken, we must consider the factors from our original cross-section equation, Eq. (1.2), that need to be applied. The cross-sections for strangeness $S = 1$ (σ_{s1}) and $S = 2$ (σ_{s2}) production are given by

$$\sigma_{s2} = \frac{\mathbb{Y}_{s2}}{A_{s2}\phi\rho_T l},\ \sigma_{s1} = \frac{\mathbb{Y}_{s1}}{A_{s1}\phi\rho_T l}, \tag{6.1}$$

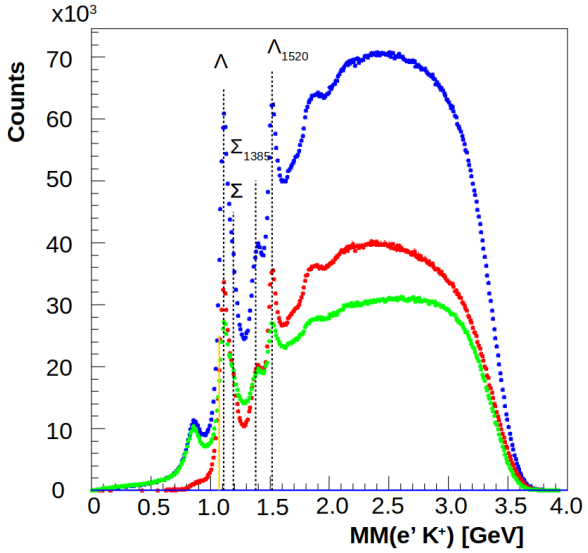

Fig. 6.2 Missing Mass of $e'K^+$ X. Blue: Original data, Green: Background scaled to sub-threshold background, Red: Signal, defined as the original data minus the normalised background (RGA Fall 2018 Inbending data).

where the variables denoted with a subscript $s1$ are for strangeness $S = 1$ production and those with a subscript $s2$ are for strangeness $S = 2$ production. For the strangeness suppression factor, this is a comparison between the same experimental data, so the total flux (ϕ), target density (ρ_T), and target length (l) are the same and all cancel out from Eq. (6.1). Therefore, the ratio of strangeness $S = 2$ and $S = 1$ production is given by

$$\frac{\sigma_{s2}}{\sigma_{s1}} = \frac{\mathbb{Y}_{s2} A_{s1}}{\mathbb{Y}_{s1} A_{s2}}. \tag{6.2}$$

Equation. (6.2) shows that for this result we only need to take a ratio of the two yields ($\mathbb{Y}_{s2}$, $\mathbb{Y}_{s2}$) with acceptance and efficiency corrections applied (A_{s1}, A_{s2}).

For the exchange meson isospin dependence and strange exotic baryon search, it is a comparison between two different run periods with the same experimental setup. These run periods have different flux and target material but everything else can be considered the same. The cross-section for strangeness production on a proton (σ_p) and deuteron (σ_d) target are given by

$$\sigma_d = \frac{\mathbb{Y}_d}{A\phi_d\rho_d l}, \; \sigma_p = \frac{\mathbb{Y}_p}{A\phi_p\rho_p l}, \tag{6.3}$$

where the variables denoted with a subscript d are for strangeness production on a deuteron target and those with a subscript p are for strangeness production on a proton target. Taking the ratio of these

two cross-sections gives

$$\frac{\sigma_d}{\sigma_p} = \frac{\mathbb{Y}_d \phi_p \rho_p}{\mathbb{Y}_p \phi_d \rho_d}. \tag{6.4}$$

The different electron fluxes and target densities of the proton and deuteron target data are taken into account, as dictated by Eq. (6.4), so the key difference between these data sets are now from differences in cross-sections for the production on proton, neutron, and deuteron. It is expected that the total cross-section on deuteron should be described by Eq. (1.4). The cross-section for interactions on a proton single-nucleon system should be the same for both targets. Therefore, any differences in the data sets should come from contributions of interactions on a neutron single-nucleon system or coherent interactions with the deuteron two-nucleon system . At the energy of this experiment, typical coherent cross-section on deuteron is $\approx 10^3$–10^4 times smaller than on a nucleon, which is why we primarily focus on the differences between interactions on the two single-nucleon systems.

To examine the non-resonant production, we look at the energy region above the resonances of strangeness one and two ($MM(e'K^+[K^+]) > 2$ GeV); this is not done for strangeness three as there are no conventional resonances. First, we only select events with missing mass above the threshold to get the total photon energy distribution shown in Fig. 6.3 (blue). This is further separated into two regions, the resonance region (red) and the 'non-resonance' region (green).

The resonance region, where we produce hyperons in this case, occurs predominantly at moderate energies and their production is heavily suppressed at high energies. Hyperons are generally low in mass, typically below 2 GeV, so reactions such as $\gamma p \to N^* \to Y K^+$ are prohibited for photons with energy of a few GeV because of a lack of N^* states with masses high enough. Another production mechanism for hyperons is from a K^+K^- pair produced in-flight, with a kaon scattering on the nucleon as a second vertex. This production mode is strongly suppressed by the vertex functions due to large momentum exchange. For the non-resonant K^+K^- in-flight production, the available phasespace rises with the photon energy, causing the domination of the non-resonant mechanism for high-energy photons. Figure 6.3 illustrates these features, with an abundance of resonant production (red) at lower photon energies, then a significant proportion of non-resonant production (green) at higher energies.

Due to the non-identical trigger conditions applied to the RGA (proton) and RGB (deuteron) experiments, the photon energy distributions are slightly different at the very low and very high energies. For this reason, we constrain our distributions between 4-9 GeV when comparing the two experiments.

Fig. 6.3 gives an indication of the photon energy threshold for producing particles with strangeness $S = -1$ (left), -2 (middle), and -3 (right). It is worth noting that in this work, all K^+s are required to go in FD ($\theta = 5$–$45\ ^\circ$). This means that the kaons have kinetic energy and are not at rest in the centre of mass (CM) reference frame, therefore, these thresholds are higher than production at rest thresholds [1]. The $S = -1$ threshold is below 4 GeV where we cannot accurately compare between proton and deuteron data due to different trigger conditions. The threshold for $S = -2$ appears to start at ≈ 4 GeV, and $S = -3$ only above 7.5 GeV.

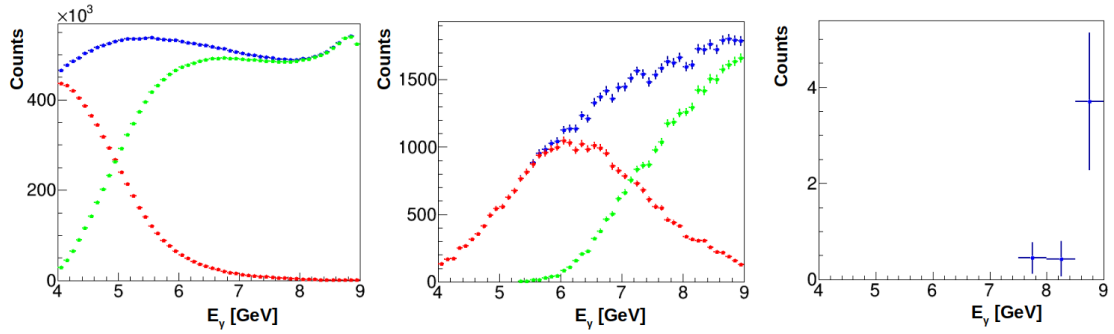

Fig. 6.3 Photon energy distribution of total (blue), resonant production (red), and non-resonant production (green) for events with one scattered electron and one (left), two (middle), or three (right) K^+s in the FD. Data from the RGB Spring 2019 Inbending run period used.

6.4 Results

This section will detail the findings of this research into the scaling behaviour of strangeness. Initial estimates for the suppression of strangeness production are presented, looking for an explanation for the lack of hyperons discovered. Interpreting the ratio of non-resonant kaon production on deuteron and proton will ascertain the isospin dependence of the exchange mesons involved. Finally, using scaling behaviour of strange production in the resonance region to search fo possible excited baryon states.

6.4.1 Strangeness Suppression

The ratio of cross-sections between strangeness 2 and 1 for the non-resonance region, shown in Fig. 6.4 (left) for proton (blue) and deuteron (red), asymptotically approaches $\frac{1}{100}$ for both targets, giving the

[1] Production at rest thresholds in photon energy are as follows: Strangeness 1= 0.91 GeV, Strangeness 2= 2.37 GeV, and Strangeness 3= 5.31 GeV

initial estimate for the strangeness suppression. A first look at this same value for strangeness 3:2 in Fig. 6.4 (right) shows a similar trend, however, for strangeness 3 the photon energy is not high enough to reach a constant level due to the greater threshold discussed in Sec. 6.3.

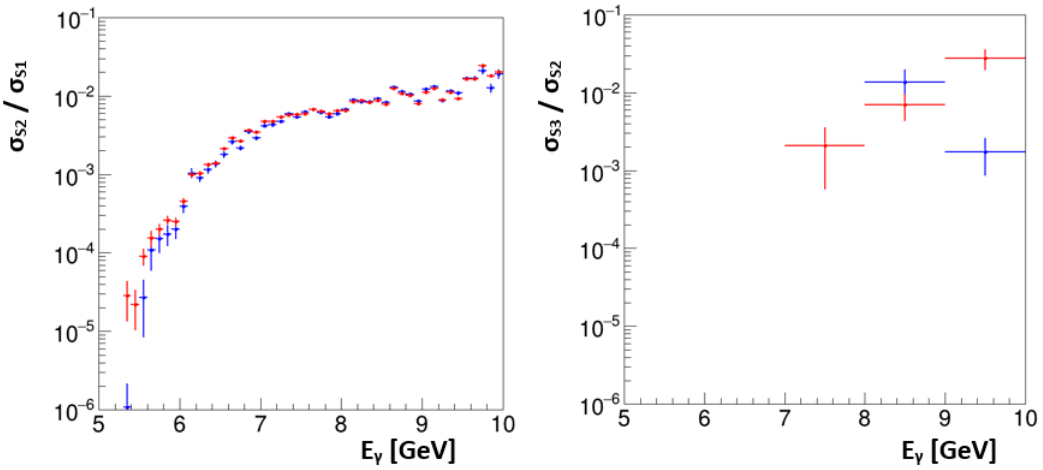

Fig. 6.4 Ratio of cross-sections for strangeness 2 to 1 (left) and strangeness 3 to 2 (right) with proton target data (blue) and deuteron target data (red). RGB Spring 2019 inbending and RGA Fall 2018 inbending data used.

6.4.2 Isospin dependence of meson coupling

Non-resonant production modes with a neutral meson exchange (isospin $I = 0$, scalar meson, or isospin $I = 1$ with charge $Q = 0$, neutral isovector meson) are expected to have similar couplings to a proton or a neutron. However, if the exchange particle is charged (isovector meson with charge $Q = -1$ in this case), this is not possible on a neutron if we do not consider Deck contributions. An example of this production channel is shown in Fig. 6.5. As discussed in Sec. 1.5.2, a ratio between deuteron and proton non-resonant kaon production close to 2, suggests a favouring of mesons with isospin $I = 0$; if the ratio is close to 1.5, this hints at mesons with isospin $I = 1$ as preferential.

The ratio $\frac{\sigma_d}{\sigma_p}$ for the non-resonance region of strangeness -1, shown in Fig. 6.6 (green), rapidly decreases from 2 to approximately 1.5 between photon energies 4–5 GeV; this is likely to come from resonant production contributions that overlap at these lower photon energies. At 5 GeV, this distribution plateaus at a ratio of approximately 1.5, which is still within the expected range of 1.5–2 set out in Sec. 6.3. Generally, this has a very smooth trend with no large deviations, which gives confidence in the validity of this approach. With the ratio sitting very close to 1.5, this suggests that there is a much stronger coupling of the isospin $I = 1$ mesons to the deuteron than the isospin $I = 0$.

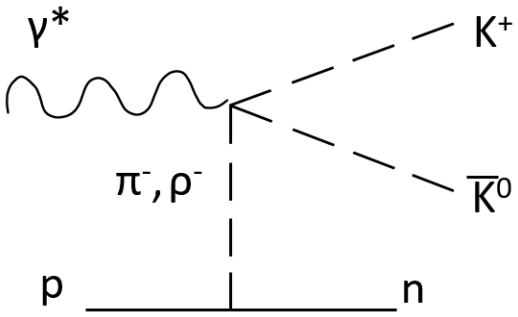

Fig. 6.5 Feynman diagram for kaon in-flight production with charged exchange meson interacting with proton target.

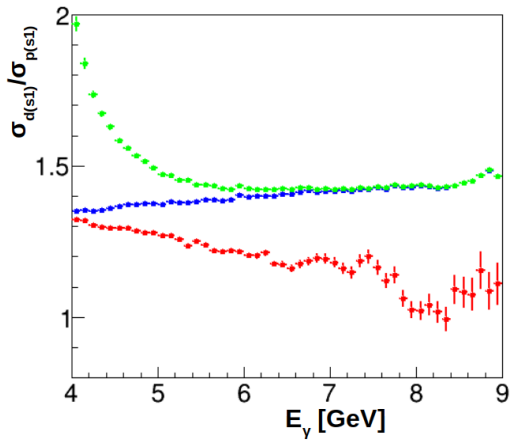

Fig. 6.6 Ratio of strangeness 1 cross-section on deuteron target to proton for total energy range (blue), resonance region (red), and non-resonance region (green). RGB Spring 2019 inbending and RGA Fall 2018 inbending data used.

An initial study for strangeness 2 has been performed, with results shown in Fig. 6.7. Although the ratios are approximately of the correct magnitude, the large statistical fluctuations and errors make it difficult to discern much from this result. Further studies with improved and higher statistics data will be performed, details of this are described in Sec. 8.2.

6.4.3 Strange exotic baryon

Figure. 6.6 (red) shows the ratio $\frac{\sigma_d}{\sigma_p}$ for the resonance region of strangeness 1, which has enhancements at $E_\gamma = 7$ and 7.5 GeV amongst the overall negative linear pattern seen, indicating an enhancement of strange baryon production on the deuteron target compared to proton. This could come from strange baryon production off of the neutron that cannot couple to a proton, such as a negatively charged hyperon. Alternatively, this increased production could be caused by the photon interacting with

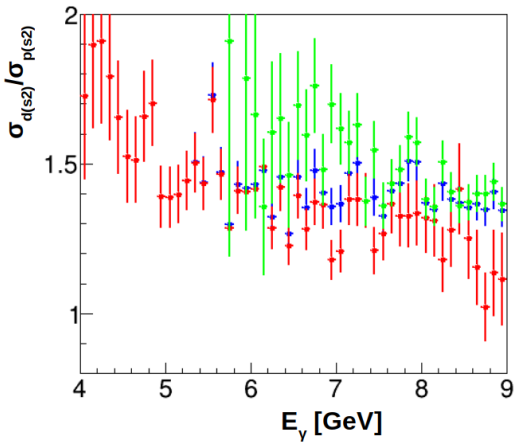

Fig. 6.7 Ratio of strangeness 2 cross-section on deuteron target to proton for total energy range (blue), resonance region (red), and non-resonance region (green). RGB Spring 2019 inbending and RGA Fall 2018 inbending data used.

the whole two-nucleon system (deuteron), producing a strange dibaryon that is also not possible on a proton due to baryon number conservation. A photon could also couple to the meson exchange currents in the deuteron, which is not possible on a proton. This is another possible cause of the enhanced K^+ production on deuteron compared to proton.

Similar to the non-resonance region in the isospin dependence of meson coupling, the large uncertainties for the resonance region in strangeness 2 in Fig. 6.7 (red) make it very difficult to extract meaningful conclusions. Most of the fluctuations are within the statistical errors, therefore, it is impossible to distinguish any enhancements in the strange production from the general downward linear trend.

Chapter 7

Analysis and Results III: Search For d_{sss}

In this chapter, the conditions applied to the experimental data for the d_{sss} search are shown, as well as the approaches used in the determination of this result, and first-ever constraint on its cross-section.

7.1 Particle and Event Selection Criteria

The d_{sss} has three decay modes. It can decay into two octet baryons, $\Xi^-\Sigma^-$, or it can decay via break-up to two decuplet baryons: $\Omega^-\Delta^-$ or $\Xi^{*-}\Sigma^{*-}$, which is shown in Fig. 7.1. All of these reaction channels have very high multiplicities, so even with the nearly hermetic CLAS12 detector, it would be incredibly unlikely to detect all of the final state particles. Choosing the d_{sss}^{--} was not purely for the lack of conventional background channels, the dibaryon can also be reconstructed by only detecting the scattered electron and three K^+ as discussed in Sec. 1.6.

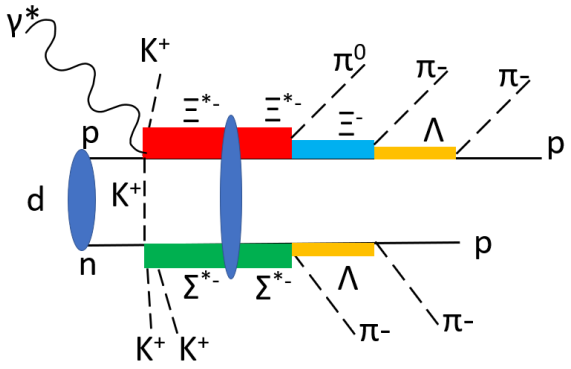

Fig. 7.1 Feynman diagram for the production of the d_{sss} dibaryon on deuteron, decaying to $\Xi^{*-}\Sigma^{*-}$.

As with the scaling of strangeness research, the kaons are required to be detected in the FD, due to the small increase in phasespace coverage and lower resolution shown in Sec. 6.1. To remove low-level background from the particle identification process, a cut on $|\chi^2_{PID}| < 3$ is placed upon all the kaons.

7.2 Determination of cross-section Upper Limit

Section 1.5 discusses what cross-sections are and shows some examples of how they can be used to extract other useful information. Cross-sections are calculated as a function of one or more kinematic variables, in this case, the kinematic variable is the missing mass of $ed \rightarrow e'K^+K^+K^+D$ where D represents the very strange dibaryon. The steps required in the determination of cross-section are as follows:

- determine the yield of the chosen reaction channel
- apply acceptance and efficiency corrections
- calculate the total flux of incoming particles
- correct for effective target density, derived from Eq. (1.3)
- account for the length of the target.

The first step is determining how many events of the given reaction channel occurred during the running of this experiment (yield). Particle and event selections are made as detailed in Sec. 7.1 to select the correct reaction channel. Before this can be used as the yield, background subtraction must be performed to reduce the contributions from other multiplicities and misidentifications. For this, the kaon background subtraction method discussed in Sec. 4.3 is applied. As this section details, this does remove a significant amount of the background but not 100%. This work is determining the upper limit of the d_{sss}'s cross-section, therefore, we want to constrain this value as close to the absolute cross-section as possible, while ensuring we do not underestimate through over-subtraction. For this reason, leaving a small amount of background in our yield will not affect the validity of the upper limit result.

Prior to the calculation of the production cross-section, acceptance and efficiency corrections need to be applied; this takes into account the angular coverage of the CLAS12 detector system as well as

the detector responses. This correction gives an estimate of how many events of this reaction channel were produced compared with how many were detected. Section 4.4 describes the general process of how the acceptance and efficiency corrections are determined for a given reaction channel. For this research, the channel in Fig. 7.2 was used to simulate the conventional triple strangeness channel, with Ξ^- and Σ^- being produced in the final state. This channel was chosen as a benchmark model, since it is the lightest known triple strangeness channel possible that can be produced, therefore, it has the largest acceptance coverage. The kinematic range of this model will cover any other channels with higher production thresholds, meaning they can be properly corrected for in terms of acceptance and efficiency. The general equation for this correction is specified in Eq. (4.6)

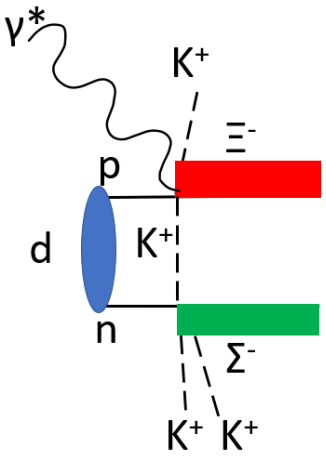

Fig. 7.2 Feynman diagram for the production of Ξ^- and Σ^- off a deuteron target.

As expected, for the pure MC data in Fig. 7.3, there are no events below the threshold level of 2.51 GeV for the nominal masses of Ξ^- and Σ^-. There is a fall-off just above the threshold due to the photon flux decreasing with energy faster than the available phasespace rises. After this reaction is simulated, the data is processed through GEMC, which puts these events through a virtual version of our detector system, implementing angular acceptance and realistic detector responses. The particle tracks are reconstructed in the same way as our real experimental data. The resulting missing mass plot in Fig. 7.4 shows missing mass values below the threshold for Ξ^- and Σ^-, which represents a combination of factors including the detector resolutions and lack of energy loss corrections, similar to what is observed in real data.

The ratio between the pure MC simulation and the simulation with detector responses is shown in Fig. 7.5, representing the acceptance and efficiency corrections factor. The smooth distribution tells us

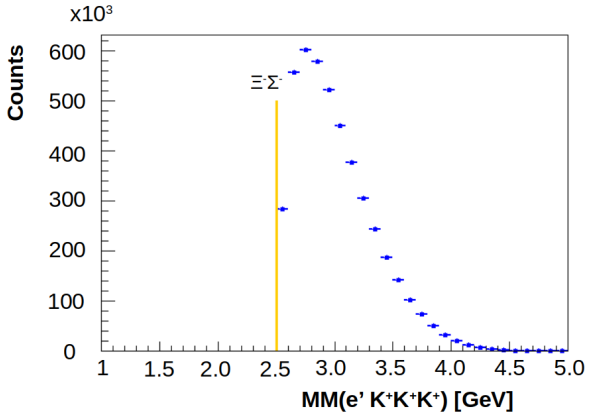

Fig. 7.3 Missing mass of $ed \rightarrow e'K^+K^+K^+D$ from pure MC simulation of $\Xi^-\Sigma^-$ channel with three kaon production threshold shown, $\Xi^-\Sigma^-$ (orange).

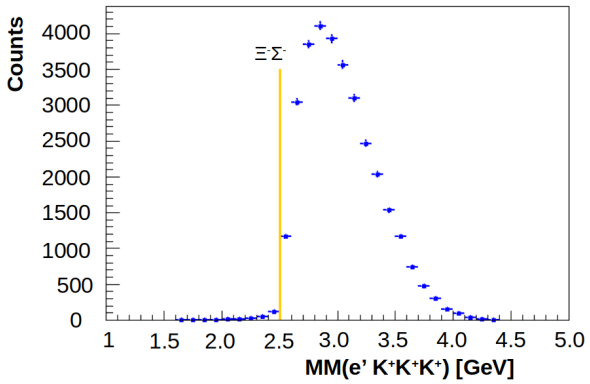

Fig. 7.4 Missing mass of $ed \rightarrow e'K^+K^+K^+D$ from MC simulation of $\Xi^-\Sigma^-$ channel after acceptance and detector responses are applied through GEMC with three kaon production threshold shown, $\Xi^-\Sigma^-$ (orange). RGB Spring 2019 Inbending setting applied in GEMC.

that the detector acceptance does not produce any artificial bumps in our missing mass distributions. From this figure, we can also estimate that for 100 events producing three K^+s, we only correctly reconstruct one event with our technique. This is a reasonable number given the high multiplicity channel. The values in this diagram are applied to the background-subtracted data.

Next, we need to calculate the total flux of incoming particles, in this case, how many electron events there were to produce the data analysed in this research. For this, we look at the accumulated charge in the Faraday Cup, then used this to calculate the total number of electrons that were impinged on the target using Eq. (3.7). During the course of the data taking used in this work, the total flux was $4.747\text{x}10^{17}$ electrons.

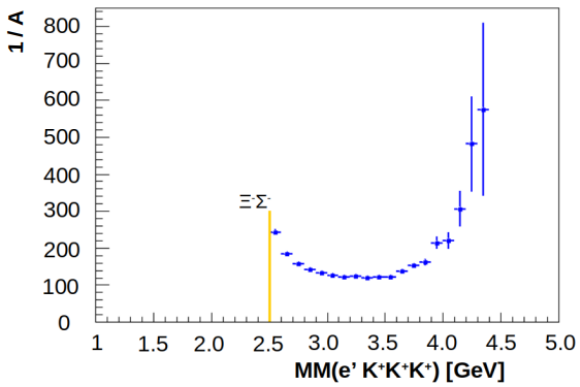

Fig. 7.5 Acceptance correction for strangeness 3 channel with three kaon production threshold shown, $\Xi^-\Sigma^-$ (orange). This distribution is the ratio between Fig. 7.3 and Fig. 7.4 producing $\frac{1}{A}$, where A is the product of the detector acceptances and efficiencies as defined in Eq. (4.6). RGB Spring 2019 Inbending setting applied in GEMC.

Another requirement is to take into account the target material and size. First, the effective target density must be determined, given by Eq. 1.3. This thesis research is focused on a deuteron target, which has an effective density of 4.874x10^{22} atoms cm^{-3}. For the target size, we only need to consider the length of the target in the direction of the electron beam, this is 5.0 cm for this experiment.

Since the accumulated statistics do not allow us to study the reaction in detail, even if we are confident in our selection of $e'3K^+$ events, we will concentrate on determining the upper limit for d_{sss} production, rather than attempting to extract the dibaryon itself. We define an upper limit using the assumption that all these events originate from the d_{sss} only, and impose a 3-σ upper bound to be confident that the real cross-section lies below with 95% probability.

7.3 Results

Before studies could be performed on the strangeness three production of d_{sss} with the deuteron target, benchmark studies were performed using proton and deuteron target data for strangeness one and two, and additionally on the proton target for strangeness three. One of the reasons these studies were performed was to discover possible background or other contributions that might arise from the virtual photon interacting with a single-nucleon in the liquid deuterium (deuteron) target instead of the whole two-nucleon system. While producing these results, the analysis process was developed and refined, the higher statistics of single and double strangeness and the cleanness of data from a single-nucleon target enabled this.

7.3.1 Benchmark Studies

Strangeness 1

A lot of hyperons were observed in the strangeness one channel $ep \rightarrow e'K^+Y$, as can be seen in Fig. 7.6. These include Λ, Σ, Σ_{1385}, Λ_{1520}, as well as signs of some of the higher mass Λs. The hyperon peaks sit on top of a smooth distribution, which comes from a physical background caused by kaon in-flight production which is shown in Figs. 1.4 and 1.5. It is also promising to see that there are very few events below the threshold for strangeness one production, which is equal to the mass of Λ, indicating that the selection of events and background subtraction was very effective.

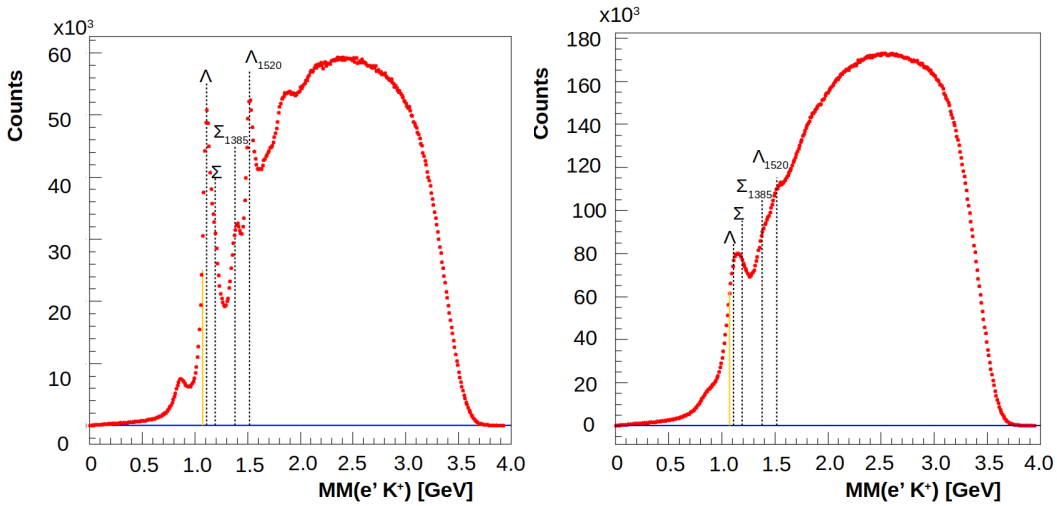

Fig. 7.6 Background subtracted missing mass for one K^+ production on a proton (left) and a deuteron target that is treated as a proton for a direct comparison (right). Well-known hyperons are highlighted at peak positions (RGA Fall 2018 inbending (proton) and RGB Spring 2019 inbending (deuteron) data used).

Comparing the strangeness one production result for the proton target (RGA) to that of the deuteron target (RGB), there are a few things to note. Some hyperons that are visible in the RGA missing mass plot are not in the RGB one, which is caused by several factors. The fermi motion inside the deuteron invalidates the assumption that the target is stationary, making the peaks in the RGB data broader than those in RGA. Another factor to consider is that interactions on the proton and neutron produce different charge states of the same hyperon. These different charge states often have similar masses such as the Σ^0 and Σ^- (1193 MeV/c and 1197 MeV/c respectively), leading to overlapping signals that cause broader peaks in the missing mass distributions.

With a deuteron target, the photon can interact with the whole two-nucleon system also, which was not available with a proton target, allowing for single strangeness dibaryons. Lastly, the calibration for RGA is more developed than that of RGB's, which can lead to further broadening of the peaks.

Strangeness 2

CLAS12's first evidence for Ξ^- was produced in this research and is clearly seen in Fig. 7.7 (left). Additionally, the $\frac{3}{2}^+$ state Ξ^-_{1530} was observed in this study for the first time at CLAS. These results show great promise for studying double-strange systems with electroproduction. There is a sharp fall-off below the threshold of strangeness two production, the Ξ ground state, further validating the event selection process and background subtraction performed in this research.

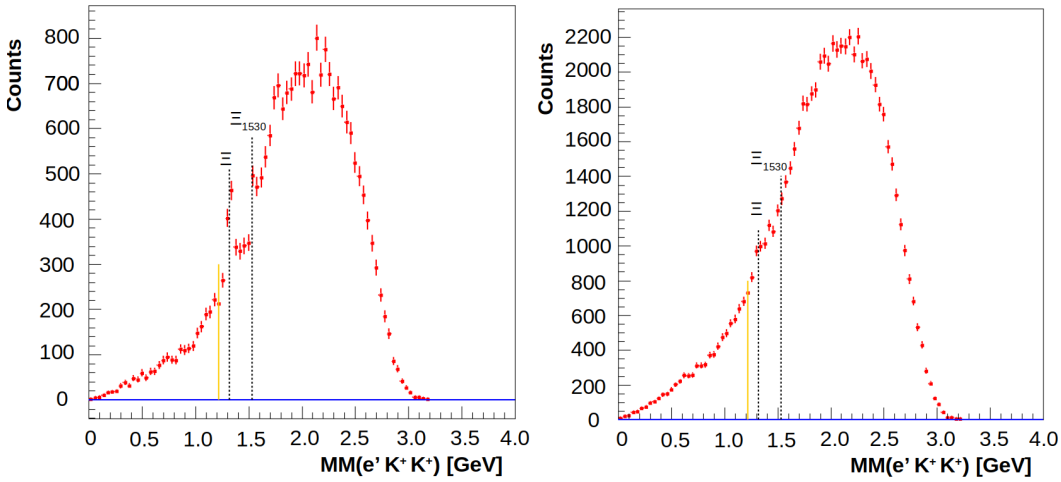

Fig. 7.7 Background subtracted missing mass for two K^+ production on a proton (left) and a deuteron target that is treated as a proton for a direct comparison (right). Well-known hyperons are highlighted at peak positions. RGA Fall 2018 inbending (proton) and RGB Spring 2019 inbending (deuteron) data used.

The contrast between the RGA and RGB missing mass distribution for two kaon production is clear, and the previously seen Ξ states are much less prominent. For strangeness two production, there are no conventional channels produced on the neutron. Therefore, if we assume an equal coupling of the photon to the proton and neutron, we expect the cross-section of these conventional resonances on the deuteron to be half that on the proton.

Strangeness 3

As we have detection of three K^+s in the final state, a triple-strange and double-negative system must have been produced for this to be a strong interaction. For production on a proton, the lightest system this could be is $\Omega^-\pi^-$ or Ξ^-K^-. Both have very similar production thresholds, within 3–4 MeV of each other. Reference [67] shows that we do not expect a bound state to be produced from the $\Omega\pi$, however, a cusp behaviour is possible because of coupled channel effects between Ξ^-K^- and $\Omega^-\pi^-$. Figure 7.8 (left) shows this behaviour but insufficient statistics prevent us from making a clear claim. Greater statistics from subsequent measurements could enable us to perform detailed studies of such a system. For these studies on a proton target (RGA), adding events with the scattered electron in the FT might provide high enough statistics for this. There is similar behaviour on the deuteron, however, due to the fact that the RGB calibration is still ongoing, we see large background contributions leaking through in Fig. 7.8 (right).

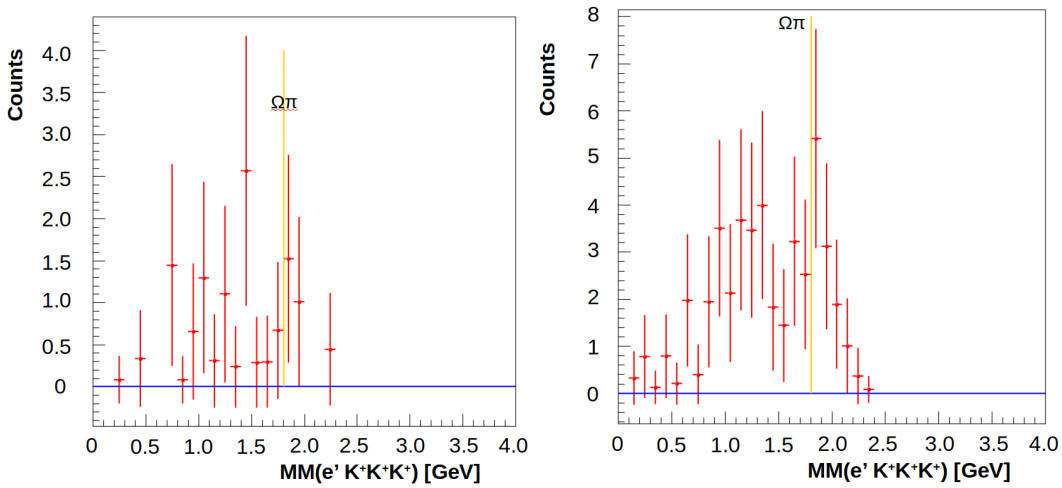

Fig. 7.8 Background subtracted missing mass for three K^+ production on a proton (left) and a deuteron target that is treated as a proton for a direct comparison (right). The threshold for strangeness 3 production, $\Omega\pi$, is highlighted (dashed line). RGA Fall 2018 inbending (proton) and RGB Spring 2019 inbending (deuteron) data used.

7.3.2 Upper Limit of cross-section for d_{sss}

Due to the lack of concrete evidence for the d_{sss} in this research, it was not viable to calculate an absolute cross-section, however, an upper limit was produced. This was done by taking the background subtracted missing mass for three K^+ production on a deuteron target, similar to Fig. 7.8 but using

the mass of deuteron for the target in the missing mass instead. Next, the acceptance and efficiency corrections in Fig. 7.5 were applied. This gives the differential cross-section, shown in Fig. 7.9 as the blue filled region, which includes three σ. The upper limit for the differential cross-section of $ed \rightarrow e' K^+ K^+ K^+ d_{sss}$ was determined to be $\frac{d\sigma_{d_{sss}}}{dMM} = 76$ fb/GeV with a 95 % confidence level. One reason why this cross-section upper limit is so small has been discussed in Sec. 6, with the strangeness suppression factor of $\frac{1}{100}$ per level of strangeness.

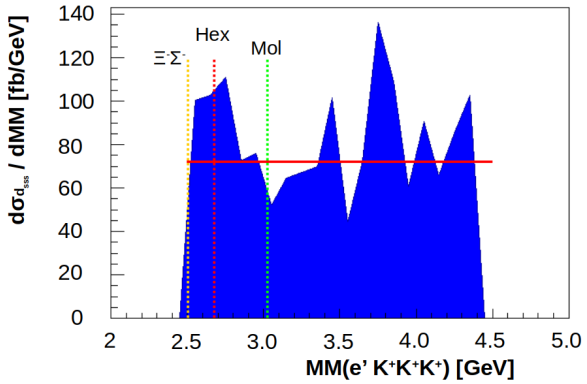

Fig. 7.9 Upper limit on cross-section for d_{sss} with fit (solid red), production threshold (dashed orange), mass for pure genuine hexaquark (dashed red), and maximum mass for pure molecular dibaryon state (dashed green) shown. RGB Spring 2019 Inbending data used.

It is obvious that we are only scratching the physics surface of triple-strange systems with the accumulated statistics. The results presented in this thesis are very promising, showing that with future runs, especially with the potential high-luminosity CLAS24, we will be able to study these states in detail. A possible cusp behaviour from $\Omega\pi$ might contaminate the threshold region, but comparisons with measurements made on a proton target could provide sufficient confidence to study the threshold region. Theoretical calculations for the mass of the d_{sss} come to approximately 2.7 GeV for a pure genuine hexaquark and 2.9 GeV for a pure molecular dibaryon, so understanding of this threshold region is critical for future studies.

This thesis work only considers the detection of the scattered electron and three K^+s, with many subsequent decay vertices after the production of the d_{sss}, there are lots of possible avenues for further exploration. One decay mode of the d_{sss} is to $\Omega^- \Delta^-$, and if we could reconstruct these two baryons in a single event, it would provide very strong evidence for the d_{sss}. This is because we would have a system with triple-strangeness, double-negative, and two baryons, all of which are required from the decay of d_{sss}^{--}. However, this would require the detection of at least six final state particles including the scattered electron, which is a requirement in the trigger for data collection.

Chapter 8

Conclusion and Outlook

In this chapter, I will give an overview of the most recent results regarding these three projects, discuss future plans, and how they can be improved further.

8.1 Exotic Mesons

With the current stage of this analysis, where the angular distribution moments are determined but no partial wave analysis has been undertaken, no outright statements can be made about the mesons that contribute to the production of the K^+K^- pair. That being said, the distributions that are shown behave as expected with smooth trends and clear structures appearing at some well-known mesons that match across multiple moment distributions. This gives confidence in the reliability of this work. Fitting these moment distributions with PWA is rather straightforward from a theoretical perspective. A suitable framework has already been developed and tested on the $\eta\pi^0$ case [66]. It has been agreed with [68] that the data showcased in this thesis can be processed further through PWA analysis after the *pass*2 calibration update. Partial wave analysis should be able to verify if these angular distribution moments are reasonable and clarify what meson contributions are seen in the production of the K^+K^- pair.

The analysis presented in Chapter 5 was performed on only one run period of data, RGA fall 2018 outbending. There are two more available that can be used to increase the statistics by approximately a factor of three. The other two run periods have inbending torus polarity in contrast with the currently used outbending data, which describes the direction a negatively charged particle would go relative to the beamline. In the case of $X \to K^+K^-$, we expect little difference in acceptance since the kaons

are mirrored in this decay, however, an influence on the available electrons is expected. Performing a combined analysis of the inbending and outbending data can significantly reduce the statistical uncertainty of the reaction and allows us to study systematic effects. Before a combined analysis can be performed, comparison studies must be undertaken to ensure they match reasonably well. To do this, simulations would be performed for both magnet polarities, as they might have different acceptances for the electron. These would need to be weighted appropriately based on the flux of each of the data sets.

A new phase of improvements is being made to the reconstruction performed within the CLAS collaboration, called *pass*2. Improvements include an energy loss correction, better reconstruction (primarily in the CD), and superior calibrations. In these studies, the line shapes, especially in regions of interfering resonances, are crucial to pinpoint the underlying states. The substantial improvement in accuracy that will come with the *pass*2 calibration, as well as the statistics increase, will make this analysis more robust and decrease systematic effects.

A variety of different cuts and constraints were performed on this data that are summarised in Tab. 5.1, the effect of these were compared between experimental and simulated data. However, detailed systematic studies of these constraints need to be performed to make sure that they are not biasing the final results. Such studies are dependent on calibration and reconstruction, therefore, this part of the analysis was postponed until the completion of the *pass*2 data processing.

Once this analysis has been run over all the available data with the *pass*2 improvements, the partial waves will be extracted from the moments. These in turn will be used to determine the different mesons contributing to the production of the K^+K^- pair. Even at this stage, without partial wave analysis and an incomplete data set, there is a lot of promise in the moments produced. It is expected that once these improvements have been completed, we should have a high-impact result. The expectation is that the results of this work will be used to evaluate conventional meson background in the region of hybrid mesons, which is critical for the extraction of the hybrid-nonhybrid interference effects. Additionally, by observing the quantum numbers of the mesons contributing to the K^+K^- production, a search for potential glueballs will be performed. Particular focus will be placed on the region of the first tensor glueball, with M $\approx$ 2000 MeV.

8.2 Scaling Behaviour Of Strangeness

This research provides the first-ever scaling behaviour of strangeness and already has a wealth of interesting results.

An initial estimate for the strangeness suppression factor has been determined to be $\frac{1}{100}$. This illustrates the experimental difficulties that come with studying the excited spectrum of hyperons. To further confirm this value, the suppression factor should be determined between strangeness two and three. Since the threshold for strangeness three production is high, at approximately 7.5 GeV, a more energetic beam would be required. There are discussions for a possible upgrade to the CEBAF at JLab that could provide electron beam energies up to 24 GeV, assuming a similar trend to the strangeness 2:1 factor, this should be more than enough to attain a secondary suppression factor.

The isospin dependence of meson exchange for in-flight production covers a broad area with a lot of interest from theoreticians. Pomeron exchange (scalar/isoscalar) [69] is expected to be the main production mode for most mesons. Previous experimental results tend to agree with this statement, however, other exchange meson contributions need to be considered in future theoretical studies. The results from this thesis work provide the ability to study the meson exchange isospin dependence for a K^+K^- system. In this work, the ratio determined is close to 1.5. As discussed in Sec. 6.4.2, this indicates a dominance of isovector meson exchange as opposed to isoscalar.

Clear enhancements of strangeness one production on the deuteron target can be seen compared with the proton target in Fig. 6.6 (red). This could potentially lead to the discovery of some new hyperons and possibly even exotic ones given that these appear to be proto-phobic. To explore these possible new hyperons, the next step would be to look at the reconstruction of hyperon Y on the deuteron target for the photon energies discussed in Sec. 6.4.3. The same energy regimes on the proton could be looked at and compared to this, potentially subtracting this from the deuteron result to see if any enhancements are visible.

8.3 Very Strange Dibaryon

This work shows the first study of a very exotic triple-strange, double-negative system on deuteron and proton. Theory predicts no conventional states in the single-baryon case. There is a trace of a cusp effect at the $\Omega\pi$ production threshold in the results shown in this thesis. This study also

highlighted, for the first time, that a triple-strange system is achievable with electroproduction, even with the limited statistics available to us. Although it is interesting to see the cusp behaviour, its appearance in a conventional, resonance-free channel makes the analysis of the possible dibaryon channel much harder. Fortunately, the momentum resolution improvements that will come with *pass*2 and the enhancement of statistics might resolve this issue.

The first-ever constraint on the d_{sss} has been produced, and future studies should be able to better determine the upper limit of the absolute cross-section. It is expected that with the energy-loss correction and improved reconstruction from *pass*2, this analysis should provide more robust results. Additionally, more data should be processed with *pass*2, making the result more statistically significant.

If the d_{sss} was discovered and found to be a genuine hexaquark, it would provide a gateway for further many-body studies, especially within the d^*_{2380}'s antidecuplet. With many exotics being discovered every year, it can be difficult for studies such as these to stand out significantly. However, this work looks at not only potential genuine hexaquarks, which informs us on the many body problem in QCD, but also the first ever triple-strange, double-negative, and double-baryon system. This and future studies on this system will be highly influential, providing new knowledge and peaking into a new and very broad area of physics with lots of potential exploration.

Bibliography

[1] M. Battaglieri et al., *Meson Spectroscopy with low Q^2 electron scattering in CLAS12*, tech. rep. (2011).

[2] M. J. Amaryan et al., "Photoproduction of the Very Strangest Baryons on a Proton Target in CLAS12", 1–50 (2012).

[3] J. Thomson, " XXIV. On the structure of the atom: an investigation of the stability and periods of oscillation of a number of corpuscles arranged at equal intervals around the circumference of a circle; with application of the results to the theory of atomic structure", The London, Edinburgh, and Dublin Philosophical Magazine and Journal of Science **7**, 237–265 (1904).

[4] J. J. Thomson, " XL. Cathode Rays ", The London, Edinburgh, and Dublin Philosophical Magazine and Journal of Science **44**, 293–316 (1897).

[5] H. Geiger and E. Marsden, "On a diffuse reflection of the α-particles", Proceedings of the Royal Society of London. Series A, Containing Papers of a Mathematical and Physical Character **82**, 495–500 (1909).

[6] E. Rutherford, " LXXIX. The scattering of α and β particles by matter and the structure of the atom ", The London, Edinburgh, and Dublin Philosophical Magazine and Journal of Science **21**, 669–688 (1911).

[7] S. Braibant, G. Giacomelli, and M. Spurio, *Particles and Fundamental Interactions* (Springer Netherlands, Dordrecht, 2012).

[8] R. Mann, *An introduction to particle physics and the standard model* (CRC Press, Jan. 2009), pp. 15–20, https://www-taylorfrancis-com.libproxy.york.ac.uk/books/oa-mono/10.1201/9781420083002/introduction-particle-physics-standard-model-robert-mann.

[9] D. H. Perkins, *Introduction to High Energy Physics, 4th Edition Introduction to High Energy Physics* ().

[10] R. August, "15. Quark Model", **090001**, 1–26 (2014).

[11] A. J. Buchmann, "Structure of strange baryons", in *Proceedings of the ix international conference on hypernuclear and strange particle physics* (Springer Berlin Heidelberg, June 2008), pp. 329–333.

[12] A. Douglas and J. Keller, "© 1947 Nature Publishing Group", NatureGroup **160**, 29–31 (1947).

[13] S. Gongyo et al., "Most Strange Dibaryon from Lattice QCD", Physical Review Letters **120**, 10.1103/PhysRevLett.120.212001 (2018), https://link.aps.org/doi/10.1103/PhysRevLett.120.212001.

[14] A. Chodos et al., *New extended model of hadrons*, tech. rep. (1974), https://journals.aps.org/prd/pdf/10.1103/PhysRevD.9.3471.

[15] The E852 Collaboration, "Evidence for Exotic Meson Production in the Reaction $\pi^- p \to \eta \pi^- p$ at 18 GeV/c", 1–14 (1997), http://arxiv.org/abs/hep-ex/9705011.

[16] G. S. Adams et al., "Confirmation of the 1^{-+} Meson Exotics in the $\eta\pi^0$ System", Physics Letters. B **1**, 1–6 (2006), https://arxiv.org/pdf/hep-ex/0612062.pdf.

[17] E852 Collaboration and S. U. C. e. Al, "Evidence for Exotic $J^{PC} = 1^{-+}$ Meson Production in the Reaction $\pi^- p \to \eta\pi^- p$ at 18 GeV/c", 10.1103/PhysRevD.60.092001 (1999), http://arxiv.org/abs/hep-ex/9902003.

[18] R. D. Tripp, "Spin and Parity Determination of Elementary Particles", Annual Review of Nuclear Science **15**, 325–380 (1965), https://www.annualreviews.org/doi/10.1146/annurev.ns.15.120165.001545.

[19] P. Z. e. Al, *(Particle Data Group), Prog. Theor. Exp. Phys. 2020* (2020), https://pdg.lbl.gov/2020/.

[20] P. Adlarson et al., "Abashian-booth-crowe effect in basic double-pionic fusion: A new resonance?", Physical Review Letters **106**, 10.1103/PhysRevLett.106.242302 (2011), http://arxiv.org/abs/1104.0123.

[21] M. Bashkanov et al., "Double-pionic fusion of nuclear systems and the "ABC" effect: Approaching a puzzle by exclusive and kinematically complete measurements", Physical Review Letters **102**, 1–5 (2009).

[22] P. Adlarson et al., "Evidence for a new resonance from polarized neutron-proton scattering", Physical Review Letters **112**, 10.1103/PhysRevLett.112.202301 (2014).

[23] R. Molina, N. Ikeno, and E. Oset, "Sequential single pion production explaining the dibaryon $d^*(2380)$ peak", (2021), http://arxiv.org/abs/2102.05575.

[24] M. Bashkanov et al., "Deuteron photodisintegration by polarized photons in the region of the $d^*(2380)$", Physics Letters, Section B: Nuclear, Elementary Particle and High-Energy Physics **789**, 7–12 (2019), http://arxiv.org/abs/1809.09398.

[25] M. Bashkanov, D. P. Watts, and A. Pastore, "Electromagnetic properties of the $d^*(2380)$ hexaquark", 10.1103/PhysRevC.100.012201 (2019), http://arxiv.org/abs/1905.00713%20http://dx.doi.org/10.1103/PhysRevC.100.012201.

[26] M. Bashkanov et al., "Decay properties of the $d^*(2380)$ hexaquark multiplet", (2020), http://arxiv.org/abs/2012.11449.

[27] Q. F. Lü et al., "Six-quark structure of d (2380) in a chiral constituent quark model", Physical Review D **96**, 10.1103/PhysRevD.96.014036 (2017).

[28] Y. Dong, P. Shen, and Z. Zhang, "Form factors of the d* (2380) resonance", Physical Review D **97**, 10.1103/PhysRevD.97.114002 (2018).

[29] A. Abele et al., "Evidence for a ph-P-wave in pp-annihilations at rest into p p h Crystal Barrel Collaboration ¨ ¨", Physics Letters B **446**, 349–355 (1999), https://www.sciencedirect.com/science/article/abs/pii/S0370269398015445.

[30] T. Barnes, "Exotic mesons, theory and experiment", Acta Physica Polonica B **31**, 2545–2556 (2000).

[31] G. S. Adams et al., "Observation of a new $J^{PC} = 1^{-+}$ exotic state in the reaction $\pi^- p \to \pi^+\pi^-\pi^- p$ at 18 GeV/c", Physical Review Letters **81**, 5760–5763 (1998).

[32] V. Dorofeev and V. E. S. collaboration, "New results from VES", **hep-ex** (1999), http://arxiv.org/abs/hep-ex/9905002v1.

[33] C. Adolph et al., "Resonance production and $\pi\pi$ S-wave in $\pi^- p \to \pi^-\pi^-\pi^+ p_{recoil}$ at 190 GeV/c", Physical Review D **95**, 1–59 (2017).

[34] A. V. Sarantsev et al., "Scalar isoscalar mesons and the scalar glueball from radiative J/ψ decays", Physics Letters, Section B: Nuclear, Elementary Particle and High-Energy Physics **816**, 10.1016/j.physletb.2021.136227 (2021).

[35] KLF Collaboration et al., "Strange Hadron Spectroscopy with Secondary KL Beam in Hall D", (2020), http://arxiv.org/abs/2008.08215.

[36] Y. Qiang et al., "Properties of the $\Lambda(1520)$ resonance from high-precision electroproduction data", Physics Letters, Section B: Nuclear, Elementary Particle and High-Energy Physics **694**, 123–128 (2010).

[37] The GlueX Collaboration et al., "An initial study of mesons and baryons containing strange quarks with GlueX", 1–22 (2013), http://arxiv.org/abs/1305.1523.

[38] B. Aubert et al., "Measurement of the spin of the $\Xi(1530)$ resonance", Physical Review D **78**, 034008 (2008), https://link.aps.org/doi/10.1103/PhysRevD.78.034008.

[39] S. F. Biagi et al., "Ξ^{*-} Resonances in Ξ^- Be interactions II. Properties of $\Xi(1820)$ and $\Xi(1960)$ in the $\Lambda\bar{K}^0$ and $\Sigma^0\bar{K}^0$ channels", Zeitschrift für Physik C Particles and Fields **34**, 175 (1987).

[40] V. Crede, "The excited baryon spectrum: What have we learned?", AIP Conference Proceedings **2249**, 10.1063/5.0009281 (2020).

[41] C. W. Leemann, D. R. Douglas, and G. A. Krafft, "The Continous Electron Beam Accelerator Facility: CEBAF at the Jefferson Laboratory", Annual Review of Nuclear and Particle Science **51**, 413–450 (2001), https://www.annualreviews.org/doi/10.1146/annurev.nucl.51.101701.132327.

[42] V. D. Burkert et al., "The CLAS12 Spectrometer at Jefferson Laboratory", Nuclear Instruments and Methods in Physics Research, Section A: Accelerators, Spectrometers, Detectors and Associated Equipment **959**, 10.1016/j.nima.2020.163419 (2020).

[43] A. Acker et al., "The CLAS12 Forward Tagger", Nuclear Instruments and Methods in Physics Research, Section A: Accelerators, Spectrometers, Detectors and Associated Equipment **959**, 163475 (2020), https://doi.org/10.1016/j.nima.2020.163475.

[44] Y. Giomataris et al., "MICROMEGAS: A high-granularity position-sensitive gaseous detector for high particle-flux environments", Nuclear Instruments and Methods in Physics Research, Section A: Accelerators, Spectrometers, Detectors and Associated Equipment **376**, 29–35 (1996).

[45] A. Acker et al., "The CLAS12 Micromegas Vertex Tracker", Nuclear Instruments and Methods in Physics Research, Section A: Accelerators, Spectrometers, Detectors and Associated Equipment **957**, 163423 (2020), https://doi.org/10.1016/j.nima.2020.163423.

[46] M. D. Mestayer et al., "The CLAS12 drift chamber system", Nuclear Instruments and Methods in Physics Research, Section A: Accelerators, Spectrometers, Detectors and Associated Equipment **959**, 10.1016/j.nima.2020.163518 (2020).

[47] M. Contalbrigo et al., "The CLAS12 Ring Imaging Cherenkov detector", Nuclear Instruments and Methods in Physics Research, Section A: Accelerators, Spectrometers, Detectors and Associated Equipment **964**, 163791 (2020), https://doi.org/10.1016/j.nima.2020.163791.

[48] D. S. Carman et al., "The CLAS12 Forward Time-of-Flight system", Nuclear Instruments and Methods in Physics Research, Section A: Accelerators, Spectrometers, Detectors and Associated Equipment **960**, 10.1016/j.nima.2020.163629 (2020).

[49] G. Asryan et al., "The CLAS12 forward electromagnetic calorimeter", Nuclear Instruments and Methods in Physics Research, Section A: Accelerators, Spectrometers, Detectors and Associated Equipment **959**, 10.1016/j.nima.2020.163425 (2020).

[50] P. Monaghan, "Wire Chambers: A Brief How-to", in Hampton university graduate school (2012), https://www.jlab.org/hugs/archive/Schedule2012/Friday15/monaghan-hugs-wire-chambers-v1.pdf.

[51] M. Ungaro et al., "The CLAS12 Low Threshold Cherenkov detector", Nuclear Instruments and Methods in Physics Research Section A: Accelerators, Spectrometers, Detectors and Associated Equipment **957**, 163420 (2020), https://linkinghub.elsevier.com/retrieve/pii/S0168900220300255.

[52] M. A. Antonioli et al., "The CLAS12 Silicon Vertex Tracker", Nuclear Instruments and Methods in Physics Research, Section A: Accelerators, Spectrometers, Detectors and Associated Equipment **962**, 163701 (2020), https://doi.org/10.1016/j.nima.2020.163701.

[53] D. S. Carman et al., "The CLAS12 Central Time-of-Flight system", Nuclear Instruments and Methods in Physics Research, Section A: Accelerators, Spectrometers, Detectors and Associated Equipment **960**, 163626 (2020), https://doi.org/10.1016/j.nima.2020.163626.

[54] P. Chatagnon et al., "The CLAS12 Central Neutron Detector", Nuclear Instruments and Methods in Physics Research, Section A: Accelerators, Spectrometers, Detectors and Associated Equipment **959**, 163441 (2020), https://doi.org/10.1016/j.nima.2020.163441.

[55] K. S. Krane., *Introductory Nuclear Physics* (Hoboken NJ : Wiley, 1987), pp. 201–202.

[56] R. Fair et al., "The CLAS12 superconducting magnets", Nuclear Instruments and Methods in Physics Research, Section A: Accelerators, Spectrometers, Detectors and Associated Equipment **962**, 10.1016/j.nima.2020.163578 (2020).

[57] S. Diehl, "CLAS12 MesonEx trigger studies", in Clas collaboration meeting - jlab (2017), https://indico.jlab.org/event/222/.

[58] D. Glazier, *CLAS12ElSpectro*, https://github.com/dglazier/clas12-elSpectro.

[59] Maurizio Ungaro, *GEMC*, https://gemc.jlab.org/gemc/html/index.html.

[60] B. Povh et al., *Particles and Nuclei*, edited by S. HAssani et al. (Springer, 2015).

[61] R. Barlow, "Extended maximum likelihood", Nuclear Instruments and Methods in Physics Research Section A: Accelerators, Spectrometers, Detectors and Associated Equipment **297**, 496–506 (1990), https://linkinghub.elsevier.com/retrieve/pii/0168900290913348.

[62] S. Weinzierl, "Introduction to Monte Carlo methods", (2000), http://arxiv.org/abs/hep-ph/0006269.

[63] L. Bibrzycki, L. Lesniak, and A. P. Szczepaniak, "$K\bar{K}$ photoproduction and S-P wave interference", 10.1140/epjc/s2004-01724-6 (2003), http://arxiv.org/abs/hep-ph/0308267.

[64] S. Gardner, Private Discussion.

[65] D. Glazier, "Analysis Tools for CLAS12-Application of RooFit", in Clas collaboration meeting (2019), https://indico.jlab.org/event/343/contributions/5450/attachments/4585/5691/GlazierBruFit.pdf.

[66] V. Mathieu et al., "Moments of angular distribution and beam asymmetries in $\eta\pi^0$ photoproduction at GlueX", 10.1103/PhysRevD.100.054017 (2019), http://arxiv.org/abs/1906.04841%20http://dx.doi.org/10.1103/PhysRevD.100.054017.

[67] M. F. Lutz and E. E. Kolomeitsev, "Baryon resonances from chiral coupled-channel dynamics", Nuclear Physics A **755**, 29–39 (2005).

[68] V. Mathieu, Private Discussion.

[69] A. Bolz et al., "Photoproduction of $\pi^+\pi$ pairs in a model with tensor-pomeron and vector-odderon exchange", Journal of High Energy Physics **2015**, 1–48 (2015).

Appendix A

$$H^0(00) = H^1(00) + 2[|P_1^{(+)}|^2 + |D_1^{(+)}|^2 + |D_2^{(+)}|^2] \tag{A.1a}$$

$$H^1(00) = 2[|S_0^{(+)}|^2 + |P_0^{(+)}|^2 + |D_0^{(+)}|^2] \tag{A.1b}$$

$$H^0(10) = H^1(10) + \frac{4}{\sqrt{5}} Re(P_1^{(+)} D_1^{(+)*}) \tag{A.1c}$$

$$H^1(10) = \frac{8}{\sqrt{15}} Re(P_0^{(+)} D_0^{(+)*}) + \frac{4}{\sqrt{3}} Re(S_0^{(+)} P^{(+)*}) \tag{A.1d}$$

$$H^0(11) = H^1(11) + 2\sqrt{\frac{2}{5}} Re(P_1^{(+)} D_2^{(+)*}) \tag{A.1e}$$

$$H^1(11) = \frac{2}{\sqrt{5}} Re(P_0^{(+)} D_1^{(+)*}) - \frac{2}{\sqrt{15}} Re(P_1^{(+)} D_0^{(+)*}) + \frac{2}{\sqrt{3}} Re(S_0^{(+)} P_1^{(+)*}) \tag{A.1f}$$

$$H^0(20) = H^1(20) - \frac{2}{5}|P_1^{(+)}|^2 + \frac{2}{7}|D_1^{(+)}|^2 - \frac{4}{7}|D_2^{(+)}|^2 \tag{A.1g}$$

$$H^1(20) = \frac{4}{5}|P_0^{(+)}|^2 + \frac{4}{7}|D_0^{(+)}|^2 + \frac{4}{\sqrt{5}} Re(S_0^{(+)} D_0^{(+)*}) \tag{A.1h}$$

$$H^0(21) = H^1(21) + \frac{2}{7}\sqrt{6} Re({D_1}^{(+)} D_2^{(+)*}) \tag{A.1i}$$

$$H^1(21) = \frac{2}{\sqrt{5}} Re(S_0^{(+)} D_1^{(+)*}) + \frac{2\sqrt{3}}{5} Re(P_0^{(+)} P_1^{(+)*}) + \frac{2}{7} Re(D_0^{(+)} D_1^{(+)*}) \tag{A.1j}$$

$$H^0(22) = \frac{2}{\sqrt{5}} Re(S_0^{(+)} D_2^{(+)*}) - \frac{4}{7} Re(D_0^{(+)} D_2^{(+)*}) \tag{A.1k}$$

$$H^1(22) = H^0(22) + \frac{\sqrt{6}}{7}|D_1^{(+)}|^2 + \frac{\sqrt{6}}{5}|P_1^{(+)}|^2 \tag{A.1l}$$

and for $L = 3,4$

$$H^0(30) = H^1(30) - \frac{12}{7\sqrt{5}} Re(P_1^{(+)} D_1^{(+)*}) \tag{A.2a}$$

$$H^1(30) = \frac{12}{7}\sqrt{\frac{3}{5}}Re(P_0^{(+)}D_0^{(+)*}) \tag{A.2b}$$

$$H_0(31) = H^1(31) = -\frac{2}{7}\sqrt{\frac{3}{5}}Re(P_1^{(+)}D_2^{(+)*}) \tag{A.2c}$$

$$H^1(31) = \frac{4}{7}\sqrt{\frac{6}{5}}Re(P_0^{(+)}D_1^{(+)*}) + \frac{6}{7}\frac{\sqrt{2}}{5}Re(P_1^{(+)}D_0^{(+)*}) \tag{A.2d}$$

$$H^0(32) = H^1(32) - \frac{2}{7}\sqrt{6}Re(P_1^{(+)}D_1^{(+)*}) \tag{A.2e}$$

$$H^1(32) = \frac{2}{7}\sqrt{3}[Re(P_0^{(+)}D_2^{(+)*}) + \sqrt{2}Re(P_1^{(+)}D_1^{(+)*})] \tag{A.2f}$$

$$H^0(33) = 0 \tag{A.2g}$$

$$H^1(33) = \frac{6}{7}Re(P_1^{(+)}D_2^{(+)*}) \tag{A.2h}$$

$$H^0(40) = H^1(40) - \frac{2}{21}[4|D_1^{(+)}|^2 - |D_2^{(+)}|^2] \tag{A.2i}$$

$$H^1(40) = \frac{4}{7}|D_0^{(+)}|^2 \tag{A.2j}$$

$$H^0(41) = H^1(41) - \frac{2}{21}\sqrt{5}Re(D_1^{(+)}D_2^{(+)*}) \tag{A.2k}$$

$$H^1(41) = \frac{2}{7}\sqrt{\frac{10}{3}}Re(D_0^{(+)}D_1^{(+)*}) \tag{A.2l}$$

$$H^0(42) = -\frac{2}{7}\sqrt{\frac{5}{3}}Re(D_0^{(+)}D_2^{(+)*}) \tag{A.2m}$$

$$H^1(42) = H^0(42) + \frac{2\sqrt{10}}{21}|D_1^{(+)}|^2 \tag{A.2n}$$

$$H^0(43) = H^{(0)}(44) = 0 \tag{A.2o}$$

$$H^1(43) = \frac{2}{3}\sqrt{\frac{5}{7}}Re(D_1^{(+)}D_2^{(+)*}) \tag{A.2p}$$

$$H^1(44) = \frac{1}{3}\sqrt{\frac{10}{7}}|D_2^{(+)}|^2 \tag{A.2q}$$

here the moments take the form $H^n(LM)$, where n is the Hamiltonian projection, L is the spin, and M is the spin projection.